nature nanotechnology

Three-dimensional cellular recording

Check for updates

Three-dimensional transistor arrays for intra- and inter-cellular recording

Yue Gu[1,2], Chunfeng Wang[2], Namheon Kim[2], Jingxin Zhang[1], Tsui Min Wang[3], Jennifer Stowe[3], Rohollah Nasiri[4], Jinfeng Li[5], Daibo Zhang[3], Albert Yang[3], Leo Huan-Hsuan Hsu[6], Xiaochuan Dai[6], Jing Mu[2], Zheyuan Liu[7], Muyang Lin[2], Weixin Li[2], Chonghe Wang[2], Hua Gong[2], Yimu Chen[2], Yusheng Lei[2], Hongjie Hu[1,2], Yang Li[2], Lin Zhang[2], Zhenlong Huang[2], Xingcai Zhang[8], Samad Ahadian[4], Pooja Banik[2], Liangfang Zhang[2], Xiaocheng Jiang[6], Peter J. Burke[9], Ali Khademhosseini[4], Andrew D. McCulloch[3] and Sheng Xu[1,2,3,10,11] ✉

Electrical impulse generation and its conduction within cells or cellular networks are the cornerstone of electrophysiology. However, the advancement of the field is limited by sensing accuracy and the scalability of current recording technologies. Here we describe a scalable platform that enables accurate recording of transmembrane potentials in electrogenic cells. The platform employs a three-dimensional high-performance field-effect transistor array for minimally invasive cellular interfacing that produces faithful recordings, as validated by the gold standard patch clamp. Leveraging the high spatial and temporal resolutions of the field-effect transistors, we measured the intracellular signal conduction velocity of a cardiomyocyte to be 0.182 m s⁻¹, which is about five times the intercellular velocity. We also demonstrate intracellular recordings in cardiac muscle tissue constructs and reveal the signal conduction paths. This platform could provide new capabilities in probing the electrical behaviours of single cells and cellular networks, which carries broad implications for understanding cellular physiology, pathology and cell–cell interactions.

Electrophysiological approaches have been used to elucidate and modulate the activities of electrogenic cells[1,2]. Transmembrane potentials associated with ionic fluxes between the cytosol and interstitium underlie the macroscopic electrophysiological characteristics of tissues and organs[3]. Research in this field is largely driven by the use of well-established tools for high-fidelity transmembrane potential recording in single cells or multicellular networks. Ideally, the recording needs to be highly accurate and scalable over a large area. Sensor contact with the cytoplasm is needed for direct intracellular sensing[4,5]. Patch clamping, in its various forms[6], has been the gold standard for recording transmembrane potentials. However, it is challenging to perform on multiple cells simultaneously. Methods based on voltage-sensitive dyes can record multiple cells in parallel but are plagued by cytotoxicity and low temporal resolution[7]. Therefore, a variety of potentially scalable approaches have been explored for intracellular electrical recording, including passive electrodes and active field-effect transistors (FETs). Passive electrodes have difficulties in picking up subthreshold and low-amplitude cellular signals due to their intrinsically large impedance[8]. Active FETs, with minimal access impedance and wide bandwidths, have shown great promise for either intracellular sensing or scalability, but have not yet been demonstrated to meet the requirements for both[9].

Here we report a scalable three-dimensional (3D) FET array for sensing intracellular as well as intercellular signal conduction

in both two-dimensional (2D) cultures and 3D tissue constructs. This array has enabled us to directly measure intracellular signal conduction velocity, which is closely related to organ pathology, where its irregularities may be implicative of severe diseases[10]. We demonstrate that the intracellular signal conduction velocity in cardiomyocytes is about five times the intercellular conduction velocity reported conventionally. The difference between intracellular and intercellular velocities indicates the coupling efficacy between cells. We also demonstrate intracellular recordings of cardiomyocytes in cardiac muscle tissue constructs, revealing the signal conduction paths, which paves the way for intracellular electrophysiological studies in vivo.

Fabrication and characterization of the 3D FET arrays

The 3D FET array was constructed using a compressive buckling technique[11] (Fig. 1a). First, a multilayered 2D precursor was fabricated by standard micro/nanofabrication techniques (Fig. 1b, left). The precursor was transferred and selected regions were bonded onto a prestrained elastomer substrate, after which the prestrain of the elastomer substrate was released. The compression caused the 2D precursor to buckle at predesigned hinge locations to form a 3D structure (Fig. 1b, right, and Supplementary Video 1). To verify the electrical functions of the device before and after the buckling, dummy structures consisting of Au and Si–Au were processed in

[1]Materials Science and Engineering Program, University of California San Diego, La Jolla, CA, USA. [2]Department of NanoEngineering, University of California San Diego, La Jolla, CA, USA. [3]Departments of Bioengineering and Medicine, University of California San Diego, La Jolla, CA, USA. [4]Terasaki Institute for Biomedical Innovation, Los Angeles, CA, USA. [5]Department of Physics and Astronomy, University of California Irvine, Irvine, CA, USA. [6]Department of Biomedical Engineering, Tufts University, Medford, MA, USA. [7]Electrochemical Energy Laboratory, Massachusetts Institute of Technology, Cambridge, MA, USA. [8]School of Engineering and Applied Sciences, Harvard University, Cambridge, MA, USA. [9]Department of Chemical Engineering and Materials Science, University of California Irvine, Irvine, CA, USA. [10]Department of Radiology, University of California San Diego, La Jolla, CA, USA. [11]Department of Electrical and Computer Engineering, University of California San Diego, La Jolla, CA, USA. ✉e-mail: shengxu@ucsd.edu
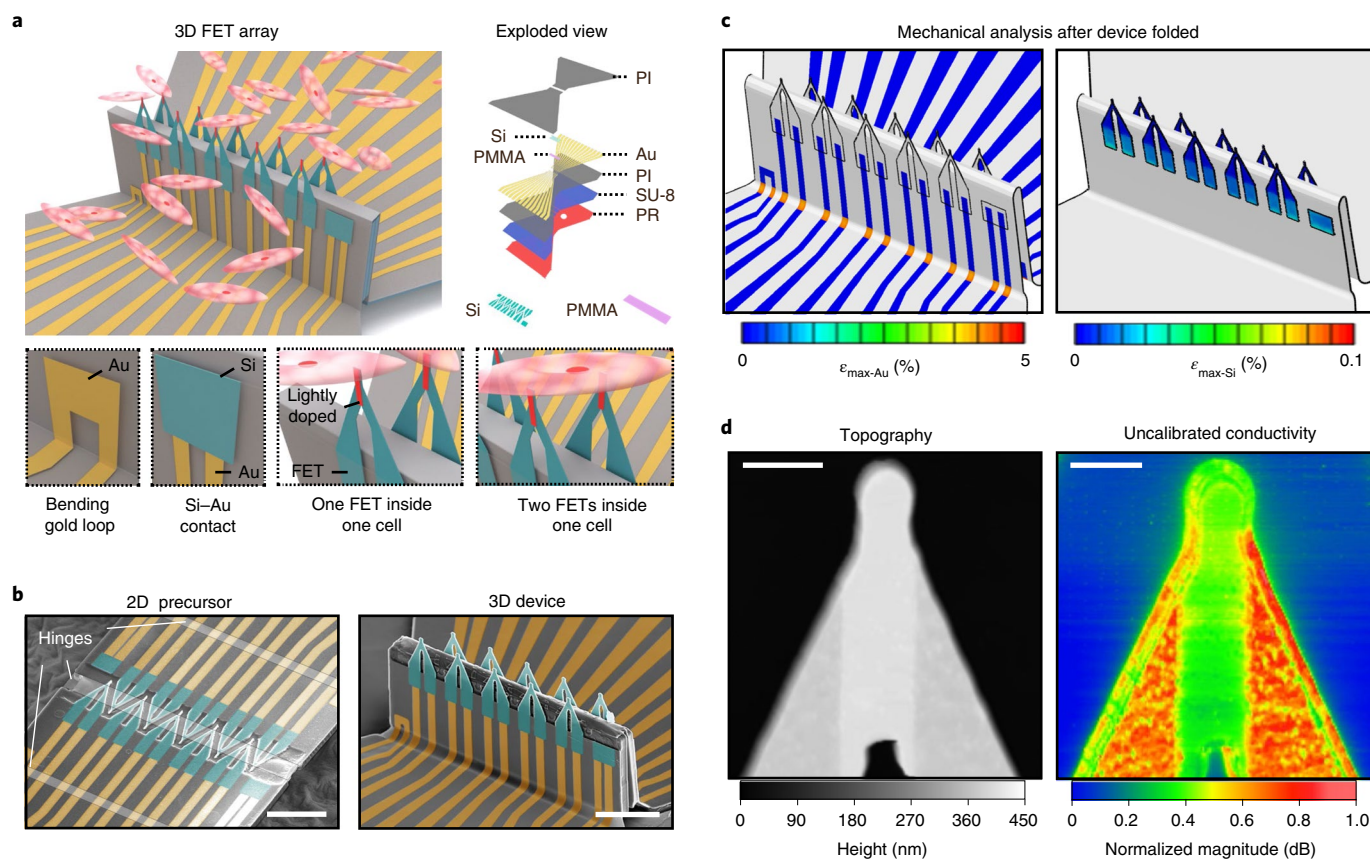
Fig. 1 | 3D FET arrays by compressive buckling. a, Schematic images showing a 10-FET array interfacing a group of cardiomyocytes. The exploded view illustrates the multilayered design of the FET array (top right). The images at the bottom show, from left to right, a Au loop for checking the electrical conductivity after the device buckles, a Au–Si bilayer for probing the quality of the electrical contact after the device has been soaked in an acidic solution, one FET recording intracellular signals and two FETs in the same cell to study intracellular signal conductions. The red area on each FET denotes the lightly doped channel. PI, polyimide; SU-8, an epoxy-based polymer; PR, photoresist. **b**, False-coloured SEM images showing the transformation from a 2D precursor (left) to a 3D 10-FET array (right). Each FET has a tapering tip (5 μm long and 1–2 μm wide). Scale bars, 50 μm. **c**, Finite element analysis of a 3D 10-FET array. The maximum strains (ε) in Au (left) and Si (right) are well below the fracture limit of each material. **d**, Images of a FET tip obtained by atomic force microscopy (left) and scanning microwave microscopy (right). The former operates in contact mode and maps the surface topography of the FET. The latter maps the uncalibrated conductivity, and thus the admittance distribution, of the FET. A lightly doped region can be clearly distinguished in both images. Because of the over-etching of the oxide doping mask, the lightly doped region is slightly thicker than the surrounding heavily doped regions (Supplementary Note 1). Also, the lightly doped region exhibits a lower conductivity than the surrounding heavily doped regions (Methods, Supplementary Note 2 and Extended Data Fig. 2). Scale bars, 2 μm.

parallel and used as checkpoints (Fig. 1a, bottom). The 3D structure was coated with a bilayer of Parylene C and SiO_2 for electrical insulation and hydrophilic surface functionalization. The compressive buckling technique enabled us to fabricate arrays at various scales with different materials, layouts, dimensions and geometries. For further details see Methods, Supplementary Note 1, Extended Data Fig. 1 and Supplementary Figs. 1–3.

The 3D geometry allows the FET to penetrate the cell membrane and record low-amplitude subthreshold signals inside the cell. The small sensor tip (1–2 μm) penetrates the cell membrane with minimal invasiveness[12]. The device layout was designed to allow interfacing with multiple cells and even to have two FETs in the same cell (Fig. 1a, bottom). To ensure that the entire device was mechanically robust, we carried out theoretical and experimental studies to optimize the materials and their dimensions, such as the use of low-molecular-weight poly(methyl methacrylate) (PMMA) and a thick acid-resistant photoresist as sacrificial layers. As simulated by finite element analysis (Fig. 1c), after the optimization, the maximum strains of the Au and Si in the buckled 3D device were 4 and 0.05%, respectively, which are below their failure strains[13,14]. The

buckling process was reversible. Under an externally applied tensile strain, the 3D device unfolded and recovered the 2D geometry. The softness of the device reduces the mechanical mismatch between the cell culture and the device[15]. The FET's structure was verified by atomic force microscopy and scanning microwave microscopy in topographic and reflection coefficient mapping modes, respectively (Fig. 1d and Extended Data Fig. 2).

The ability of a FET to accurately capture cellular signals, especially low-amplitude subthreshold potentials, depends on its sensitivity and noise level. The sensitivity is determined by the transconductance, which is tunable by the doping profile of the conduction channel (Supplementary Note 3). Lower doping concentrations typically yield higher sensitivities[16]. However, noise level also increases with sensitivity, especially in the low-frequency regime[17]. Therefore, we used the sensitivity-to-noise ratio to characterize the FET performance. By tailoring the doping time, we could precisely control the sheet resistance and thus doping concentrations in different regions of the FET, leading to a selectively doped n^+nn^+ (n-type semiconductor with more heavily doped drain and source regions than the gate region) structure. The n^+nn^+

structure is crucial for high sensitivity and operational reliability at zero gate bias because it operates in the 'ON' state with zero gate bias, which avoids the irreversible Faradaic reactions induced by the high gate voltage during signal recording observed with other FET structures (Extended Data Fig. 3 and Supplementary Note 4). For the FET geometry shown in Fig. 1d, we optimized the doping time to achieve the highest sensitivity-to-noise ratio (Fig. 2a). The sensitivity-to-noise ratios of the selectively doped FETs were much higher than those of FETs with low uniform doping (that is, only background doping from the substrate) or high uniform doping (Fig. 2b and Extended Data Fig. 3).

We characterized the transport behaviour of a 10-FET array in a water-gate configuration (Methods and Supplementary Fig. 4). The output characteristics of a FET in the array showed typical n-channel properties under various gate biases (Fig. 2c(i)). Furthermore, each FET exhibited large conductance under various drain potentials at zero gate bias (Fig. 2c(ii)), which is crucial for sensing cellular electrophysiological signals (Supplementary Note 4). The 10 FETs showed an average conductance of $0.9 \pm 0.3\,\mu S$ (Fig. 2d(i)) and an average transconductance of $7.5 \pm 2.0\,\mu S\,V^{-1}$ (Fig. 2d(ii)). The transconductance is greater than, and its relative standard deviation (that is, its coefficient of variation) is comparable to, those of devices synthesized by bottom-up methods[18], which can be attributed to the high material quality of the device-grade Si and controllable fabrication process. The high performance allows the FETs to record low-amplitude subthreshold cellular signals[3].

After transforming from two to three dimensions, the 10 FETs showed a <0.2% variation in conductance and a <0.5% variation in transconductance (Fig. 2e), which validates the mechanical and electrical robustness of the 3D FETs. The 10 FETs exhibited comparable conductance before and after immersion in saline solution (Fig. 2f), showing neglectable changes in surface charge and minimal current leakage through the insulation layers. Moreover, the FETs exhibited consistently high sensitivities over a range of pH (from 6.7 to 7.6) and temperatures (from 21 to 50 °C), demonstrating their tolerance to chemical and thermal conditions in various cell culture media (Extended Data Fig. 4). The stability of the FETs is primarily attributed to the insulating gate dielectric materials. The type of gate dielectric materials will not affect the FETs' sensitivity (Extended Data Fig. 4).

To ensure that we could record dynamic and transient ionic signals, we characterized the temporal response of the FETs. Pulse signals with a rise and fall time of 5 ns to 50 ms were applied to the gate, and the channel signals of the FETs were recorded. The FETs showed a short intrinsic response time to the input gate signals (≤712 ns), which is shorter than previously reported values due to its optimized small gate dielectric thickness[19] (Supplementary Note 5 and Supplementary Fig. 5). Due to the limit of the sampling rate of the digitizer (100 kHz maximum), the entire recording system has a temporal resolution of 0.01 ms. The recorded channel signal shows a response time of 0.1 ms (Fig. 2g(i)), which is sufficient to accurately record common ionic activities (typically >1 ms)[20]. Note that there is a capacitance-induced overshoot on the rising and falling edges of the response. The capacitance arises from electrode–ionic solution coupling, which can be neglected in cellular measurements because of the localized coupling between the membrane potential and the FET (for more details see Supplementary Note 3)[21]. In repeated measurements, the start and saturation times of the FET's response remained unchanged, showing that it can accurately follow the rapid input signals (Fig. 2g(ii)). With different rising/falling times (0.1–50 ms) of the input signal, the conductance changes were within ~1.5%, which is typical for FETs (Fig. 2g(iii))[21]. Additionally, the FETs can faithfully record simulated cellular action potentials resembling those produced by pacemaker and non-pacemaker cardiomyocytes, with frequencies of 1–10 Hz, covering the typical firing

frequencies of electrogenic cells. More discussions related to the response time of the FET are presented in Supplementary Notes 6–8 and Supplementary Fig. 6.

We coated a phospholipid bilayer onto the FETs to facilitate internalization into cells[4] and to enable good sealing at the FET–cell interface. Either small unilamellar vesicles of extracted red blood cell membranes or synthetic phospholipid bilayer materials (1,2-dimyristoyl-*sn*-glycero-3-phosphocholine) were used[4,22] (Methods). Fluorescent imaging confirmed the successful coating of the phospholipids on all FETs before and after buckling (Supplementary Note 9 and Supplementary Figs. 7 and 8). To illustrate the internalization process, when the FET is near the cell, it records the membrane potential extracellularly. The equivalent circuit model reveals an attenuated signal (V_c) due to the membrane impedance (which is composed of membrane resistance (R_m) and membrane capacitance (C_m) connected in parallel) and the shunt via the small spreading resistance (R_s). As the FET approaches the cell, the phospholipid coating spontaneously fuses with the cell membrane with minimal invasiveness to the cell, realizing intracellular sensing. The tight interfacial sealing maximizes the spreading resistance R_s (that is, minimizes leakage current) (Supplementary Fig. 8).

Recording intracellular action potentials

Full-amplitude signals contain quantitative information on ionic activities inside the cell[4,21]. The full amplitude depends on many factors, including the type, culture conditions and physiological status of the cell[4,21,23]. The FET arrays in this work can measure full-amplitude signals comparable to those acquired by the whole-cell patch clamp[21,24].

Cell viability test results proved that neither the construction materials nor the signal recording of the FET showed cytotoxicity towards HL-1 cardiac muscle cells (Supplementary Fig. 9). A Ca^{2+} sparks assay confirmed the electrophysiological activity of the HL-1 cells (Methods, Supplementary Figs. 10 and 11, and Supplementary Videos 2–4). Full-amplitude action potentials were stably recorded by both the FET and a whole-cell patch clamp (Fig. 3a and Supplementary Fig. 12). The amplitudes, morphologies and firing patterns of the acquired potentials by those two techniques show strong agreement, revealing the ideal coupling and faithful recording of the intracellular signals by the FETs. The minor discrepancies are within the standard fluctuations expected due to differences in cellular physiology and measurement set-ups[23,25] (Supplementary Note 10). Importantly, the FETs could record subthreshold signals due to their high sensitivity-to-noise ratios. Primary cells exhibit natural and primitive electrophysiological characteristics akin to their intrinsic states in live animals. The FET was able to record action potentials from spontaneously firing neonatal and adult mouse cardiomyocytes with results similar to those of the whole-cell patch[25–27] (Fig. 3b,c). The amplitude of each spike in the same recording fluctuates as a result of the contractile movements of the cells[24].

The phospholipid coating on the FETs plays a crucial role in the intracellular recording. Continuous intracellular signal recordings on HL-1 cells could be extended to over 70 s (Supplementary Fig. 13), the longest reported by an intracellular FET sensor. A phospholipid coating could last three cell insertions before refunctionalization was needed to achieve a stable intracellular recording (Supplementary Fig. 14). Without the phospholipid coating, the FET could still mechanically rupture the cellular membrane and access the cytoplasm sometimes. However, those recordings showed higher noise levels, lower signal amplitudes and fluctuating signal baselines due to the highly unstable FET–cell interface (Supplementary Fig. 15). Signals recorded without the phospholipid coating gradually transformed from intracellular to extracellular, probably because the ruptured cell membranes fused again and expelled the FET[24] (Supplementary Figs. 16–18).
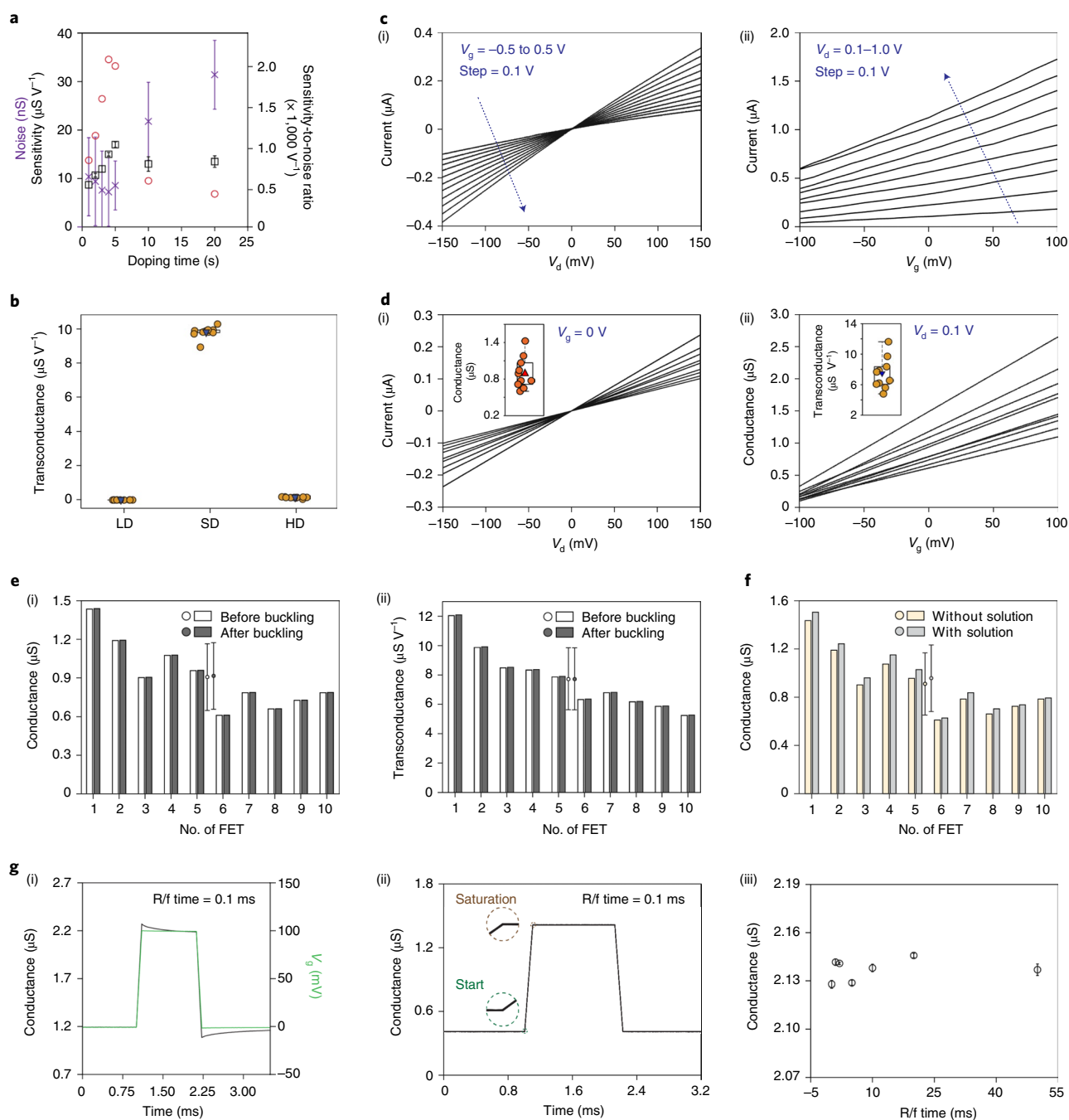
Fig. 2 | Electrical optimization and characterization of the FETs. a, The sensitivity-to-noise ratio of the FET as a function of doping time in the lightly doped region. A doping time of <4 s leads to a lower current in the conduction channel. A doping time of >4 s results in higher noise, because of a larger number of traps generated by doping-induced defects. Square, sensitivity; cross, noise; circle, sensitivity-to-noise ratio. **b**, Calculated transconductances of three devices with different doping profiles (Extended Data Fig. 3), showing that the FET structure is crucial for high sensitivity: low doping (LD, uniform doping at ~$10^7\,\Omega\,sq^{-1}$ in the silicon-on-insulator substrate), selective doping (SD, light doping at ~$10^4\,\Omega\,sq^{-1}$ in the gate and heavy doping in the drain and source) and heavy doping (HD, uniform doping at ~$10^2\,\Omega\,sq^{-1}$). **c**, Output characteristics of the n-channel FET in the linear region under different applied gate voltages (i) and transfer characteristics of the FET under different drain voltages (ii). The FET is in depletion mode, which is 'ON' at zero gate voltage. It shows a high transconductance in the –100 to 100 mV regime. V_d, drain voltage; V_g, gate voltage. **d**, Output (i) and transfer (ii) characteristics of each FET in a 10-FET array. The insets show the distribution of the FET conductance (i) and transconductance (ii). **e**, Comparison of the 10-FET array's conductance (i) and transconductance (ii) before and after compressive buckling, illustrating that the buckling process has no impact on the FET's electrical performance. The circles and error bars show the mean and standard deviation of the FETs' properties, respectively. **f**, Comparison of the FETs' electrical conductance with and without saline solution on the gate terminal, showing minimal current leakage of the FETs. The circles and error bars show the mean and standard deviations of the FETs' properties. The ionic solution induces slightly more carriers (due to surface-adsorbed H⁺), and thus slightly higher conductance in the conduction channel. **g**, Temporal response of the FETs to gate signals. A 100 mV pulse (rising/falling (R/f) time 0.1 ms, duration 1 ms, green curve) was applied to the gate, and the corresponding conductance of the FET (black curve) shows changes coincident with the input signal without any noticeable delay (i). Ten repeated characterizations of the same FET with an input gate signal at the sampling rate of 100 kHz (0.01 ms resolution) shows no observable jitter (<0.01 ms) in the data acquisition system (ii). The FET's conductance is reliable and independent of the rising/falling times of the input signals (iii).
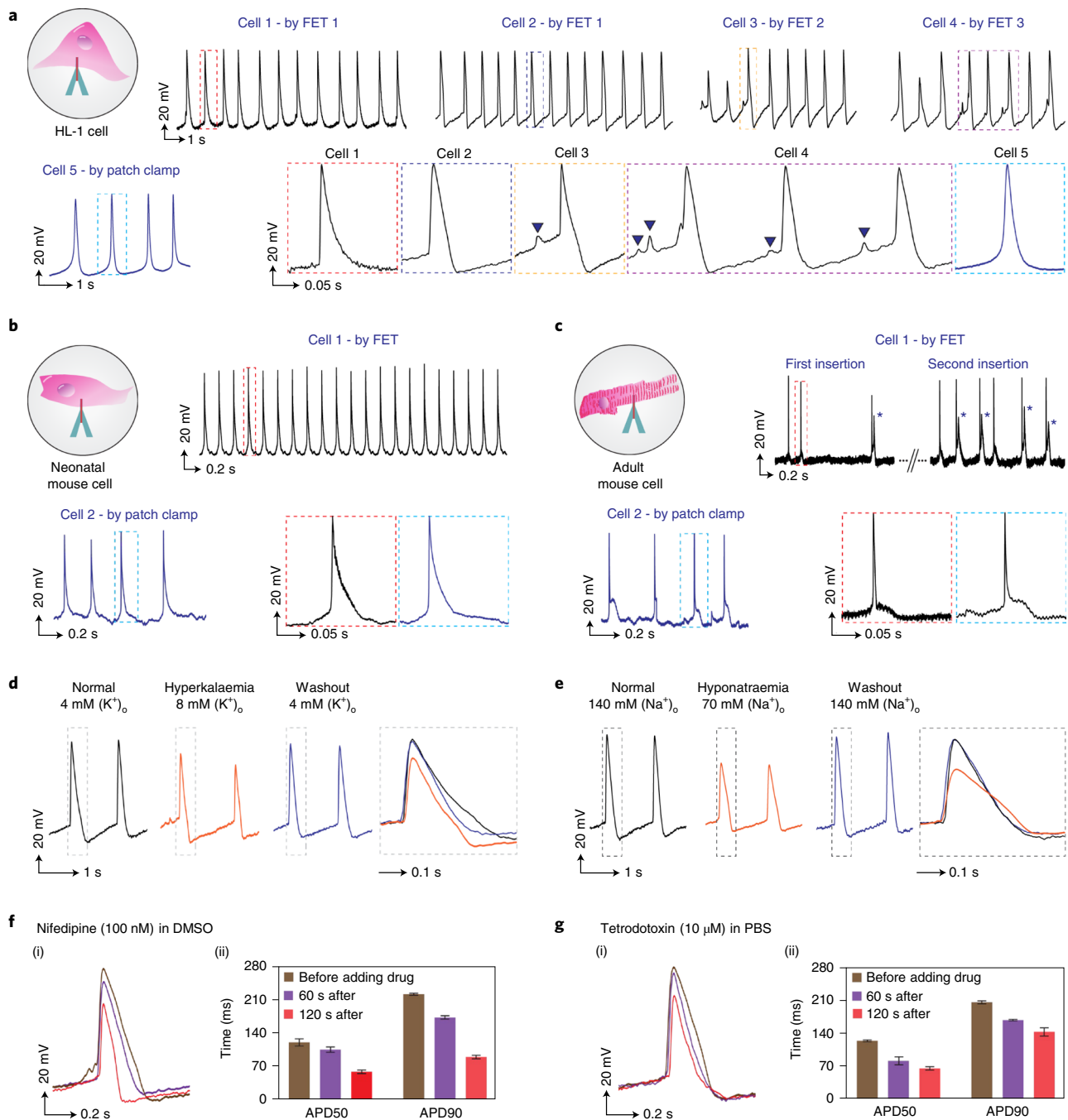
Fig. 3 | Intracellular recordings and validations on single cardiomyocytes. a, Periodic spikes can be recorded from different HL-1 cells by different FETs (top). The results are validated using the whole-cell patch clamp (lower left). The enlarged regions of the recordings by the FETs and the patch clamp (highlighted by boxes) represent typical pacemaker action potentials of the HL-1 cells (lower right). The mean of the action potentials measured by the FETs is 121.4 ± 1.3 mV, which is close to the 122.0 ± 4.0 mV measured by the patch clamp, showing the FETs' capability for recording full-amplitude action potentials. Subthreshold signals (for example, cell membrane oscillations of 5–15 mV) are captured in the recordings of cells 3 and 4, as highlighted by the black triangles. **b,c**, Intracellular recordings from primary cells including neonatal mouse atrial cardiomyocytes (**b**) and adult mouse ventricular cardiomyocytes (**c**). The greater noise in **c** is induced by the contraction of the adult mouse cells during measurements. In some spikes in **c**, an upstroke can be observed during repolarization, as marked by the asterisks, indicating abnormal Ca^{2+} influxes, which are also likely caused by the contraction. **d,e**, Pathological studies of the HL-1 cells by modulating potassium ion (**d**) and sodium ion (**e**) concentrations in the culture solutions (that is, solutions outside of the cell membrane, ion concentrations were labelled by $[K^+]_o$ and $[Na^+]_o$. Both the hyperkalaemia cells (**d**) and the hyponatraemia cells (**e**) exhibit a decreased signal amplitude, a shortened action potential duration and a longer refractory period compared with the normal cells, as recorded by the FET. The recorded action potentials recover when the culture solutions are switched back to Tyrode's solution. **f,g**, Effects of the ion channel blocking drugs nifedipine (**f**) and tetrodotoxin (**g**) on the action potential morphologies of HL-1 cells recorded by the FET (i) and the corresponding quantitative analysis (ii). Cells exposed to 100 nM nifedipine exhibit a lower spike amplitude and shorter APD50 and APD90. The cells repolarize very quickly because nifedipine is an L-type Ca^{2+} channel blocker, which diminishes the influx of Ca^{2+} into the cells. Tetrodotoxin (10 μM) acts on the rapid Na^+ channels, reducing the spike amplitude and thus shortening the repolarization duration. The colour code in **f,g**(ii) applies to **f,g**(i). The error bars represent standard deviations of 20 recorded action potentials. DMSO, dimethylsulfoxide; PBS, phosphate-buffered saline.

We tested the FET performance by verifying the HL-1 cells' response to extracellular solution composition and ion channel blocking drugs. Figure 3d,e shows the effect of hyperkalaemia or hyponatraemia on the recorded electrophysiological behaviours of cardiomyocytes, including the beating rhythm, resting membrane potential and action potential duration. Abnormally high potassium or low sodium ion concentration would vary the cell's action potential shape by shortening the duration and decreasing the amplitude[28,29]. Figure 3f,g shows the measured responses of HL-1 cells to ion channel blockers with modulated action potential amplitude and duration. The results show that nifedipine or tetrodotoxin lowers the amplitude and reduces the action potential duration (APD) at 50 or 90% repolarization (APD50 or APD90; the data are listed in Supplementary Table 1). The effect was reversible, as revealed after the extracellular solution was swapped back to the normal composition.

Recording intercellular signal conductions

We used a 3D 10-FET array with well-defined spacing (Fig. 4a) to record intercellular signal conductions, which are related to the electrical coupling states between cells[30]. When a common electrical pulse was provided, the FETs exhibited the same characteristics and the electrical signal delay between any two channels was no greater than 0.01 ms, suggesting that the system-induced electrical delay was negligible (Supplementary Fig. 19). A layer of spontaneously firing HL-1 cells cultured on a polydimethylsiloxane (PDMS) sheet was laminated on the FET array (Fig. 4b; see Methods and Supplementary Figs. 4 and 20–23 for details). We used electrical stimulation to regulate the firing patterns of the HL-1 cells to study the direction and velocity of intercellular signal conduction. Four electrodes were placed in the four corners of the cell culture, and a stimulation pulse was applied to one electrode in each measurement (Fig. 4c). Under electrical pacing, spontaneous arrhythmic action potentials were suppressed[31], and the corresponding recorded cellular signals are shown in Fig. 4d, Supplementary Fig. 24 and Extended Data Fig. 5. We calculated the signal latencies between the FETs by cross-correlating the recorded action potential profiles (Supplementary Fig. 25 and Supplementary Table 2). The heat map in Fig. 4d visualizes the action potential conduction direction among the cells, as indicated by the arrows. Based on the conduction latencies and the predefined distances between the FETs, the intercellular signal conduction velocity was calculated to be 35.1–39.3 μm ms⁻¹, comparable to the results from other studies on HL-1 cells[32]. Long-period recordings showed the robustness of the measurements by the FET array (Supplementary Fig. 26 and Supplementary Table 3).

Fast signal conductions within a cell

Intracellular signal conduction in cardiomyocytes corresponds to various forms of subcellular ionic activities[33]. However, it is challenging to record intracellular conductions in cardiomyocytes because it is difficult to interface two or more patch clamps with one cardiomyocyte[34]. Also, the short signal latency inside the cardiomyocyte can be overshadowed by the intrinsic delay of the existing recording systems[35].

In Fig. 4d, regardless of the orientation of the stimulation electrode, we found the latencies between the FETs at (2,3) and (1,3) to be always in the range 0.10–0.20 ms (Supplementary Table 2), which is much shorter than those between the other FETs. Given the distance between these two FETs (26.6 μm), the conduction velocity was calculated to be 182 μm ms⁻¹, which is about five times the intercellular conduction velocity (Fig. 4e). To verify the measurement, we used the same 10-FET array to study a different HL-1 cell culture. This time, we found no signal conduction between the FETs at (2,3) and (1,3), but two other FETs, at (1,1) and (1,2), showed a latency of ~0.18 ms (Supplementary Figs. 27c,d). To triple check

the measurements, we used confocal microscopy to image live cells while simultaneously recording electrical signals. The results verified that two FETs were in the same cell (Fig. 4f and Supplementary Fig. 28). Therefore, the signals we measured between these two FETs are intracellular conductions. The slight fluctuation in the intracellular conduction velocity may be because of the constantly changing ionic distributions within the cell. The intracellular conduction is much faster than the intercellular conduction because the latter is slowed by ion diffusion processes via gap junctions between neighbouring cells[36].

Additionally, in Fig. 4d, when the stimulation originated from different orientations relative to the FETs, the corresponding intercellular signal conduction direction would change. However, we found that the intracellular conduction direction was always from (1,3) to (2,3), independent of the direction of intercellular conduction, which is probably related to the positions of the FETs and the coupling of cells with neighbouring cells (Supplementary Figs. 27e,f and 29). In other measurements, the intracellular conduction direction was reversed with different stimulation orientations (Supplementary Fig. 27e,f).

Intracellular recording of 3D tissue constructs

Compared with 2D cellular cultures, 3D engineered tissue constructs better resemble natural organs in structural complexity and physiological functions. Therefore, they are excellent models for intracellular electrophysiology studies[37]. However, existing devices have limitations in interfacing with 3D tissues: either they can only perform extracellular sensing[38], or they have a uniform height suitable for interrogating cells on a common plane only[24,25].

With tunable heights, the 3D FET array provides a unique opportunity to study the electrophysiology of 3D tissues. To this end, we fabricated a stretchable 128-FET array distributed in 40 units of three different heights, capable of interrogating cells at three different depths in a 3D microtissue (Fig. 5a and Supplementary Figs. 30–34). Representative recordings by the array showed intracellular action potentials in a 3D cardiac tissue, with 44% of the FETs being intracellular, 34% extracellular and 22% inactive, the intra- or extracellular signals being defined by the shape and amplitude of the signals[39] (Fig. 5b,c). The inactive FETs could be due to electrically inactive cells, degraded performance of the FET or non-ideal FET–cell coupling (for example, because of an elastic response from the cytoskeleton).

We used the FETs in each unit to study the small-scale intercellular signal conductions, whose velocities were calculated to be 18.8 ± 7.5 μm ms⁻¹, consistent with reported values[25] (Fig. 5d and Extended Data Fig. 6). We also leveraged the relatively large spacing between the 40 units of the FETs to determine the velocity of large-scale signal conduction (Fig. 5e). For each of the three heights, the signals propagate clockwise among the units, forming a loop (Fig. 5e). The signal conduction velocities in the three different loops were calculated to be 10.9, 11.8 and 12.2 μm ms⁻¹ (Fig. 5f). The calculated large-scale conduction velocities are generally lower than the small-scale velocities within each unit, because we assume the signal conduction path is linear from point to point on the large scale, whereas the actual path is likely to follow a zig-zag pattern[25], depending on the relative positions of the cells and their electrical coupling states.

Conclusions

With the device size down to the submicrometre regime, the high sensitivity and the high signal-to-noise ratio, FETs have attracted growing attention in the last decade as a tool for interrogating electrogenic cells. Two-dimensional planar FETs for extracellular interfacing usually lack one-to-one correspondence between the cells and FETs, providing information on an ensemble of cells near the FET. Three-dimensional FETs allow direct interfacing
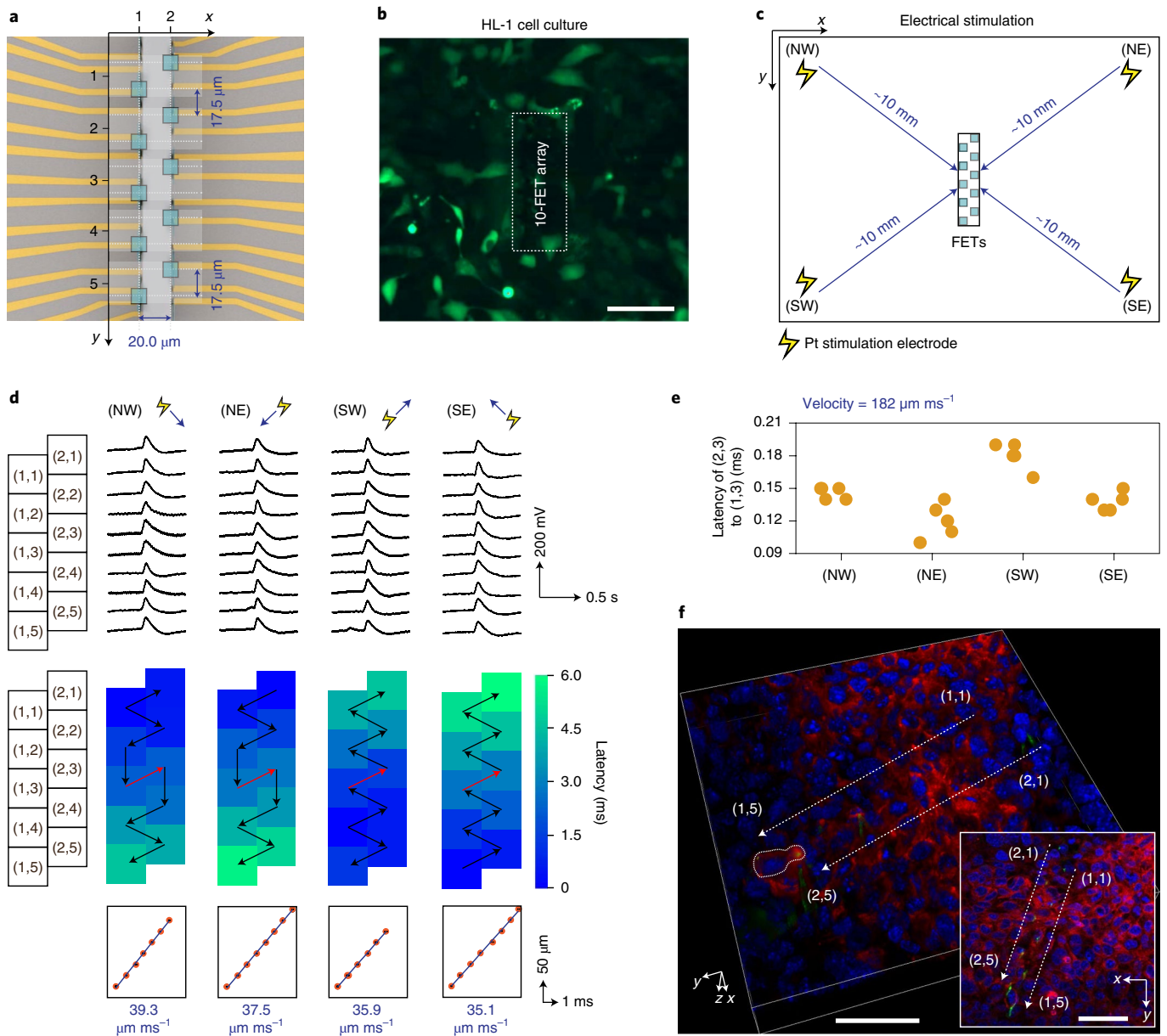
Fig. 4 | Intracellular recording of a 2D HL-1 cell culture by a 10-FET array. a, Schematic top view of a 10-FET array. The spacing between each FET was accurately defined by lithography. A coordinate system is used to denote the position of each FET, indicated by the green squares. **b**, A fluorescent image of a 10-FET array interfacing with a 2D culture of HL-1 cells (average size ~50 μm), stained by Fluo-4 AM dye. During the measurement, only the FETs are interfacing the cells, while the areas around them are not contacting them. Scale bar, 100 μm. **c**, Schematic of the set-up for stimulating the HL-1 cells, with four Pt electrodes placed in four corners of the cell culture. A stimulation pulse was applied to a single electrode in each measurement. We used biphasic pulses, so the net injection current was zero. The frequency, width and amplitude of the pulses were 1 Hz, 1 ms and 1 V, respectively, to effectively pace the cells. **d**, Simultaneous intracellular recordings from a 2D HL-1 cell culture under electrical pacing at different orientations to the FETs (top). All FETs recorded periodic intracellular action potentials of 95–116 mV (Extended Data Fig. 5). Heat maps illustrate the latency of the action potentials among the cells (middle). The arrows indicate the possible signal conduction paths between the cells; the black arrows show intercellular signal conductions and the red arrows show intracellular signal conductions. In all measurements, the signal first arrives at the cell closest to the stimulation electrode and then transmits to the neighbouring cells. The average intercellular conduction velocity is 35.1–39.3 μm ms^{-1} (bottom). Regardless of the stimulation orientation to the FETs, the intracellular signal conduction is always from (1,3) to (2,3). **e**, The average latency between (1,3) and (2,3) calculated from the 20 action potentials in four orientations is 0.146 ± 0.025 ms. The intracellular conduction velocity is 182 μm ms^{-1}, which is about five times the velocity of intercellular conduction. **f**, Confocal microscopy image illustrating a 3D view of FETs intracellularly interfacing live HL-1 cells. The inset shows the corresponding top view. Green (rhodamine 6G), the PI in the FETs; red (CellBrite), cell membranes; blue (NucBlue), cell nuclei. The images clearly show that two FETs, (1,5) and (2,5), are interfacing the same cell. The corresponding action potential recordings are presented in Supplementary Fig. 28d. Scale bars, 50 μm.

with the cytoplasm of cells, which ensures correspondence with each specific recorded cell. However, existing 3D FET devices are not suited to large-scale, high-spatial-resolution sensing[8]. With an

unprecedented number of FETs and a predefined layout, the 3D FET array demonstrated in this work can fill this technological gap (Supplementary Fig. 35).
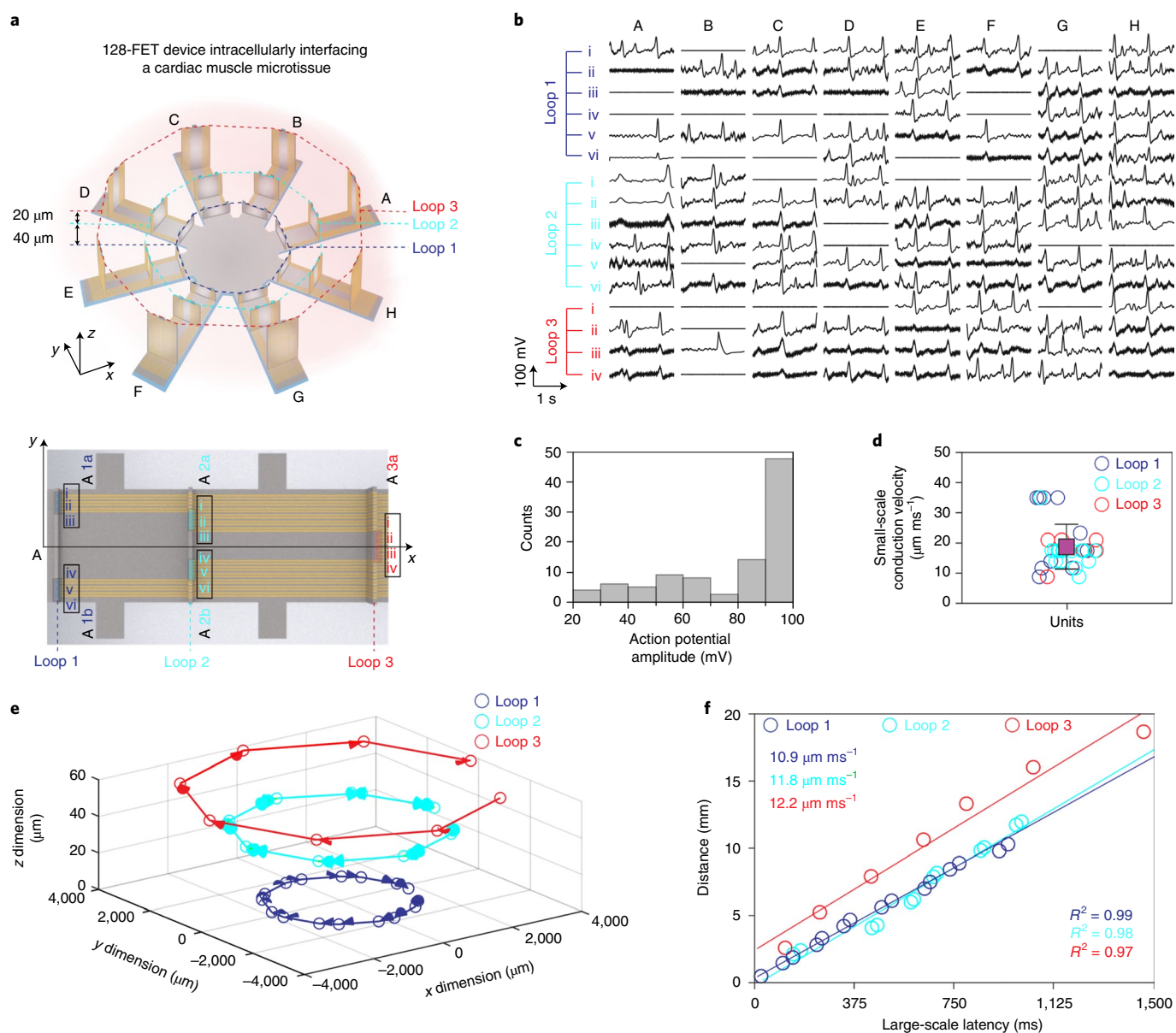
Fig. 5 | Intracellular recording of a microtissue of neonatal rat cardiomyocytes using a 128-FET array. a, Schematic diagrams of the 128-FET array distributed on eight arms. On each arm, there are 16 FETs in five units of different heights, distributed in three concentric loops (top). The relative positions of the 16 FETs and their coordinates are indicated (bottom). **b,** Representative recordings from the 3D cardiac tissue by the 128-FET array. Intracellular action potentials are recorded from all three loops on each arm. **c,** A histogram of the spike amplitudes in **b**. **d,** The small-scale intercellular signal conduction velocity measured within each unit. The average velocity (purple square) within the 40 units is $18.8 \pm 7.5 \, \mu m \, ms^{-1}$. **e,** Three-dimensional visualization of the signal conduction in the whole 3D tissue construct. The signal conduction directions are consistent in all three loops, beginning at arm H and then propagating to arm A. **f,** Linear fit of the intercellular signal conduction velocity across the units in each loop.

The arrayed FETs provide tremendous opportunities for studying the fundamental physiologies of electrogenic cells. The acquired knowledge can help to understand the pathology and guide the treatment of numerous evolutionary disease models[40]. Intracellular signals disclose more meaningful information about the cell type and density of various ion channels[1,2]. In particular, full-amplitude action potentials are highly relevant to the disease status and pathology of cells[41]. Subthreshold signals can potentially shed light on the process of intercellular synchronization[42], the mechanism of electrophysiological modulation[20,43] and how these subthreshold signals impact the development of sensory systems[44]. Studies of the conduction behaviour would not only enhance the understanding of the ionic transport across organellular membranes within a cell[45],

but also facilitate the study of electrical coupling between different cells[36]. These findings have important implications for understanding subcellular electrophysiology, organellar ionic dynamics[45], organelle–cell membrane interaction[46] and their influences on cellular physiological activities, including proliferation, differentiation and apoptosis[47].

Further explorations could follow by applying the 3D FET array to various types of cardiac tissues, such as embryonic stem cell-derived cardiomyocytes, myocyte–fibroblast cocultures and other general electrogenic cells, such as neurons. Reliable recordings of 3D tissues on a large scale may reveal cellular alignment directions. Future translation of this platform technology to in vivo studies will depend on the FET's ability to penetrate through the

thick membranes of the myocardium and the cortex, prevent severe immune responses and eliminate motion artifacts induced by heart beating and brain pulsation. To that end, further refinement of the 3D FET structure (for example, tip size, spacing and relative positions), array size, structural materials, surface coating and deployment approach, as well as the use of artificial intelligence-assisted signal processing, would be essential to enhance the reliability, quality and duration of the recordings.

Online content

Any methods, additional references, Nature Research reporting summaries, source data, extended data, supplementary information, acknowledgements, peer review information; details of author contributions and competing interests; and statements of data and code availability are available at https://doi.org/10.1038/s41565-021-01040-w.

References

1. Kim, D. H. et al. Dissolvable films of silk fibroin for ultrathin conformal bio-integrated electronics. *Nat. Mater.* **9**, 511–517 (2010).
2. Abbott, J. et al. A nanoelectrode array for obtaining intracellular recordings from thousands of connected neurons. *Nat. Biomed. Eng.* **4**, 232–241 (2020).
3. Dai, X. et al. Three-dimensional mapping and regulation of action potential propagation in nanoelectronics-innervated tissues. *Nat. Nanotechnol.* **11**, 776–782 (2016).
4. Tian, B. et al. Three-dimensional, flexible nanoscale field-effect transistors as localized bioprobes. *Science* **329**, 830–834 (2010).
5. Jiang, Y. et al. Heterogeneous silicon mesostructures for lipid-supported bioelectric interfaces. *Nat. Mater.* **15**, 1023–1030 (2016).
6. Wang, X. & Li, M. Automated electrophysiology: high throughput of art. *Assay Drug Dev. Technol.* **1**, 695–708 (2003).
7. Fast, V. G. & Kléber, A. G. Microscopic conduction in cultured strands of neonatal rat heart cells measured with voltage-sensitive dyes. *Circ. Res.* **73**, 914–925 (1993).
8. Hong, G. & Lieber, C. M. Novel electrode technologies for neural recordings. *Nat. Rev. Neurosci.* **20**, 330–345 (2019).
9. Zhang, X. Nanowires pin neurons: a nano "moon landing". *Matter* **1**, 560–562 (2019).
10. Aranega, A., de la Rosa, A. & Franco, D. Cardiac conduction system anomalies and sudden cardiac death: insights from murine models. *Front. Physiol.* **3**, 211 (2012).
11. Xu, S. et al. Assembly of micro/nanomaterials into complex, three-dimensional architectures by compressive buckling. *Science* **347**, 154–159 (2015).
12. Tian, B. & Lieber, C. M. Nanowired bioelectric interfaces. *Chem. Rev.* **119**, 9136–9152 (2019).
13. Fan, J. A. et al. Fractal design concepts for stretchable electronics. *Nat. Commun.* **5**, 3266 (2014).
14. Khang, D. Y., Jiang, H., Huang, Y. & Rogers, J. A. A stretchable form of single-crystal silicon for high-performance electronics on rubber substrates. *Science* **311**, 208–212 (2006).
15. Schaefer, N. et al. Multiplexed neural sensor array of graphene solution-gated field-effect transistors. *2D Mater.* **7**, 025046 (2020).
16. Lee, J. W. et al. Analysis of charge sensitivity and low frequency noise limitation in silicon nanowire sensors. *J. Appl. Phys.* **107**, 044501 (2010).
17. Rettinger, J., Schwarz, S. & Schwarz, W. Electrophysiology (Springer, 2016).
18. Noy, A. Bionanoelectronics. *Adv. Mater.* **23**, 807–820 (2011).
19. Hempel, F. et al. PEDOT:PSS organic electrochemical transistor arrays for extracellular electrophysiological sensing of cardiac cells. *Biosens. Bioelectron.* **93**, 132–138 (2017).
20. Grant, A. O. Cardiac ion channels. *Circ. Arrhythm. Electrophysiol.* **2**, 185–194 (2009).
21. Duan, X. et al. Intracellular recordings of action potentials by an extracellular nanoscale field-effect transistor. *Nat. Nanotechnol.* **7**, 174–179 (2011).
22. Gong, H. et al. Biomembrane-modified field effect transistors for sensitive and quantitative detection of biological toxins and pathogens. *ACS Nano* **13**, 3714–3722 (2019).
23. Qing, Q. et al. Free-standing kinked nanowire transistor probes for targeted intracellular recording in three dimensions. *Nat. Nanotechnol.* **9**, 142–147 (2014).
24. Zhao, Y. et al. Scalable ultrasmall three-dimensional nanowire transistor probes for intracellular recording. *Nat. Nanotechnol.* **14**, 783–790 (2019).
25. Abbott, J. et al. CMOS nanoelectrode array for all-electrical intracellular electrophysiological imaging. *Nat. Nanotechnol.* **12**, 460–466 (2017).
26. Xie, C. et al. Intracellular recording of action potentials by nanopillar electroporation. *Nat. Nanotechnol.* **7**, 185–190 (2012).
27. Elcarpio, J. O. B. D. et al. HL-1 cells: a cardiac muscle cell line that contracts and retains phenotypic characteristics of the adult cardiomyocyte. *Proc. Natl Acad. Sci. USA* **95**, 2979–2984 (1998).
28. Hegyi, B., Chen-Izu, Y., Izu, L. T. & Bányász, T. Altered K$^+$ current profiles underlie cardiac action potential shortening in hyperkalemia and β-adrenergic stimulation. *Can. J. Physiol. Pharmacol.* **97**, 773–780 (2019).
29. Lu, Y.-Y. et al. Electrolyte disturbances differentially regulate sinoatrial node and pulmonary vein electrical activity: a contribution to hypokalemia- or hyponatremia-induced atrial fibrillation. *Heart Rhythm* **13**, 781–788 (2016).
30. Robinson, J. T. et al. Vertical nanowire electrode arrays as a scalable platform for intracellular interfacing to neuronal circuits. *Nat. Nanotechnol.* **7**, 180–184 (2012).
31. Czeschik, A. et al. Nanostructured cavity devices for extracellular stimulation of HL-1 cells. *Nanoscale* **7**, 9275–9281 (2015).
32. Kireev, D. et al. Graphene multielectrode arrays as a versatile tool for extracellular measurements. *Adv. Healthc. Mater.* **6**, 1601433 (2017).
33. Bers, D. M., Barry, W. H. & Despa, S. Intracellular Na$^+$ regulation in cardiac myocytes. *Cardiovasc. Res.* **57**, 897–912 (2003).
34. Brown, A. M., Lee, K. S. & Powell, T. Voltage clamp and internal perfusion of single rat heart muscle cells. *J. Physiol.* **318**, 455–477 (1981).
35. Gouwens, N. W. & Wilson, R. I. Signal propagation in *Drosophila* central neurons. *J. Neurosci.* **29**, 6239–6249 (2009).
36. McCain, M. L. et al. Cell-to-cell coupling in engineered pairs of rat ventricular cardiomyocytes: relation between Cx43 immunofluorescence and intercellular electrical conductance. *Am. J. Physiol. Heart Circ. Physiol.* **302**, H443–H450 (2012).
37. Lancaster, M. A. & Knoblich, J. A. Organogenesis in a dish: modeling development and disease using organoid technologies. *Science* **345**, 1247125 (2014).
38. Hong, G. et al. A method for single-neuron chronic recording from the retina in awake mice. *Science* **360**, 1447–1451 (2018).
39. Dipalo, M. et al. Intracellular and extracellular recording of spontaneous action potentials in mammalian neurons and cardiac cells with 3D plasmonic nanoelectrodes. *Nano Lett.* **17**, 3932–3939 (2017).
40. Nattel, S. Electrical coupling between cardiomyocytes and fibroblasts: experimental testing of a challenging and important concept. *Cardiovasc. Res.* **114**, 349–352 (2018).
41. Lin, Z. C. et al. Accurate nanoelectrode recording of human pluripotent stem cell-derived cardiomyocytes for assaying drugs and modeling disease. *Microsyst. Nanoeng.* **3**, 16080 (2017).
42. Desmaisons, D., Vincent, J.-D. & Lledo, P.-M. Control of action potential timing by intrinsic subthreshold oscillations in olfactory bulb output neurons. *J. Neurosci.* **19**, 10727–10737 (1999).
43. Frohnwieser, B., Chen, L. Q., Schreibmayer, W. & Kallen, R. G. Modulation of the human cardiac sodium channel alpha-subunit by cAMP-dependent protein kinase and the responsible sequence domain. *J. Physiol.* **498**, 309–318 (1997).
44. Boehmer, G., Greffrath, W., Martin, E. & Hermann, S. Subthreshold oscillation of the membrane potential in magnocellular neurones of the rat supraoptic nucleus. *J. Physiol.* **526**, 115–128 (2000).
45. Kamiya, K. et al. Electrophysiological measurement of ion channels on plasma/organelle membranes using an on-chip lipid bilayer system. *Sci. Rep.* **8**, 17498 (2018).
46. Li, J. et al. Scanning microwave microscopy of vital mitochondria in respiration buffer. In *Proc. 2018 IEEE MTT-S International Microwave Symposium* 115–118 (IEEE, 2018).
47. Moon, C. H. et al. KR-31378, a novel benzopyran analog, attenuates hypoxia-induced cell death via mitochondrial K$_{ATP}$ channel and protein kinase C-ε in heart-derived H9c2 cells. *Eur. J. Pharmacol.* **506**, 27–35 (2004).

Methods

The materials, software/algorithms and equipment are listed in the Supplementary Information.

Fabrication of the 3D FETs. The FET arrays were fabricated by the compressive buckling technique. The 2D structure contained silicon FETs, gold electrodes prepared by sputtering, two PI layers and an SU-8 mechanical supporting layer obtained by spin casting. The shapes and patterns of each layer were defined by lithography and reactive ion etching. The overall fabrication process included four main steps. In a nutshell, the FET was first prepared on a silicon-on-insulator wafer by standard cleanroom micro/nanofabrication techniques. Second, the completed FET was released from the silicon-on-insulator wafer and transfer-printed onto a temporary 2D substrate. Third, different functional materials were sequentially deposited onto the FET to enable the electrical and mechanical robustness of the device. Finally, the fabricated multilayered device was released and transfer-printed onto a prestrained elastomeric substrate for controlled buckling. The fabrication process is described in detail in Fig. 1, Extended Data Fig. 1 and Supplementary Note 1.

Finite element analysis of the 3D FET. ABAQUS (v.6.13, Dassault Systèmes Simulia Corp.) was used to study the mechanical behaviour of the device during compressive buckling. As the thickness of the silicone substrate was much greater than that of the device, a boundary condition was to constrain the device to buckle only above the substrate. Displacement boundary conditions were applied to the two edges of the device to initiate the compression. Composite shell elements (S4R) were used to model the SU-8, PI, Si and Au layers. The minimal size of the element was set to be half of the FET tip's width ($\sim$0.5 μm). The total number of elements in the model was $\sim$106. Mesh convergence of the simulation was accomplished in all cases. The elastic moduli (E) and Poisson's ratios (ν) of the different layers are as follows: $E_{PI} = 2.5$ GPa, $\nu_{PI} = 0.34$; $E_{Si} = 130$ GPa, $\nu_{Si} = 0.27$; $E_{Au} = 78$ GPa, $\nu_{Au} = 0.44$; $E_{SU-8} = 4$ GPa, $\nu_{SU-8} = 0.22$. The fracture strains of Au and Si are 5 and 1%, respectively[14,15].

Surface conductivity mapping of the FET. The FET was characterized using a scanning microwave microscope (Keysight™ 7500), which combined an atomic force microscope and a vector network analyser. The atomic force microscope had a conductive probe that scanned the FET surface, revealing the topography. Simultaneously, a microwave signal from the network analyser was transmitted to the probe, reflected by the sample at the contact point and then sent back to the network analyser. The conductance information was obtained from the reflection coefficient, determined from the transmission and reflection signals. The reflection coefficient calculations are presented in Supplementary Note 2.

Phospholipid coating. Phospholipid coating of the FET surface facilitated the cell internalization process, through spontaneous fusion, to achieve direct contact with the cell cytosol. Briefly, large phospholipid vesicles in aqueous solutions were broken into small unilamellar vesicles by consecutive freeze-and-thaw treatments, sonication and filter extrusion. These high-surface-energy vesicles formed a uniform phospholipid coating on the FET surface by self-assembly. The schematics in Supplementary Fig. 7 and Supplementary Note 9 demonstrate the whole process. Successful coating of the phospholipids was verified by fluorescent imaging (Supplementary Fig. 8).

Fabrication of the multi-electrode array. The multi-electrode array (MEA), composed of Au electrodes, an SU-8 insulation layer and a glass substrate, was fabricated using standard micro/nanofabrication techniques. The fabrication process is described in detail in Supplementary Note 11.

Water-gate characterization. FET sensitivity was determined by measuring the FET transfer characteristics. In the water-gate characterization (Supplementary Fig. 4), the corresponding FET conductance was measured under a fixed positive bias (for example, 200 mV) at the source and a potential sweep (from −100 to 100 mV) at the gate. Experimental details are provided in Supplementary Note 6.

Ca^{2+} sparks screening. The schematics in Supplementary Fig. 10 illustrate the process of staining Ca^{2+} and monitoring their transient activity under a fluorescent microscope. First, the HL-1 cells were cultured in supplemented Claycomb medium. We then removed the cell culture medium by aspiration and added typical clear-colour Tyrode's solution. Second, we added Fluo-4 AM (Invitrogen™) stock solution to the cells and incubated them for 1 h to facilitate the loading of calcein dyes. Then, we removed the old solution and refilled it with fresh Tyrode's solution. Finally, we monitored the Ca^{2+} signals under a microscope with a 480 nm excitation filter and a 525 nm emission filter.

HL-1 cell culture. We followed the standard cell culture protocol provided by Sigma-Aldrich. All materials and solutions were from Sigma-Aldrich. The cells were cultivated in supplemented Claycomb medium after precoating the substrates with templating materials. We prepared the cell cultures on PDMS sheets for signal recording, in cell culture flasks for cell proliferation and on cell culture dishes for Ca^{2+} sparks screening. The details are provided in Supplementary Note 7.

Primary cardiomyocytes culture. Neonatal mouse ventricular myocytes were isolated from 1- to 2-day-old Black Swiss mouse pups purchased from Charles Rivers Laboratories. Adult mouse single ventricular myocytes were isolated from mouse ventricles using Langendorff's enzymatic digestion method. The cells were obtained by digesting the ventricles in buffered solutions. After removing the fibroblast cells and blood from the vasculature, the cardiomyocytes were cultured on laminin-templated PDMS sheets or cell culture dishes for signal recording. The preparation of the solutions is described in detail in Supplementary Note 8.

Whole-cell patch clamp electrophysiology. Whole-cell current patching of HL-1 cells and primary cardiomyocytes was performed at 35 °C with cells plated on a PDMS sheet superfused with an external solution. A glass micropipette that was filled with the solution in its lumen was attached to the cell membrane, forming a gigaseal between the micropipette and the cell membrane. After that, the membrane patch was ruptured by a negative pressure in the pipette, which established the whole-cell configuration. Action potentials were recorded with a holding potential of −80 to −40 mV, and evoked by injecting currents into the cells. More information is provided in Supplementary Note 12.

Data acquisition. An electrophysiological signal acquisition system includes the FETs for interfacing the cells, preamplifiers, a signal digitizer and a graphical user interface (that is, computer software) for data visualization. We used a customized 10-channel preamplifier and a commercial data acquisition system and software (Axon) with the 10-FET array, and a commercial 256-channel current-input analogue-to-digital converter (Texas Instruments) and its configured software with the 128-FET array. The sampling rates adopted in these recordings ranged from 500 to 100,000 Hz in the different systems. Before recording cellular signals, we characterized the complete signal measurement system (including a 10-FET array, the preamplifier and the data acquisition device) and confirmed that the system had low intrinsic noise and no electrical crosstalk between the channels (Supplementary Figs. 22 and 23). More information is provided in Supplementary Note 13.

Signal processing. All signal recordings were post-processed offline in MATLAB (MathWorks). The intracellular and extracellular signals of 2D cell cultures (HL-1 cells, adult and neonatal mouse cardiomyocytes) recorded by the FETs had high signal-to-noise ratios and thus the raw data are presented. The MEA recordings of HL-1 cells were passed through a notch filter (60 Hz) and a bandpass filter (0.5−30 Hz). The electrical signals of the 3D cardiac muscle tissues, unless specified otherwise, were filtered through a bandpass filter (0.1−30 Hz). The FET sensitivity, noise level and delay between two action potential signals were also calculated in MATLAB (Supplementary Notes 3 and 14).

Electrical stimulation of the HL-1 cells. Platinum electrodes were used to stimulate the HL-1 cells and manipulate their firing patterns. We applied biphasic squared pulses (1 V, 1 Hz and 1 ms peak width) from an analogue output terminal of a commercial DAQ system (Digidata 1440, Axon) with commercial software (pCLAMP 10.3, Axon). The electrodes were placed ~10 mm away from the FETs.

Pharmacological and ion-concentration modulation of HL-1 cell electrophysiology. To explore the effects of drugs on cell electrophysiology we added channel blockers nifedipine (Sigma Aldrich or Abcam) or tetrodotoxin (Sigma Aldrich or Abcam) to typical Tyrode's solution. We also tuned the potassium or sodium concentration in the typical Tyrode's solution. The resulting solutions were administered by the perfusion (that is, simultaneously aspirating the old solution and adding the new solution) of cells. The electrical signals of the cells were recorded simultaneously. See Supplementary Note 15 for further discussions.

Engineering of cardiac microtissues. Neonatal rat cardiomyocyte tissues were engineered on a PDMS platform composed of a well and two microposts following the previously reported method[48] (Supplementary Fig. 34). Cardiomyocytes were mixed with collagen-based gel at a density of ~5 × 10^6 cells ml^{-1}. Each cell-laden hydrogel was added to the PDMS well around the two microposts and incubated for 1 h. Then, the culture medium was added to the cell-laden gels, followed by incubation. More details are provided in Supplementary Note 16.

Fluorescence staining of live cells. HL-1 cell membranes were marked with a cytoplasmic membrane dye (CellBrite), cell nuclei were stained with NucBlue and the PI layer in the FETs was mixed with rhodamine 6G dye. See Supplementary Note 17 for further discussions

Quantification and statistical analysis. The number of experiments and replicates is indicated in individual figure legends. The signal latencies in Fig. 4 were calculated by cross-correlating each two recording traces in MATLAB. The signal conduction velocities were calculated by linear regression of the signal latencies extracted from the raw data. The data presented in Figs. 2−5 were processed and visualized using MATLAB.

Reporting Summary. Further information on research design is available in the Nature Research Reporting Summary linked to this article.

References

48. Zhao, Y. et al. A platform for generation of chamber-specific cardiac tissues and disease modeling. *Cell* **176**, 913–927.e18 (2019).

Author contributions

S.X., N.K. and Y.G. conceived the idea. S.X., N.K. and Y.G. designed the device. Y.G., N.K., Chunfeng Wang, J.Z., J.M. and Y. Li, fabricated the device. Y.G. and N.K. took the optical and SEM images. Y.G., N.K. and T.M.W. measured the signals with the patch clamp. Y.G., J.S., D.Z., J.M., A.Y. and L.H.-H.H. cultured the HL-1 cells. T.M.W. and J.S. isolated the primary cardiomyocytes of neonatal and adult mice. R.N., S.A. and A.K. prepared the microtissues of neonatal rat cardiomyocytes. J.L. and P.J.B. mapped the FET surface capacitance. Y.G. carried out the finite element analysis simulations. Y.G., N.K., Chunfeng Wang, J.Z. and Z.H. characterized the device electrically. Y.G., N.K., H.G., A.Y. and D.Z. coated the phospholipid on the FET device. Y.G., A.Y. and J.M. performed the fluorescent staining and confocal microscopy imaging. Y.G. fabricated the MEA. Y.G., J.S. and D.Z. carried out the Ca²⁺ sparks screening assays. Y.G. and D.Z. tested the viability of HL-1 cells. Z.L. and M.L. designed the 10-channel preamplifier. Y.G., Z.H. and W.L. designed the cellular signal measurement set-up. Y.G., Chunfeng Wang, N.K., J.Z. and W.L. measured and analysed the cellular signals. Y.G. and J.Z. drew the schematics and took photographs of the devices. Y.G. carried out the pharmacological and ion-concentration modulation of the HL-1 cells. Y.G. stimulated the HL-1 cells electrically. All authors contributed to discussions on the data and commented on the manuscript.

Competing interests

The authors declare no competing interests.

Additional information

Extended data is available for this paper at https://doi.org/10.1038/s41565-021-01040-w.

Supplementary information The online version contains supplementary material available at https://doi.org/10.1038/s41565-021-01040-w.

Correspondence and requests for materials should be addressed to Sheng Xu.

Peer review information *Nature Nanotechnology* thanks Xinyan Tracy Cui and Chi Hwan Lee for their contribution to the peer review of this work.

Reprints and permissions information is available at www.nature.com/reprints.

a Part 1: silicon doping

i

SOI
(undoped)

ii

Heavily doped
Si and an
undoped line

iii

A patterned
Si FET

b Part 2: silicon FETs transfer printing

i

Si FETs
on BOX

ii

Partially
etched BOX

iii

Si FETs
underfilled
by PTFE

iv

Completely
etched BOX

v

Si FETs anchored by
PTFE on the carrier Si

vi PDMS

Si FETs picked up
by a PDMS stamp

vii

Si FETs transferred
to a new substrate
coated with PI

viii

Si FETs left on the
PI substrate after releasing
the PDMS stamp

c Part 3: device fabrication on new substrate

i

Etched PI
(first-layer)

ii

Defined metal
connection

iii

Defined PMMA
protection

iv

Defined PI
(second-layer)

v Hinges

Defined SU-8
structure

vi

Defined photoresist
sacrificial layer

vii PDMS

Device picked up
by a PDMS stamp

viii Water-soluble
tape

Device picked up by
the water-soluble tape

d Part 4: 2D to 3D device by compressive buckling

i Hinges

Bonding sites

Device transferred
to a prestrained
elastomer substrate

ii

Folded device at the
hinges by releasing
the prestrain

■	Undoped Si	■	Heavily doped Si	■	BOX
■	PTFE	■	Carrier Si	■	PDMS
■	First PI	■	Metal (Au)	■	PMMA
■	Second PI	■	SU-8	■	Photoresist
■	Water-soluble tape			■	Elastomer

Extended Data Fig. 1 | Schematics illustrating the fabrication steps of the 3D FET array. a, The FET's drain, source, and gate regions are determined on an n-type SOI wafer by doping. First, the undoped region (that is, the region with only the background doping from the wafer) is coated by a layer of SiO_2 as the barrier for spin-on dopants from diffusing into the silicon substrate. Second, the FET shape is defined by photolithography and reactive ion etching. **b**, The FETs are firstly anchored to the substrate by PTFE, and then are transferred using a PDMS stamp to a temporary 2D substrate coated with PI. **c**, Multi-layered polymers and metal are coated and patterned on the temporary substrate. Finally, the layered device is transferred to a PDMS stamp and picked up by a water-soluble tape. **d**, The FET array is transferred to a prestrained elastomer substrate and selectively bonded at the two pre-designed bonding sites. When the prestrain releases, the 2D FET array gets compressed and buckled up to form 3D geometries.
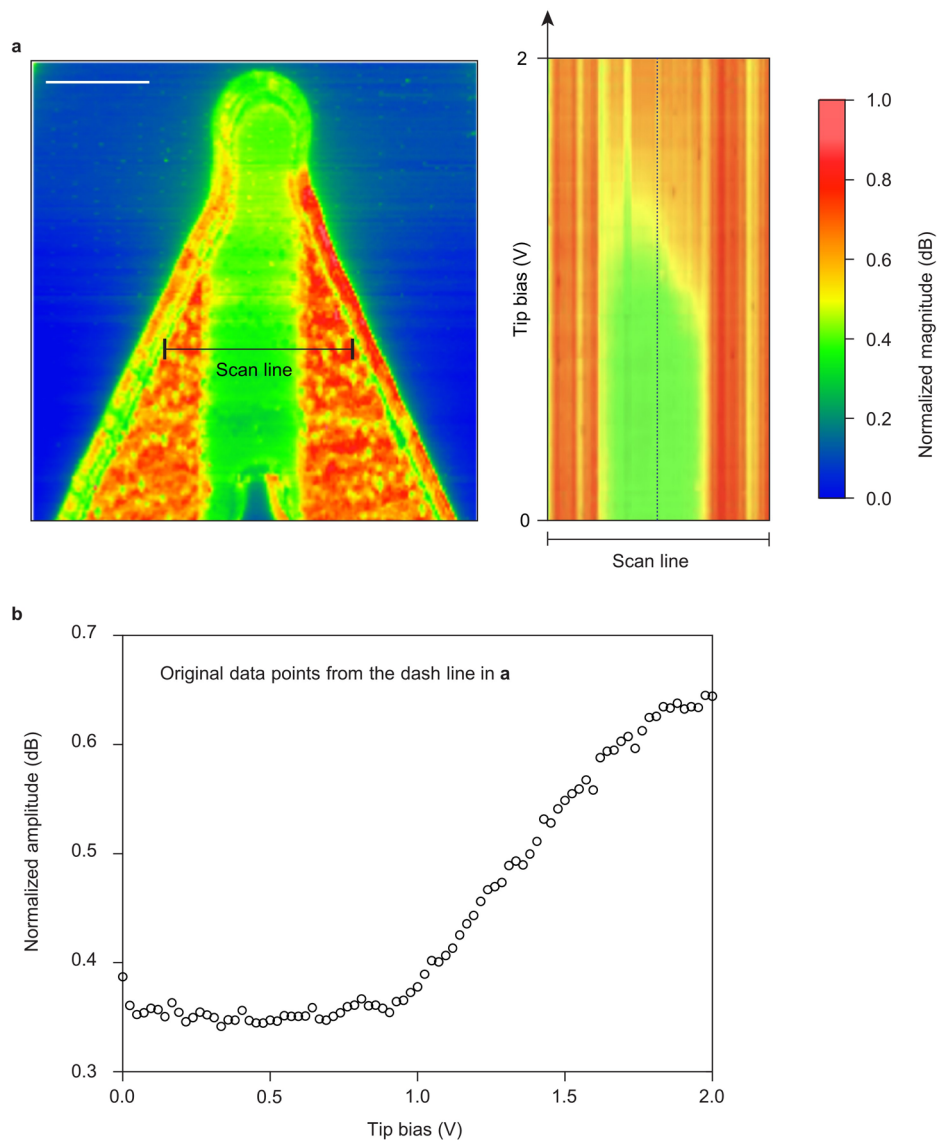
Extended Data Fig. 2 | Mapping FET's conductivity by an atomic force microscope with a bias applied by the scanning tip. a, A linear scan of the FET's conductivity was performed with a positive bias applied by the atomic force microscope. The results show a larger positive bias applied on the FET's lightly doped conduction channel yields a larger conductivity in the channel, which verifies the n-type properties of the FET's channel, which corresponds to the results by electrical transport characterizations. Scale bar: 2 μm. **b**, Original data points from the conductivity linear scan showing the FET's conduction channel turns 'ON' at the 1V tip bias. The 'threshold voltage' didn't appear in the water-gate characterization because we used a much smaller gate bias range for scanning the water-gate characterization. Additionally, we expect the FET device is 'ON' at zero bias because the middle region is also n-type with lots of free electrons. The discrepancy between the two measurements is from their different characterization mechanisms, including the gate capacitance, method of applying the gate bias, and the information that can be read from the signals.
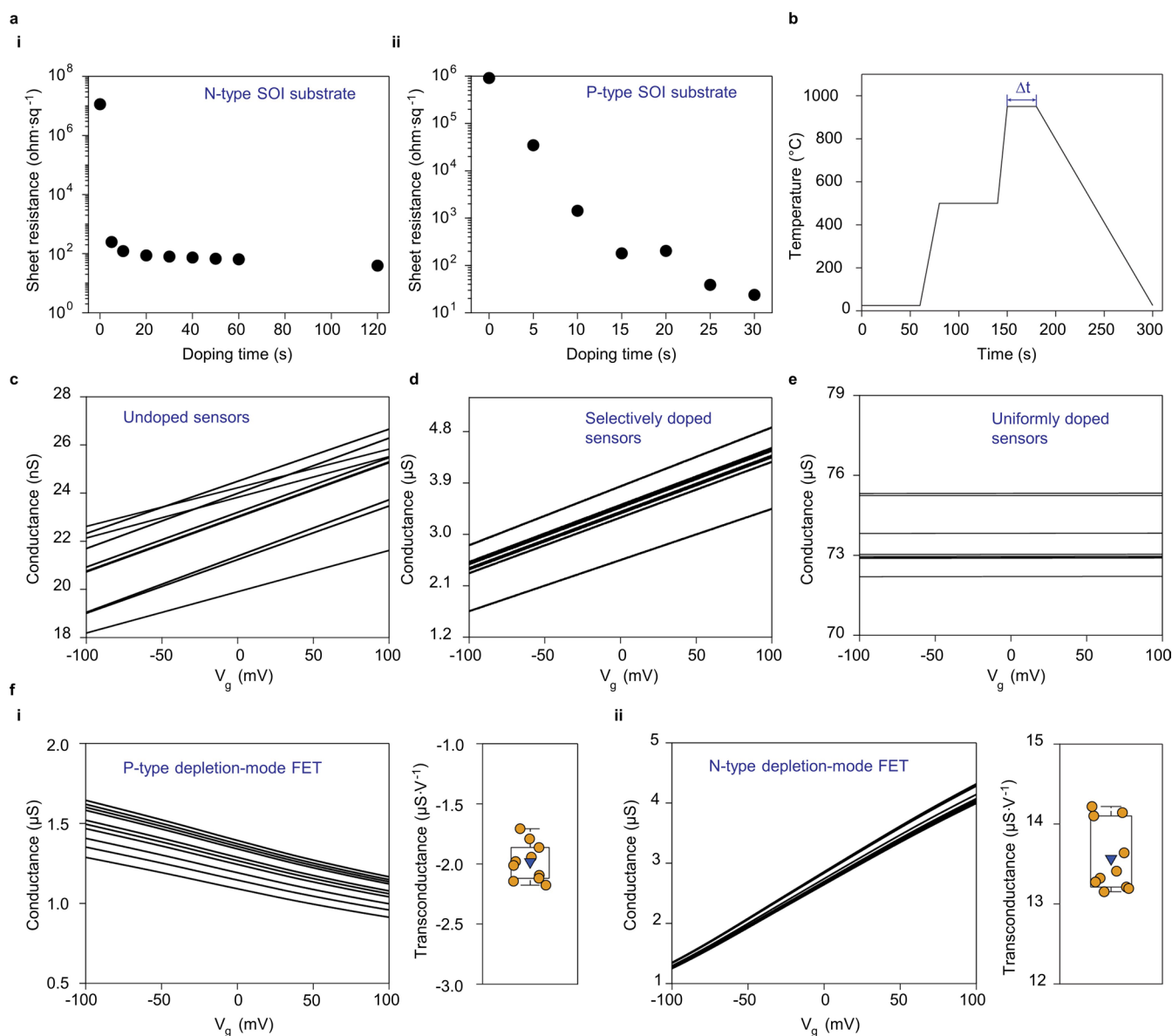
Extended Data Fig. 3 | Optimizing the FETs' electrical properties by tuning doping concentrations. a, Sheet resistances of (i) antimony doped SOI (N-type) and (ii) boron doped SOI (P-type) wafers, determined by high-temperature doping with phosphorus dopant (P509) at 950 °C for various doping times (Δt), which is defined as the period that the apex temperature was held during annealing. **b**, A typical temperature profile for driving the phosphorus dopants into the SOI wafer. The most effective doping period was at the highest temperature (950 °C), as indicated by Δt. A longer Δt generates a smaller sheet resistance of the SOI. We applied a two-step doping process: the first light doping was for the whole SOI that determined the FET's conduction channel's doping concentration; and the second heavy doping was for the whole SOI except the conduction channels. The resultant FET had an N^+NN^+ structure and worked under a depletion mode. **c-e**, Transfer characteristics of devices by various doping conditions, including (**c**) undoped, (**d**) selectively doped, and (**e**) heavily uniformly doped sensors. **f**, Transfer characteristics of (**i**) p-type and (**ii**) n-type depletion-mode FETs, showing that the n-type FETs demonstrate about six times larger transconductances (that is, sensitivities) than those p-type FETs. Therefore, we chose n-type depletion-mode FETs in this work.
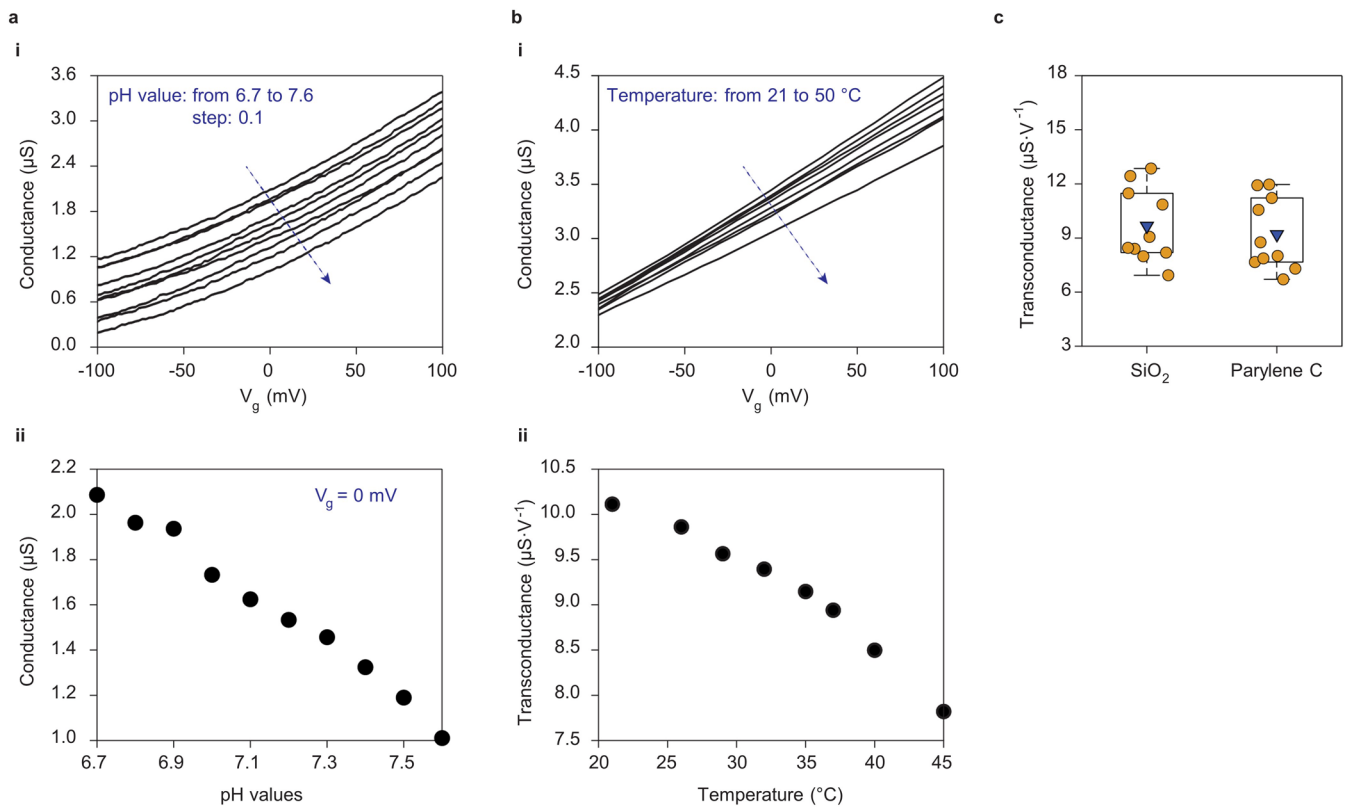
Extended Data Fig. 4 | FETs' reliability tests under various conditions. a, i, An FET's conductance with different pH of the gate solution. The transfer characteristics show high similarities, proving high reliability of the FET under various pH. The common pH for cell culturing is 7.4. **ii**, Extracted data points at zero gate bias, showing the conductance decreases with increasing the pH, giving another evidence of the n-type conductivity of the FET. **b, i**, An FET's transfer characteristics under different temperatures of the gate solution, showing the FET has excellent thermal stability and reliability under various temperatures. The common temperature for cell culturing is 37 °C. **ii**, Calculated transconductances showing the FET's transconductance decreases with increasing the temperature, which is due to the effectively reduced mobility of the charge carriers in the conduction channel. **c**, Parylene C was used as an additional gate dielectric material on top of the SiO_2 in the FET, considering SiO_2 might be soluble in biological fluids, such as extracellular solutions of cardiac muscle cells. The FETs' transconductance (that is, sensitivity) barely changed after coating the Parylene C.
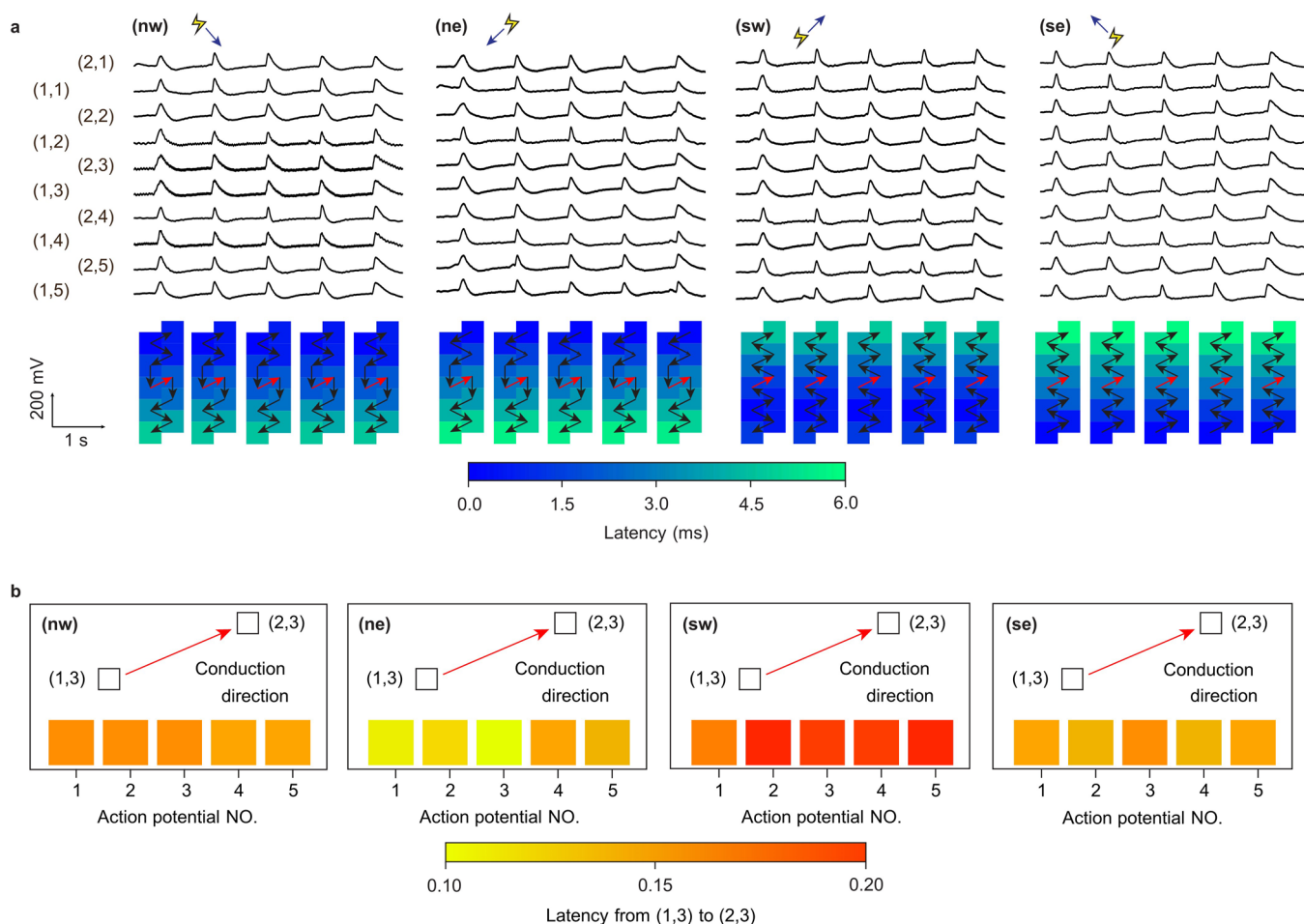
Extended Data Fig. 5 | Recordings of HL-1 cells' action potentials by a 10-FET array under electrical stimulation. a, Changing the stimulation electrode orientation from northwest (**nw**) to northeast (**ne**), southwest (**sw**), and southeast (**se**) will shift the directions of intercellular signal conductions. The first signal appeared in the FET that is relatively closer to the stimulation electrode and propagated among the cells per their coupling states, as indicated by the black arrows. The intercellular signal conduction velocity under electrical stimulation is from 35.1 to 39.3 μm·ms⁻¹. The variations in the velocity are caused by the fluctuations of temperature, pH value, and ion concentration in the cell culture medium. In all scenarios, the directions of intracellular signal conductions, as indicated by the red arrows, are always the same, that is, from (1,3) to (2,3). **b**, Schematics showing the latencies of intracellular signal conductions from (1,3) to (2,3).
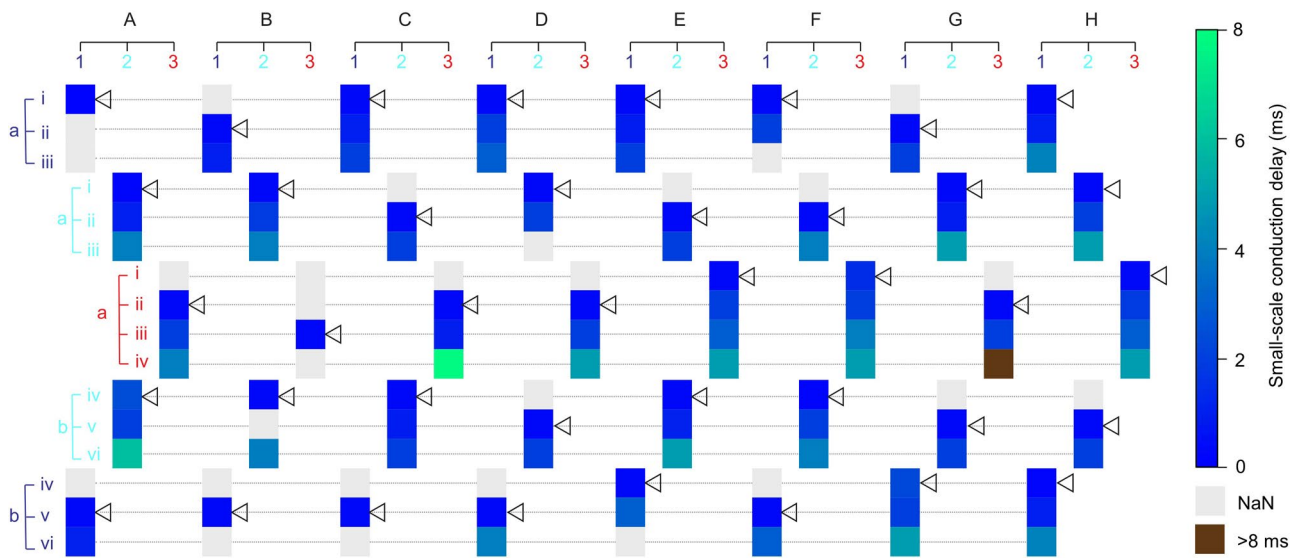
Extended Data Fig. 6 | Small-scale signal conduction within the cardiac tissue by the 128-FET array. The 128-FET array is classified into 40 units, where each arm has five units. Each unit is labelled by the combination of the located arm name (for example, 'A'), the loop number (for example, '1'), and the relative location (for example, 'a'). In each unit, the FETs are labelled in i, ii, iii, and iv. Within each unit, intercellular signal conductions via gap junctions in neighboring cells are analyzed, and the latencies are denoted in the heatmaps. The signal conduction velocity inside each unit can be calculated. For instance, in E2b, the signal transmits 70 μm from E2iv to E2vi in 5 ms. By analyzing all signal conductions within each unit, we calculated the small-scale conduction velocity (Supplementary Table 5), whose average and standard deviation are 18.8 ± 7.5 μm·ms⁻¹, which are consistent with previously reported values. The triangle for each unit indicates the selected FET that has the earliest spike within that unit. We use the selected FET in each unit as the reference point to calculate the signal conduction velocities among different units. NaN: Not a number, meaning no cellular signal was recorded.

nature portfolio

Corresponding author(s): Sheng Xu

Last updated by author(s): Aug 10, 2021

Reporting Summary

Nature Portfolio wishes to improve the reproducibility of the work that we publish. This form provides structure for consistency and transparency in reporting. For further information on Nature Portfolio policies, see our Editorial Policies and the Editorial Policy Checklist.

Statistics

For all statistical analyses, confirm that the following items are present in the figure legend, table legend, main text, or Methods section.

n/a	Confirmed	
☐	☒	The exact sample size (n) for each experimental group/condition, given as a discrete number and unit of measurement
☐	☒	A statement on whether measurements were taken from distinct samples or whether the same sample was measured repeatedly
☒	☐	The statistical test(s) used AND whether they are one- or two-sided *Only common tests should be described solely by name; describe more complex techniques in the Methods section.*
☒	☐	A description of all covariates tested
☒	☐	A description of any assumptions or corrections, such as tests of normality and adjustment for multiple comparisons
☐	☒	A full description of the statistical parameters including central tendency (e.g. means) or other basic estimates (e.g. regression coefficient) AND variation (e.g. standard deviation) or associated estimates of uncertainty (e.g. confidence intervals)
☒	☐	For null hypothesis testing, the test statistic (e.g. F, t, r) with confidence intervals, effect sizes, degrees of freedom and P value noted *Give P values as exact values whenever suitable.*
☒	☐	For Bayesian analysis, information on the choice of priors and Markov chain Monte Carlo settings
☒	☐	For hierarchical and complex designs, identification of the appropriate level for tests and full reporting of outcomes
☒	☐	Estimates of effect sizes (e.g. Cohen's d, Pearson's r), indicating how they were calculated

Our web collection on statistics for biologists contains articles on many of the points above.

Software and code

Policy information about availability of computer code

Data collection	The data recorded by 10-FET device and the patch-clamp were captured via Axon pCLAMP 10.3, and processed Matlab (MathWorks, USA). The data recorded by 128-FET devices was captured via DDC264 (Texas Instruments) and a customized acquisition interface (DDC264 Evaluation v3.0.4079.16447 Firmware version: 656)
Data analysis	Matlab R2019b, Fiji (ImageJ 1.53c)

For manuscripts utilizing custom algorithms or software that are central to the research but not yet described in published literature, software must be made available to editors and reviewers. We strongly encourage code deposition in a community repository (e.g. GitHub). See the Nature Portfolio guidelines for submitting code & software for further information.

Data

Policy information about availability of data

All manuscripts must include a data availability statement. This statement should provide the following information, where applicable:

- Accession codes, unique identifiers, or web links for publicly available datasets
- A description of any restrictions on data availability
- For clinical datasets or third party data, please ensure that the statement adheres to our policy

All data supporting the findings of this study are available within the Article and its Supplementary Information.

Field-specific reporting

Please select the one below that is the best fit for your research. If you are not sure, read the appropriate sections before making your selection.

☐ Life sciences   ☐ Behavioural & social sciences   ☐ Ecological, evolutionary & environmental sciences

For a reference copy of the document with all sections, see nature.com/documents/nr-reporting-summary-flat.pdf

Life sciences study design

All studies must disclose on these points even when the disclosure is negative.

Sample size	*Describe how sample size was determined, detailing any statistical methods used to predetermine sample size OR if no sample-size calculation was performed, describe how sample sizes were chosen and provide a rationale for why these sample sizes are sufficient.*
Data exclusions	*Describe any data exclusions. If no data were excluded from the analyses, state so OR if data were excluded, describe the exclusions and the rationale behind them, indicating whether exclusion criteria were pre-established.*
Replication	*Describe the measures taken to verify the reproducibility of the experimental findings. If all attempts at replication were successful, confirm this OR if there are any findings that were not replicated or cannot be reproduced, note this and describe why.*
Randomization	*Describe how samples/organisms/participants were allocated into experimental groups. If allocation was not random, describe how covariates were controlled OR if this is not relevant to your study, explain why.*
Blinding	*Describe whether the investigators were blinded to group allocation during data collection and/or analysis. If blinding was not possible, describe why OR explain why blinding was not relevant to your study.*

Behavioural & social sciences study design

All studies must disclose on these points even when the disclosure is negative.

Study description	*Briefly describe the study type including whether data are quantitative, qualitative, or mixed-methods (e.g. qualitative cross-sectional, quantitative experimental, mixed-methods case study).*
Research sample	*State the research sample (e.g. Harvard university undergraduates, villagers in rural India) and provide relevant demographic information (e.g. age, sex) and indicate whether the sample is representative. Provide a rationale for the study sample chosen. For studies involving existing datasets, please describe the dataset and source.*
Sampling strategy	*Describe the sampling procedure (e.g. random, snowball, stratified, convenience). Describe the statistical methods that were used to predetermine sample size OR if no sample-size calculation was performed, describe how sample sizes were chosen and provide a rationale for why these sample sizes are sufficient. For qualitative data, please indicate whether data saturation was considered, and what criteria were used to decide that no further sampling was needed.*
Data collection	*Provide details about the data collection procedure, including the instruments or devices used to record the data (e.g. pen and paper, computer, eye tracker, video or audio equipment) whether anyone was present besides the participant(s) and the researcher, and whether the researcher was blind to experimental condition and/or the study hypothesis during data collection.*
Timing	*Indicate the start and stop dates of data collection. If there is a gap between collection periods, state the dates for each sample cohort.*
Data exclusions	*If no data were excluded from the analyses, state so OR if data were excluded, provide the exact number of exclusions and the rationale behind them, indicating whether exclusion criteria were pre-established.*
Non-participation	*State how many participants dropped out/declined participation and the reason(s) given OR provide response rate OR state that no participants dropped out/declined participation.*
Randomization	*If participants were not allocated into experimental groups, state so OR describe how participants were allocated to groups, and if allocation was not random, describe how covariates were controlled.*

Ecological, evolutionary & environmental sciences study design

All studies must disclose on these points even when the disclosure is negative.

Study description	*Briefly describe the study. For quantitative data include treatment factors and interactions, design structure (e.g. factorial, nested, hierarchical), nature and number of experimental units and replicates.*
Research sample	*Describe the research sample (e.g. a group of tagged Passer domesticus, all Stenocereus thurberi within Organ Pipe Cactus National*

Research sample	*Monument), and provide a rationale for the sample choice. When relevant, describe the organism taxa, source, sex, age range and any manipulations. State what population the sample is meant to represent when applicable. For studies involving existing datasets, describe the data and its source.*
Sampling strategy	*Note the sampling procedure. Describe the statistical methods that were used to predetermine sample size OR if no sample-size calculation was performed, describe how sample sizes were chosen and provide a rationale for why these sample sizes are sufficient.*
Data collection	*Describe the data collection procedure, including who recorded the data and how.*
Timing and spatial scale	*Indicate the start and stop dates of data collection, noting the frequency and periodicity of sampling and providing a rationale for these choices. If there is a gap between collection periods, state the dates for each sample cohort. Specify the spatial scale from which the data are taken*
Data exclusions	*If no data were excluded from the analyses, state so OR if data were excluded, describe the exclusions and the rationale behind them, indicating whether exclusion criteria were pre-established.*
Reproducibility	*Describe the measures taken to verify the reproducibility of experimental findings. For each experiment, note whether any attempts to repeat the experiment failed OR state that all attempts to repeat the experiment were successful.*
Randomization	*Describe how samples/organisms/participants were allocated into groups. If allocation was not random, describe how covariates were controlled. If this is not relevant to your study, explain why.*
Blinding	*Describe the extent of blinding used during data acquisition and analysis. If blinding was not possible, describe why OR explain why blinding was not relevant to your study.*

Did the study involve field work? ☐ Yes ☐ No

Field work, collection and transport

Field conditions	*Describe the study conditions for field work, providing relevant parameters (e.g. temperature, rainfall).*
Location	*State the location of the sampling or experiment, providing relevant parameters (e.g. latitude and longitude, elevation, water depth).*
Access & import/export	*Describe the efforts you have made to access habitats and to collect and import/export your samples in a responsible manner and in compliance with local, national and international laws, noting any permits that were obtained (give the name of the issuing authority, the date of issue, and any identifying information).*
Disturbance	*Describe any disturbance caused by the study and how it was minimized.*

Reporting for specific materials, systems and methods

We require information from authors about some types of materials, experimental systems and methods used in many studies. Here, indicate whether each material, system or method listed is relevant to your study. If you are not sure if a list item applies to your research, read the appropriate section before selecting a response.

Materials & experimental systems

n/a	Involved in the study
☒	☐ Antibodies
☐	☒ Eukaryotic cell lines
☒	☐ Palaeontology and archaeology
☒	☐ Animals and other organisms
☒	☐ Human research participants
☒	☐ Clinical data
☒	☐ Dual use research of concern

Methods

n/a	Involved in the study
☒	☐ ChIP-seq
☒	☐ Flow cytometry
☒	☐ MRI-based neuroimaging

Eukaryotic cell lines

Policy information about cell lines

Cell line source(s)	Sigma Aldrich SCC065 and Dr. Xiaochen Jiang lab in Tufts University
Authentication	none of the cell line used were authenticated
Mycoplasma contamination	the cell lines were not tested for mycoplasma contamination
Commonly misidentified lines (See ICLAC register)	*Name any commonly misidentified cell lines used in the study and provide a rationale for their use.*

Supplementary information

Three-dimensional transistor arrays for intra- and inter-cellular recording

1
2
3
4 # Supplementary Information for
5
6 **Three-dimensional transistor arrays for intra- and inter-cellular recording**
7
8 **This PDF file includes:**
9 Materials and Methods
10 Supplementary Figs. 1–35
11 Supplementary Tables 1–5
12 References
13
14 **Other Supplementary Information for this manuscript include the following:**
15 Supplementary Videos 1–5
16

Table of Contents

90   **Materials and Methods**

91   **Materials**

Materials	Source
Biological Samples	
Red blood cell membranes	Gong et al. 2019 (ref. 16)
Chemicals, Peptides, and Recombinant Proteins	
CellBrite Cytoplasmic Membrane Dyes	Biotium; #30023
NucBlue™ Live ReadyProbes™ Reagent (Hoechst 33342)	Thermo-Fisher Scientific; R37605
18:1-12:0 NBD PC	Avanti; 810133; CAS: 190792-36-0
14:0 PC (DMPC)	Avanti; 850345; CAS: 18194-24-6
AZ 1505 Photoresist	AZ Electronic Materials USA Corp.
AZ 1512 Photoresist	EMD Performance Materials Corp.
AZ 1529 Photoresist	EMD Performance Materials Corp.
Negative resist NR9-3000PY	Futurrex, INC.
SU-8 2010	Microchem
Teflon™ AF amorphous fluoroplastics	The Chemours Company FC, LLC
PI-2545	HD MicroSystemsTM
VM651 Adhesion Promoter	HD MicroSystemsTM
N-Methylpyrrolidine, 97%	Sigma-Aldrich, Inc.
Acetone	Chemical Strategies, Inc.
Hydrochloric Acid	Avantor Performance Materials, LLC
Hydrofluoric Acid, 49%	Avantor Performance Materials, LLC
Buffered Oxide Etch 6:1	Avantor Performance Materials, LLC
Isopropyl Alcohol	Chemical Strategies, Inc.
Ammonia hydroxide, 29%	Avantor Performance Materials, LLC
Hydrogen peroxide, 30%	Avantor Performance Materials, LLC
MCC Primer 80/20	Microchem
495PMMA A11	Microchem
Resist Developer RD6	Futurrex, Inc.
AZ 300 MIF Developer	EMD Performance Materials Corp.
SU-8 Developer	Microchem
Fluo-4, AM, cell permeant	Thermo-Fisher Scientific; Cat#F14201
Experimental Models: Cell Lines	
HL-1 Cardiac Muscle Cell Line	Sigma-Aldrich; Cat#SCC065
Other	
SYLGARD® 184 Silicone Elastomer Kit	Dow Corning Corporation
Dragon Skin® 10 SLOW	Smooth-On, Inc.
Water-soluble Tape	Aquasol Corporation
Spin-On Diffusant B151 or P509	Filmtronics, Inc.
6-inch Silicon-on-insulator	University Wafer, Inc.
Krazy Glue (Cyanoacrylate)	Elmer's Products, Inc
Elform Heat Seal Connectors (anisotropic conductive film)	Yutek Tronic, Inc

FPC connector	MDFLY, Inc

92 **Software and Algorithms**

Software and Algorithms	Source
MATLAB custom code	This paper
pCLAMP	https://www.moleculardevices.com/systems/ conventional-patch-clamp/pclamp-10-software
Fiji	Schneider et al., 2012; https://imagej.net/ImageJ

93 **Equipment**

Equipment	Source
Oxford Plasmalab System 100	Oxford Instruments
Oxford PlasmaLab 80Plus	Oxford Instruments
Trion RIE/ICP Dry Etcher	Trion Technology
PE-100	Plasma Etch, Inc
Denton Discovery 18 Sputtering System	Denton Vacuum
Denton Vacuum Discovery 635	Denton Vacuum
ATC ORION Deposition Systems	AJA International, Inc
Oxford Plasmalab 80Plus PECVD	Oxford Instruments
Karl Suss MA6 Mask Aligner	Süss Microtec SE.
Vacuum Drying Oven ADP 3 1	Yamato Scientific Co., Ltd
PSD Series UV Ozone System	Novascan Technologies, Inc.
AccuThermo AW 610	Allwin21 Corp.
PDS 2010 Parylene Coater	Specialty Coating Systems Inc.

94

95 **Supplementary Notes 1–17**

96 **Supplementary Note 1 | Fabrication of the 3D field-effect transistor (FET)**

97 Fabrication of the stretchable 3D FET array involved standard micro/nanofabrication techniques,
98 as well as a newly designed transfer printing technique, and the unique compressive buckling
99 technique. Details are illustrated in Extended Data Fig. 1. All the equipment and
100 materials/chemicals used in the fabrication process are listed in Methods.

101 The 3D FET has a functional silicon transistor connected with gold conduction electrodes, which
102 are sandwiched by two polyimide (PI) structure layers. A poly(methyl methacrylate) (PMMA)
103 layer is holding and protecting the FETs during the sequential fabrication process. It would get
104 removed by acetone before releasing the prestrain and applying the compressive force. A relatively
105 rigid SU-8 layer serves as the mechanical support of the whole device. A photoresist layer defines
106 the bonding sites of the SU-8 to the prestrained elastomeric substrate.

107 **1.1. Si doping defining the FET's drain, source, and gate terminals (Extended Data Fig. 1a)**

108 **1.1.1. Preparation of the silicon substrate**

109 The device was fabricated on a silicon-on-insulation (SOI) wafer (University wafers, device
110 layer: 1.5 µm, oxide layer: 3 µm, carrier layer: 550 µm). SOI samples were diced by a diamond
111 dicing machine and cleaned thoroughly in an RCA (Radio Corporation of America) clean process
112 to remove all organic contaminations, particles, and SiO_2 on the wafer surface (Mixture solution
113 is Ammonia hydroxide (29%): hydrogen peroxide (30%): deionized (DI) water = 1: 1: 5 in volume;
114 The solution was heated to 140 °C, and the samples were boiled for 15 min; The oxide on the
115 silicon surface got removed by dipping the samples in buffered oxide etchant (BOE) 6:1 for 2–3

116 seconds followed by DI water rinsing). Next, the 1.5 μm silicon was thinned down to 400 nm by
117 dry etching (inductively coupled plasma–reactive ion etching (ICP-RIE); RIE: 30 W, ICP: 1,200
118 W, 18.0 mTorr, 20 °C, 25.0 sccm SF_6, 50.0 sccm C_4F_8, 120–180 s). Another dry etching process
119 (ICP-RIE; RIE: 200 W, ICP: 2,000 W, 50.0 mTorr, 15 °C, 50 sccm O_2, 1 min) removed the induced
120 C_4F_8 residue coated on the silicon surface.

121 **1.1.2. SiO$_2$ doping mask fabrication**

122 The sample was RCA cleaned again to remove any oxide or contaminants on the surface.
123 Alignment markers at the four corners of the sample were defined by photolithography (photoresist
124 NR-3000PY: spin-casting at 4,000 r.p.m. for 60 s, baking on a hotplate at 150 °C for 60 s, UV
125 irradiance at 220 mJ·cm^{-2}, post-exposure baking at 100 °C for 60 s, and developing for ~20 s with
126 developer RD6) and dry etching (ICP-RIE: 30 W, ICP: 1,200 W, 18.0 mTorr, 20 °C, 25.0 sccm
127 SF_6, 50.0 sccm C_4F_8, 60 s). The silicon on the alignment markers positions was thinner than the
128 other areas, providing optical contrast while aligning the photomask in subsequent fabrication
129 steps. Next, SiO_2 doping mask was fabricated by depositing a uniform 100 nm or 300 nm thick
130 oxide layer on the sample surface using plasma-enhanced chemical vapor deposition (PECVD; RF
131 power: 20 W, 1,000 mTorr, 350 °C, 117.0 sccm SiH_4, 710.0 sccm N_2O, 246 s), and the doping
132 mask patterns were defined by photolithography (photoresist AZ 1505: spin-casting at 4,000 r.p.m.
133 for 45 s, baking on a hotplate at 105 °C for 90 s, UV irradiance at 30 mJ·cm^{-2}, and developing for
134 ~15 s with developer AZ 300 MIF) and dry etching SiO_2 (RIE: 150 W, 30.0 mTorr, 20 °C, 25.0
135 sccm Ar, 25.0 sccm CHF_3, 720 s).

136 **1.1.3. Thermally driving dopants into the silicon**

137 The dopants were coated on the sample surface (spin-on diffusants, B151 or P509: spin-casting
138 at 3,000 r.p.m. for 10 s, soft baking on a hotplate at 200 °C for 15 min) and annealed in a rapid
139 thermal annealing furnace (RTA furnace: 950 °C for certain time referring to Extended Data Fig.
140 3b). During sample annealing, the dopants would diffuse into the silicon dioxide mask instead of
141 the underneath silicon, forming the selectively undoped regions. Then, the doping mask and the
142 excessive dopants got removed in BOE for ~15 min. After that, silicon probe structures were
143 defined by photolithography (photoresist AZ 1505: spin-casting at 4,000 r.p.m. for 45 s, baking on
144 a hotplate at 105 °C for 90 s, UV irradiance at 30 mJ·cm^{-2}, and developing for ~15 s with developer
145 AZ 300 MIF) and silicon dry etching (RIE: 30 W, ICP: 1,200 W, 18.0 mTorr, 20 °C, 25.0 sccm
146 SF_6, 50.0 sccm C_4F_8, 60 s) and a follow-up RCA clean to obtain contamination-free silicon samples
147 for FETs. It was notable that offsets in doping regions caused by misalignment of photolithography
148 and/or non-uniform doping induced by uneven spin-coating on the silicon surfaces would
149 introduce variations in the measured conductance and transconductance of the FETs.

150 **1.1.4. Characterization of the doping results**

151 The FET had a lightly doped conduction channel in the middle and two heavily doped source
152 and drain terminals on the sides. We characterized the doping concentration distribution by using
153 an atomic force microscope coupled with the scanning microwave microscopy function, as
154 described in the Methods section in the main text. The topography image in Fig. 1d reflects the
155 height profile of the FET surface. The height difference between the lightly doped middle region
156 and its two sides was due to the RIE etching of the SiO_2 when defining the doping mask that
157 covered the middle part. To dry etch the SiO_2, CHF_3 gas was applied, which could also react with
158 Si at a selectivity of 3:1. If there was any over-etching, the exposed Si would also be etched to
159 form a small step edge compared to the middle region protected by photoresist during the dry
160 etching. Over-etching was preferred over under-etching because we wanted to ensure the silicon
161 is completely exposed before casting spin-on-dopants to fulfill successful doping.

1.2. Transfer-printing of the FET sensors to a new substrate (Extended Data Fig. 1b)

1.2.1. Free the FET device structure from the oxide layer underneath

The 3 µm oxide layer (buried oxide: BOX) in the SOI was wet etched (hydrofluoric acid (HF) 49%: 140–160 s) to undercut the FET structures, and also left sufficient oxide residue to connect the FET structures to the carrier wafer. A layer of PTFE (polytetrafluoroethylene) (AF: PTFE (Amorphous Fluoroplastics Solution) was deposited: spin-casting at 1,000 r.p.m. for 60 s, baking on a hotplate sequentially at 110 °C for 5–10 min, 245 °C for 5 min, and 330 °C for 15 min) on the FET surfaces, and dry etched (RIE; 80 W, 50.0 mTorr, 35–40 °C, 50.0 sccm O_2, 10 s) to expose the silicon surface. As a result, the previous undercut portion of SiO_2 was filled with PTFE. Then, the rest of the SiO_2 was completely etched off by placing the samples in HF (49%) for 2–3 hours.

1.2.2. Preparation of a temporary 2D substrate for the FET structures

A temporary 2D substrate was needed to connect and encapsulate these FET structures in functional devices. The temporary substrate was prepared by sequentially coating Al (sputtering; 200 W, 3.0 mTorr, 10 sccm Ar, 5 min, ~60 nm), PMMA (495 A11: spin-casting at 4,000 r.p.m. for 60 s, baking on a hotplate at 180 °C for 1 min, ~800 nm), and SiO_2 (plasma enhanced chemical vapor deposition (PECVD); RF power: 20 W, 1,000 mTorr, 350 °C, 117.0 sccm SiH_4, 710.0 sccm N_2O, 82 s, ~100 nm). Here, the Al layer served as the sacrificial materials to be later etched away in hydrochloric acid (HCl, 37–38%) to release the FET device from the substrate. The PMMA and SiO_2 dual layers acted as the protection materials to firstly avoid HCl from attacking the metal connections at the Au/Cr/Si interfaces, and to secondly prevent chemicals in subsequent steps from over-etching the PI or PMMA.

1.2.3. Transfer-printing of the FET structures

The sample prepared in **1.2.1** was deposited with an anti-adhesive C_4F_8 layer (RIE: 5 W, ICP: 500 W, 18.0 mTorr, 20 °C, 10.0 sccm C_4F_8, 120 s) to reduce the adhesion between the silicon device and the transfer-printing stamp. A polydimethylsiloxane (PDMS; base: curing agent = 4:1 in weight ratio) stamp was used to press on the FET structures and quickly pick them up from the SOI carrier wafer. Dry etching (RIE: 80 W, 50.0 mTorr, 20 °C, 50.0 sccm O_2, 420 s) the picked-up silicon surface to completely remove all of the PTFE underneath the FETs and to activate the silicon surface. Next, PI (2545; spin-casting at 6,000 r.p.m. for 60 s, baking on a hotplate at 100 °C for 20 s, ~1.6 µm) was coated on the prepared temporary substrate as described in **1.2.2**. At the time the PI layer was baked for 20 s, we pressed the PDMS stamp with the activated FET surface contacting the PI and held on the hotplate for 1 min before slowly releasing the PDMS stamp from the substrate. Then the FET structures were successfully transfer-printed to the temporary substrate.

1.3. Fabrication of the 2D arrayed FETs (Extended Data Fig. 1c)

1.3.1. Determination of the FET shape

The C_4F_8 layer left on FET surfaces got removed by dry etching (RIE: 80 W, 50.0 mTorr, 35–40 °C, 50.0 sccm O_2, 10 s). Then we fully cured the PI layer (hard baking on a hotplate; 250 °C, 60 min). Its shape was determined by photolithography (photoresist AZ 1529: spin-casting at 4,000 r.p.m. for 45 s, baking on a hotplate at 95 °C for 120 s, UV irradiance at 350 mJ·cm^{-2}, and developing for ~40 s with developer AZ 300 MIF) and dry etching (RIE: 80 W, 50.0 mTorr, 35–40 °C, 40.0 sccm O_2, 10 sccm CF_4, 300 s).

1.3.2. Metallization for interconnections

A lift-off process was used to define the metal patterns for connecting the FETs by photolithography (photoresist NR-3000PY: spin-casting at 4,000 r.p.m. for 60 s, baking on a hotplate at 150 °C for 60 s, UV irradiance at 220 mJ·cm^{-2}, post-exposure baking at 100 °C for 60 s, and developing for ~20 s with developer RD6) and sputtering (chromium: 200 W, 3.0 mTorr, 5

208 sccm Ar, 30 s, ~5 nm; gold: 200 W, 3.0 mTorr, 5 sccm Ar, 5 min, ~100 nm). The metallization
209 was finalized after the samples were soaked in acetone for 15 min. Moisture induced in the lift-off
210 process got removed when the samples were baked in a vacuum oven at 100 °C for 10 min.

211 **1.3.3. Embedding a sacrificial layer for holding the FET sensors**
212 A PMMA layer was coated on the FETs for dual purposes: to protect the FETs during the
213 following fabrication process and to serve as a sacrificial layer to release the FETs from the PI
214 layer during the compressive buckling. Because PMMA is not photo-patternable by UV light in
215 photolithography, a combination of photolithography and dry etching process was employed to
216 pattern the PMMA layer. Given that PMMA is dissolvable in organic solvents such as acetone and
217 NMP that would be used to remove the photoresist after dry etching, we coated a thin layer of PI
218 on the PMMA before casting the photoresist. Notably, the PI is also photo-patternable and
219 dissolvable in basic developers such as AZ 300 MIF but is resistant to acetone. Herein, sequential
220 coating of PMMA (495 A11: spin-casting at 2,000 r.p.m. for 60 s, baking on a hotplate at 180 °C
221 for 1 min, ~1,250 nm) and PI (PI2545/NMP = 2:1 in volume; spin-casting at 3,000 r.p.m. for 60 s,
222 baking on a hotplate at 150 °C for 1 min, ~624 nm) followed by photolithography (photoresist AZ
223 1512: spin-casting at 4,000 r.p.m. for 60 s, baking on a hotplate at 95 °C for 60 s, UV irradiance
224 at 120 mJ·cm^{-2}, and developing for ~12 s with developer AZ 300 MIF) and dry etching (RIE: 80
225 W, 50.0 mTorr, 35–40 °C 50.0 sccm O_2, 150 s) defined the PMMA structure. The photoresist and
226 PI on top of the PMMA got removed by acetone and developer AZ 300 MIF, respectively.
227 Similarly, moisture was removed in the vacuum oven (100 °C, 5 min).

228 **1.3.4. Sandwiching the functional materials by a second PI layer**
229 An adhesion promoter for PI (VM651/DI water = 1:50 in volume; spin-casting at 3,000 r.p.m.
230 for 60 s, baking on a hotplate at 100 °C for 1 min) was cast before a second PI layer (PI2545; spin-
231 casting at 1,500 r.p.m. for 60 s, baking on a hotplate at 150 °C for 1 min, ~4,500 nm) was formed
232 to sandwich the FET sensors and the PMMA. Its pattern was established by photolithography
233 (photoresist AZ 1529: spin-casting at 4,000 r.p.m. for 45 s, baking on a hotplate at 95 °C for 120
234 s, UV irradiance at 350 mJ·cm^{-2}, and developing for ~40 s with developer AZ 300 MIF) and dry
235 etching (RIE: 80 W, 50.0 mTorr, 35–40 °C, 50.0 sccm O_2, 300 s). The PI was fully cured after
236 baking at 250 °C on a hotplate for 1 hour.

237 **1.3.5. Forming a mechanical support of the soft structure**
238 A relatively rigid and thick SU-8 layer provided structural support to the device. The second PI
239 layer was activated by oxygen plasma (RIE: 50 W, 50.0 mTorr, 35–40 °C, 50.0 sccm O_2, 10 s) to
240 bond with the SU-8 and prevent any delamination that might occur in the multi-layered device.
241 Photolithography (SU-8 2010: spin-casting at 4,000 r.p.m. for 30 s, baking on a hotplate at 95 °C
242 for 150 s, UV irradiance at 140 mJ·cm^{-2}, post-exposure baking at 95 °C for 210 s, and developing
243 for ~140 s with SU-8 developer) defined the SU-8 shape. Hard baking (100 °C on a hotplate, 1
244 hour) fully crosslinked the polymer chains of the SU-8.

245 **1.3.6. Adding a sacrificial layer to the compressive buckling process**
246 A photoresist layer served as the sacrificial material for releasing the non-bonded areas of the
247 device during the compressive buckling[1]. To fabricate such a layer, the SU-8 surface was activated
248 (RIE: 50 W, 50.0 mTorr, 35–40 °C, 50.0 sccm O_2, 30 s) before coating a photoresist layer followed
249 by photolithography (photoresist AZ 1529: spin-casting at 4,000 r.p.m. for 45 s, baking on a
250 hotplate at 95 °C for 120 s, UV irradiance at 350 mJ·cm^{-2}, and developing for ~40 s with developer
251 AZ 300 MIF).

252 **1.4. 2D to 3D transformation by the compressive buckling (Extended Data Fig. 1d)**
253 **1.4.1. Releasing the flexible device by removing the sacrificial metal layer**

254   The device had a stack of layers and was attached to the temporary substrate during the
255 fabrication processes as described above. To free the multi-layered device from the temporary
256 substrate, the Al layer was etched in HCl fume evaporated from HCl solution (37–38%). After 12-
257 hour etching, the Al was mostly gone, but device was still loosely anchored on the substrate by the
258 photoresist pattern and could be released from the substrate by the mechanical force of the stamp.

259   **1.4.2. Transfer-printing the device to a prestrained elastomer substrate**
260   A PDMS stamp picked up the device from the substrate. A cellulose-based, water-soluble tape
261 allowed retrieval of the device from the PDMS stamp. Next, a strip of elastomer (Dragon Skin)
262 was placed and prestrained on a uniaxial stretcher. The device and the dragon skin surfaces were
263 treated in ultraviolet-induced ozone (UVO) cleaner, with the UV lamp ~1 cm apart from their
264 surfaces, for 10 minutes. The device/tape was transferred on the UVO-treated elastomer surface
265 with press. The bonded structure was then baked in a convection oven at 80 °C for 10 min.

266   **1.4.3. Popping up the device by releasing the prestrain**
267   DI water and acetone removed the water-soluble tape and the PMMA and photoresist layers in
268 the device, respectively. The selectively bonded sites were located at middle places of the SU-8.
269 When the prestrain in the elastomer substrate was slowly released, the 2D structure transformed to
270 the 3D configuration gradually. Finally, the entire device was rinsed with BOE and DI water to
271 remove any oxide residues adhered to the device.

272   **1.5. Wiring the device and sterilization before interfacing with cells**
273   Before interfacing with cells, first, the entire device was wired using anisotropic conductive film
274 (ACF) cables, which were bonded to the backend flat printed circuit cable (FPC) connector board
275 (by aligning and pressing the cable on the tin leads with heating at 180 °C for 10 s). Second, the
276 device was coated by a bilayer of Parylene C (1 g) and SiO_2 (sputtering; 200 W, 3.0 mTorr, 50
277 sccm Ar, 10 min). Parylene C was used to protect the silicon FET from dissolving in the solution.
278 SiO_2 was used to generate a hydrophilic surface of the FET for binding with phospholipids. The
279 insulation layer was vital to maintain the FET's high sensitivity and material stability during the
280 measurement[2,3]. The device was soaked in 70% ethanol for half an hour and then treated by UV
281 for 1 hour for sterilization.

282

283 **Supplementary Note 2 | Signal analysis in scanning microwave microscopy**
284   The reflection coefficient of the microwave signal varies depending on the dielectric properties
285 of the sample at each scanned point; hence the conductivity can be mapped. In the experiment, we
286 particularly tuned the reference setting so we could verify if the corresponsive relationship between
287 the reflection coefficient and the uncalibrated conductivity was positive or negative[4,5].
288   To enhance the measurement sensitivity, a homemade interferometric system was developed.
289 The interferometric system contained a hybrid coupler that split the source microwave into two
290 coherent signals[4,5]. One signal went to the probe, and the other to a tunable attenuator and phase-
291 shifter. Both signals got reflected: the former one was reflected by the sample, and the latter
292 reflected by the tunable attenuator and phase-shifter. The two reflected signals were combined at
293 the output of the coupler and canceled each other after proper tuning. The resulting signal was
294 amplified and measured by the network analyzer in the transmission mode. With proper tuning,
295 the system operated at its best sensitivity; small conductivity changes could be detected.
296   A linear scan of the FET tip area was performed to verify the doping results. In Extended Data
297 Fig. 2, the conduction channel's conductivity increased with a greater bias applied by the atomic
298 force probe, which showed convincing evidence that the FET had an n-type channel. The
299 conductivity went up when the tip bias was ~1 V, representing the threshold voltage to turn "ON"

300   the FET. Notably, the FET was engineered to have an N^+NN^+ structure which meant it was in a
301   depletion-mode at the "ON" state with zero gate bias, as shown in the water-gate characterizations
302   in Fig. 2. The plausible contradiction here could be due to the different mechanisms of the
303   characterization approaches, where the gate capacitance, method of applying the gate bias, and the
304   information that could be read from the signals were different, which have been well studied [6].
305   The difference of the ON/OFF voltage range between the tip-gate and the ion water-gate is mainly
306   caused by that the ion water-gate has a much bigger gate capacitance (double-layer capacitance),
307   so that a small gate-voltage can result in a larger carrier density change in the semiconductor
308   channel, hence affect its conductance greatly. The tip gate capacitance is small; hence it needs a
309   bigger voltage to reach the same switch effect.
310
311   **Supplementary Note 3 | Calculation of the membrane potential recorded by the FET**
312   Each FET's gate terminal was electrically coupled with the ionic solution, so ionic flows in the
313   solution would change the electrical field and thus conductance in the conduction channel of the
314   FET by electrostatic interactions. An FET sensed the electric field potential on its gate terminal
315   and translated the value by its current readout through its conduction channel. The translational
316   factor is defined by the transconductance of the FET, which we also used to define an FET's
317   sensitivity. The transconductance g_m is defined as:

318 $$g_m = \frac{\Delta I_{ds}}{\Delta V_g}, (1)$$

319   where I_{ds} is the current in the conduction channel of the FET and V_g is the electric field potential
320   on the gate, which also represents the membrane potential in recording the cellular signals. After
321   measuring the transconductance of the FET, we can correspond the current in the conduction
322   channel to the gate potential by the following formula:

323 $$I_{ds} = V_g \times g_m, (2)$$

324   In the case of cell membrane potentials, it can be written as:

325 $$I_{ds} = V_m \times g_m, (3)$$

326   where V_m is the membrane potential, i.e., the action potential. The FET sensor was cascaded to a
327   current preamplifier where the current was amplified and converted into a voltage reading and fed
328   into the downstream data acquisition (DAQ) system. The DAQ then digitalized the voltage signal
329   as the computer readout, which could be expressed as:

330 $$V_r = I_{ds} \times \beta, (4)$$

331   where V_r is the voltage readout in the DAQ and β is the amplification of the preamplifier. We can
332   establish the relationship between the membrane potential, V_m, and the voltage readout, V_r, by
333   substituting equation (3) into equation (4):

334 $$V_r = V_m \times g_m \times \beta, (5)$$

335   Or

336 $$V_m = \frac{V_r}{g_m \times \beta}, (6)$$

337   The amplification β is a known value, which was pre-set at its design period. The transconductance,
338   g_m, can be determined by the slope of the line plot of I_{ds}-V_g in the water-gate characterization of
339   the FET sensor, seen in Fig. 2c and d. Therefore, we can accurately obtain the recorded intra- or
340   extra- cellular membrane potentials by the voltage readouts.
341
342   **Supplementary Note 4 | Justification of using the n-type depletion-mode FET (N^+NN^+) and**
343   **optimization of the sensitivity-to-noise ratio**
344

345   The significant difference between a depletion-mode and an enhancement-mode FET is whether
346   it is "ON" at zero gate bias, where the depletion-mode FET already has charges in the conduction
347   channel ("ON") without a gate bias. The feature is beneficial for the FET biosensors to operate in
348   an aqueous environment because we can avoid the large gate bias required to turn on the FET,
349   which would generate irreversible faradaic reactions such as electrolysis of water. Further, the
350   depletion-mode FETs show high sensitivity and thus have been extensively used to detect weak
351   signals in biological systems[7].

352   We prepared a p-type and an n-type depletion-mode FET arrays. These two arrays had the same
353   structure and dimensions. Each array had ten FETs with heavily doped source and drain regions
354   (p-type: ~10 ohm·sq^{-1}; n-type: ~10^2 ohm·sq^{-1}) and an undoped gate region (p-type: ~10^6 ohm·sq^{-1}
355   ; n-type: ~10^7 ohm·sq^{-1}). In Extended Data Fig. 3f, transfer characteristics of both devices showed
356   that the n-type FETs demonstrated about six times larger sensitivity than the p-type FETs.
357   Therefore, we chose the n-type depletion-mode FET in this work.

358   Optimizing the doping levels in the drain, source, and gate regions of the N^+NN^+ FET yielded
359   the largest sensitivity-to-noise ratio of the FETs. In this process, we lightly doped the gate region
360   for 1~20 seconds (Fig. 2a). Before doping, the SOI wafer had a background doping level (antimony
361   doped), making its sheet resistance ~10^7 ohm·sq^{-1}. The sheet resistances of lightly and heavily
362   doped silicon were 10^4 ohm·sq^{-1} and 10^2 ohm·sq^{-1}, respectively.

363   To improve the sensitivity-to-noise ratio, ideally, we want to increase the sensitivity and, in the
364   meantime, decrease the noise level of the FET. However, these two properties would show a
365   positive relationship between each other. In electrophysiological experiments, electrical
366   measurement noises can arise from current fluctuations in the cell membrane, the sensors, the
367   preamplifier electronics, and/or external sources such as power lines, computers, monitors, and
368   many other devices located in the vicinity of the measurement setup[8].

369   External noises can be largely reduced by the application of electromagnetic shielding, such as
370   using a faradaic cage to isolate the cells and sensors from the surrounding electronics. However,
371   internal noises represented by current or voltage signal fluctuations cannot be avoided. These
372   noises often show in low-frequency regions, so called low-frequency noise. Generally, thermal
373   noise, shot noise, pink noise (i.e., flicker noise or 1/f noise), and generation-recombination noise
374   represent the common internal noises in a transistor sensor[9]. Pink noise and generation-
375   recombination noises are frequency-dependent and are high in the low frequency.

376   The positive relationship between the noise level and the FET's sensitivity is in two aspects.
377   First, there was external noise during the electrical measurement even a faradaic cage was
378   implemented. These noises were amplified by the FETs. Thus, a FET of higher sensitivity leads to
379   a higher level of noises. Second, in a model describing the sensitivity of silicon nanowire
380   transistors to the gate charge, the transistor's sensitivity would increase by decreasing the doping
381   concentration[10]. At the same time, lower doping concentration would elevate the noise level of the
382   transistor. Therefore, we can conclude a positive relationship between the transistor sensitivity and
383   the noise.

384

385   **Supplementary Note 5 | Characterization of the FET's response time to input gate signals**
386   The response time of an FET shows its switching characteristics. The typical switching
387   frequency of the silicon FET is in the megahertz range, corresponding to the response time of
388   hundreds even tens of nanoseconds[11]. The response time of an FET is primarily affected by the
389   input capacitance (such as the gate-source capacitance and gate-drain capacitance)[12]. For an FET
390   sensor that interacts with cells, the FET must accurately retain fast and slow cellular signals,

391 including opening and closing of rapid sodium ion channels (~1 ms)[13], initiation of an action
392 potential of cardiomyocytes (~1 ms)[13,14], and activation of fast transient outward current of
393 potassium ions and chlorine ions (<10 ms)[13,15]. It herein requires the FET to show the fast response
394 to cellular signals with a wide bandwidth, which means the frequency range that the biosensor can
395 maintain a stable amplitude of the detected signals. Within this range, the amplitude of the recorded
396 signals by the FET is almost fixed with little fluctuations.
397   Here, we characterized the FET's response time by applying a rapid signal on its gate terminal
398 using a similar configuration to that of the water-gate characterization. We used an arbitrary
399 waveform generator (Model 3390, Keithley) to generate a pulse signal (rising/falling time: 5 ns,
400 duration: 0.1 ms, amplitude 100 mV) and fed it to the FET. In Supplementary Fig. 5a, the
401 corresponding FET's output signal indicated a response time of 600~700 ns, much shorter than the
402 recorded signal latencies between FETs, which were in the microsecond range. It proved the FET
403 sensor had sufficiently fast response to external signals and therefore could faithfully record rapid
404 cellular electrical signals.
405
406 **Supplementary Note 6 | Characterization of the FET's sensitivity by the water-gate method**
407   The measurement system is illustrated in Supplementary Fig. 4, where the FET was connected
408 to preamplifiers, DAQ (e.g., DigiData 1440A), and downstream to a computer graphic user
409 interface (GUI; for example, Axon pCLAMP 10 Software Suite).
410   The ionic solution such as the phosphate-buffered saline (PBS; Sigma-Aldrich, pH = 7.4;
411 temperature = 37 °C) or typical Tyrode's solution (NaCl 140 mM, KCl 4 mM, $CaCl_2$ 1.8 mM,
412 $MgCl_2$ 1 mM, HEPES (4-(2-hydroxyethyl)-1-piperazineethanesulfonic acid) 10 mM, glucose 10
413 mM, pH = 7.35 with NaOH, temperature = 37 °C) was added on the FET's gate surface. An
414 Ag/AgCl electrode was immersed in the solution and applied a potential sweep from -100 mV to
415 100 mV to the solution. In the meantime, a positive potential (e.g., 200 mV) was fed to the FET's
416 source terminal.
417   The FET's drain terminal conducted currents to the downstream preamplifier. With a change in
418 the gate potential, the corresponding change in the source to drain current could be recorded and
419 plotted in the GUI. The FET's sensitivity was finally defined by the slope of the FET's transfer
420 characteristic plot.
421   It was notable that in the FET's temporal response to rapid signals (Fig. 2g-i), sometimes there
422 was overshoot, which was caused by the capacitance between the metal wires, dielectric layers,
423 and the ionic solution. These three layers formed a parallel plate capacitor. In the water-gate
424 characterization, the ionic solution and thus the gate signal were covering everywhere. Therefore,
425 the metal-induced capacitance would affect the characterization result. However, in the cellular
426 measurement, the local cellular signal is applied to the FET locally, but not on anywhere else, so
427 we could safely neglect the capacitance effect in the cellular measurements[12].
428
429 **Supplementary Note 7 | HL-1 cell culture protocol**
430   The HL-1 cardiomyocytes were purchased from Sigma-Aldrich.
431   To prepare the cells for signal recordings, the cells were cultivated on thin PDMS sheets (base
432 material: curing agent = 10:1; prepared by spin-casting the mixed precursors on a 4-inch wafer at
433 500 r.p.m. for 60 s, baking in a convection oven at 80 °C for 4 hours).
434   Before cell plating, the PDMS sheet was cut into 3 cm by 3 cm square and placed in a 35 cm
435 cell culture dish. The PDMS sheet was soaked in 70% ethanol for 30 min, followed by ultraviolet

436 sterilization for 1 hour. Fibronectin/Gelatin (5 µg·ml^{-1} fibronectin in 0.02% gelatin solution, 1 ml)
437 was coated on the pre-treated PDMS surface for at least 1 hour before seeding the cells.
438   After removing the coating agent, the cells (at a density of ~1 × 10^5 cm^{-2}) were plated and
439 maintained in the supplemented Claycomb medium (10% fetal bovine serum, norepinephrine 0.1
440 mM, L-Glutamine 2 mM, and penicillin/streptomycin 100 U·ml^{-1}/100 µg·m^{-1}, 2 ml) in an incubator
441 at 37 °C and 5% CO_2. The cell culture medium was replaced by a 2 ml fresh medium every day
442 until the cells reached confluency in 3–4 days.
443   Sterilizing the MEA and the FET before plating the cells followed the same procedure as the
444 abovementioned. Fibronectin/Gelatin was coated on the MEA surface before cell seeding to
445 enhance cell attachment.
446
447 **Supplementary Note 8 | Primary cardiomyocyte culture protocol**
448   **8.1. Neonatal mouse cardiomyocytes**
449 The neonatal mouse ventricles were predigested in HBSS (Hank's Balanced Salt Solution) (0.5
450 mg·ml^{-1}) containing Trypsin (0.5 mg·ml^{-1}) at 4 °C on an orbital shaker at 80 r.p.m. for overnight,
451 and then were thoroughly digested in collagenase (330 U·ml^{-1}) and HBSS (0.8 mg·ml^{-1}) mixed
452 solution.
453   Isolated cells were suspended in the cell culture medium (Dulbecco's Modified Eagle Medium:
454 M199 = 4:1 in volume, penicillin/streptomycin 120 U·ml^{-1}/100 µg·m^{-1}, L-Glutamine 2 mM,
455 HEPES 10 mM, 10% Horse Serum, 5% Fetal Bovine Serum). The cells were plated in a T-75 flask
456 to remove the adherent fibroblast cells.
457   The suspended cardiomyocytes were transferred to a PDMS sheet in a 35-cm dish pre-coated
458 with laminin (1 µg·ml^{-1} laminin in sterile 1X PBS). The cells were incubated at 37 °C in a
459 humidified incubator with 10% CO_2. The medium was replaced on a daily basis.
460   **8.2. Adult mouse cardiomyocytes**
461   Adult mouse hearts were isolated via aortic perfusion with a buffered perfusion solution (NaCl
462 113 mM, Na_2HPO_4 0.6 mM, $NaHCO_3$ 12 mM, KCl 4.7 mM, $KHCO_3$ 10 mM, KH_2PO_4 0.6 mM,
463 $MgSO_4·7H_2O$ 1.2 mM, HEPES 10 mM, Taurine 30 mM, phenol red 0.032 mM, glucose 5.5 mM,
464 temperature = 37 °C; pH = 7.35 with NaOH) to fully remove all blood from the vasculature. A
465 1mg/mL collagenase type 2-containing digestion buffer digested the matrix of the heart during
466 perfusion at a rate of 3 ml·min^{-1}. Once the heart was sufficiently digested, the ventricles were
467 removed and minced with scissors before being triterated in warmed solution (90% perfusion
468 solution, 10% fetal bovine serum, 12.5uM calcium chloride) with a transfer pipette. Cells were
469 strained through 100um mesh and stepwise, slowly brought to 1mM calcium concentration. Then
470 they were transferred to a 35 cm dish pre-coated with laminin (1 µg·ml^{-1} laminin in sterile PBS
471 solution). The cells were incubated at 37 °C in a humidified incubator with 5% CO_2 for 4 hours
472 before measurements.
473
474 **Supplementary Note 9 | Surface functionalization of the FET by the phospholipids**
475   Two types of phospholipid bilayers were used in the experiments including a synthetic lipid
476 bilayer and a natural cell membrane. These two types of lipid bilayer membranes had different
477 advantages and were preferred in different applications. The natural cell membranes were
478 structurally and functionally similar to those of the host cells so they could express specific cellular
479 biomarkers (e.g., CD47) in the membranes to mimic the cellular surface to the greatest extent[16].
480 Hence, we could use these natural cell membranes without additional modification. Red blood cell
481 membranes have been widely used for nanoparticles coatings in fields of drug delivery, vascular

482 injury repair, and tumor imaging because of the simplicity of the isolation process[17-21]. On the
483 other hand, the synthetic phospholipids showed higher flexibility for engineering and modification
484 and superb stability. Besides, synthetic lipids were usually less expensive than natural cell-derived
485 membranes.

486   The synthetic lipid bilayer was made of DMPC (1,2-Dimyristoyl-sn-glycero-3-phosphocholine)
487 from Avanti, and the extracted red blood cell membranes were obtained by following established
488 protocols[12,17,22]. We added the fluorescent material into the phospholipid bilayers for
489 characterization purposes (Supplementary Fig. 7a). We skipped this step when preparing the
490 phospholipid coatings on the FET sensors used for signal recordings. Ideally, the lipid bilayer
491 could naturally merge with the cell membrane. However, in reality, the spontaneous fusion would
492 get affected by other materials in the cellular context, such as collagen. The fusion process took
493 some time to form a perfect interface. Plus, the cell could expel the FET out of its body even after
494 the sensor internalization (called the elastic response from the cytoskeleton)[23,24]. The coatings
495 could be repeatedly used for intracellular measurements of different cells for about three times.
496 After that, the phospholipid coating became worn and torn, making it difficult to get stable
497 intracellular recordings, or even no signals at all.

498   The critical step in the preparation of the phospholipid bilayers was to generate high-surface-
499 energy small lipid vesicles that could spontaneously form a lipid coating layer on the FET surface.
500 A step-by-step description of the coating process is introduced below.

501   **9.1. Removing the organic solvent in the received lipid solutions.**
502   The received synthetic phospholipids were dissolved in chloroform solutions in glass vials. We
503 removed the chloroform solvent and prepared aqueous lipid solutions. To achieve that, purging
504 nitrogen gas overnight desiccated the chloroform thoroughly in a glass vial.

505   **9.2. Re-hydrating the lipids in DI water.**
506   The phospholipids were re-hydrated with the DI water and immediately transferred to a plastic
507 vial. Here, importantly, using the plastic vials specifically was to prevent the hydrophilic segment
508 of the phospholipid bilayer from attaching to the glass vial walls.

509   **9.3. Breaking the large phospholipids aggregates into small unilamellar vesicles (SUVs).**
510   The mixture in the aqueous solution underwent a freeze-and-thaw process (freeze in the liquid
511 nitrogen and thaw in a water bath of 37 °C) for at least five times to break the multi-lamellar lipid
512 vesicles into unilamellar vesicles. The later sonication treatment was also employed to disperse
513 the lipid vesicles separately in the solution and eliminate any aggregation of small lipid vesicles.
514 The next step of preparing the lipid solution was to extrude the mixture solution through a PTFE
515 syringe filter. Only the small unilamellar vesicles would be left in the prepared solution. These
516 SUVs had high surface energy so they could self-assemble to become a uniform lipid coating on
517 the FET surface. Note that for natural red blood cell membranes, they are in bilayered vesicle
518 structures upon collection for natural cells. They only need to undergo this extrusion process to
519 generate unilamellar small vesicles.

520   **9.4. Applying the SUVs solutions on the FETs.**
521   To coat the lipid bilayers on the FETs, we applied the lipid solution to the FETs and put them in
522 an incubator at 37 °C to sit for at least two hours. Spontaneous lipid fusion took place at such a
523 higher temperature than the lipid's transition temperature (24 °C for DMPC). After that, removing
524 the excessive lipid solutions gently by DI water completed the functionalization.

525

526 **Supplementary Note 10 | Justification of the action potential morphologies**

527   Cells show different physiological characteristics even though they are of the same type or even
528 in the same cell culture. For example, in the same culture, some cells are contractile, but some are
529 not; also, some cells are spontaneously firing action potentials, but some are not. Their actual
530 action potential shapes of different cells would have slight differences as well[25]. Plus, as a
531 cancerous cell line, HL-1 cells would mutate during proliferation and reproduction, so their
532 physiological characteristics would vary from different cell passages (i.e., how many times they
533 have reproduced themselves)[26]. In different literature, the action potential morphologies of HL-1
534 cells were not identical[27-30].
535
536 **Supplementary Note 11 | Fabrication of the multi-electrode array (MEA)**
537   The MEA in this study had multiple conductive electrodes that were extracellularly contacting
538 cellular membranes and recording the membrane potentials. We used these devices to verify the
539 cardiomyocytic electrophysiological activities. The collected extracellular signals served as a
540 control for those recorded by the FET.
541   **11.1. Cleaning the glass substrate**
542   The first step was to clean cover glass slides (35 mm by 50 mm by 0.13–0.16 mm; Fisherbrand[TM])
543 to remove all organic contaminants and particles in stabilized sulfuric acid and hydrogen peroxide
544 mixture solution (Nano-Strip; VWR International, heating up to 80 °C for half an hour), followed
545 by rinsing with DI water and drying with nitrogen gas.
546   **11.2. Fabricating the metal connection layouts**
547   A lift-off process allowed forming metal connection patterns on the glass slides. The process
548 involved photolithography (photoresist NR-3000PY: spin-casting at 4,000 r.p.m. for 60 s, baking
549 on a hotplate at 150 °C for 60 s, UV irradiance at 220 mJ·cm^{-2}, post-exposure baking at 100 °C for
550 60 s, and developing for ~20 s with developer RD6) and then sputtering (chromium: 200 W, 3.0
551 mTorr, 5 sccm Ar, 30 s, ~5 nm; gold: 200 W, 3.0 mTorr, 5 sccm Ar, 5 min, ~100 nm). The samples
552 were soaked in acetone overnight to thoroughly remove all photoresists and lift off the metals on
553 the top of the photoresists.
554   **11.3. Depositing the insulation layer**
555   A thin layer of SU-8 was coated to insulate most of the metal wires and only expose the metal
556 electrode pads, by photolithography (SU-8 2000.5: spin-casting at 4,000 r.p.m. for 30 s, baking on
557 a hotplate at 95 °C for 60 s, UV irradiance at 100 mJ·cm^{-2}, post-exposure baking at 95 °C for 60
558 s, and developing for ~60 s with SU-8 developer). Hard baking at 180 °C for an hour cured the
559 SU-8 completely so that the SU-8 was safe and compatible with cells during measurements.
560   **11.4. Assembling a container for the cell culture medium**
561   A conical centrifuge tube (Falcon[TM]) was cut at 3 cm apart from the threaded dome. The flat top
562 surface was adhered to the center of the MEA using a low toxicity silicone adhesive (Kwik-Sil[TM],
563 World Precision Instruments) to build a container for the cell culture medium (Supplementary Fig.
564 18a).
565   **11.5. Wiring and sterilizing the device**
566   We used silver epoxy (8831, MG Chemicals) to connect the metal leads of the MEA to flexible
567 cables and the backend circuit. The device was sterilized in 70% ethanol for 5 hours before use.
568
569 **Supplementary Note 12 | Electrophysiological measurements by the whole-cell patch-clamp**
570   Whole-cell current patching on HL-1 cells and primary cardiomyocytes were performed with
571 external solution (for all types of cells: NaCl 140 mM, KCl 4 mM, MgCl$_2$ 1 mM, HEPES 10 mM,

572 glucose 10 mM, temperature = 37 °C; for HL-1 cells: $CaCl_2$ 1.8 mM, pH = 7.35 with NaOH; for
573 primary cells: $CaCl_2$ 1.0 mM, pH = 7.4 with NaOH).

574   Glass pipettes were pulled from borosilicate glass using a micropipette puller (Model P-87,
575 Sutter Instrument Co.). The as-pulled glass pipettes were then filled with an internal solution (NaCl
576 10 mM, KCl 10 mM, K-Aspartate 120 mM, $MgCl_2$ 1 mM, HEPES 10 mM, MgATP 5 mM, pH =
577 7.2 with KOH). The glass pipettes had an average impedance of 2–5 MΩ measured in the cell
578 medium bath.

579   Junction potentials were zeroed before the formation of the membrane–pipette sealing. Several
580 minutes after the seal was formed, the membrane was ruptured by gentle suction to establish the
581 whole-cell configuration for current clamping. Cell capacitance was measured by integrating the
582 capacitive transient evoked by applying a 5 mV hyperpolarizing step from a holding potential of -
583 40 mV.

584   Schematics in Supplementary Fig. 12 illustrate the electrical system of the patch-clamp platform,
585 including an Ag/AgCl electrode connected with a headstage for amplifying the recorded signals
586 by a feedback circuit. The headstage connected to an amplification system (Axonpatch 200B) and
587 a data digitalization module (DigiData 1440A, Axon). Current-clamp command pulses were
588 generated by a digital-to-analog converter (DigiData 1440A, Axon) controlled by the pCLAMP
589 software (10.3, Axon). After the cells were stimulated by an injection current, action potential
590 spikes could be recorded and shown in the GUI.

591   The small discrepancy between the results from the FETs and the patch-clamp is within the
592 standard cellular signals' fluctuation range due to differences in cellular physiology and
593 measurement setups.

594

595 **Supplementary Note 13 | Electrophysiological signal acquisition**
596   **13.1. The acquisition system for the 10-FET array**
597   The experimental setup for sensing cellular electrophysiology by the 10-FET array consisted of
598 a commercial DAQ system (DigiData 1440A) and a customized 10-channel preamplifier shown
599 in Supplementary Figs. 20 and 21. The setup was similar to that used for water-gate
600 characterization, where cells were placed on the FET with a zero bias from the Ag/AgCl electrode.
601 The sampling rates applied for the recordings were within the range from 10 to 100 kHz.

602   Electrical characterization showed no crosstalk between different channels in the preamplifier
603 (Supplementary Fig. 22). By hooking up the preamplifier to the DAQ, PC, and the 10-FET array,
604 each FET in the array operates independently, showing no crosstalk with each other
605 (Supplementary Fig. 19).

606   **13.2. The acquisition system for the 128-FET array**
607   The DAQ system consisted of a DDC264 (Texas Instruments) and a customized acquisition
608 interface to the evaluation board (Supplementary Fig. 31). The DAQ was connected to the FET
609 sensor arrays using ACF cables and an adaptive printed circuit board. Customized software (Texas
610 Instruments) controlled the DAQ system. All recordings by the 128-FET array in this study used
611 a sampling rate of 500–1,000 Hz, which was large enough to ensure the signal's fidelity, and small
612 enough to meet the limited capacity of the chip memory for on-board data storage.

613

614 **Supplementary Note 14 | Signal processing and analysis**
615   **14.1. Calculations of the FET's sensitivity and noise level**
616   The FET's sensitivity and noise level were analyzed and computed in MATLAB. The sensitivity
617 was represented by the slope of the FET's water-gate characterization plot. To obtain the slope, a

618 linear fitting of the plot was performed. The noise's amplitude was calculated from the same plot.
619 First, we substituted every gate potential (x-coordinate) into the fitting function to get a new set of
620 values, which represented the recordings without noise. Second, we subtracted the new values
621 from the originally recorded (y-coordinate) values and got the pure noise signals. Third, the
622 difference between the maximal and minimal values of the noise signals represented the peak-to-
623 peak amplitude of the noise.

624 **14.2. Signal latency calculation by the cross-correlation method**
625 Supplementary Fig. 25 introduces the cross-correlation method to calculate the latency between
626 two action potential spikes. The computation was conducted in MATLAB using the cross-
627 correlation function. To calculate the latency between any two action potentials, we first chose the
628 simultaneous recordings from different FET sensors, such as (2,1) and (1,1) in Extended Data Fig.
629 5. We selected a fixed duration of data that contained an action potential recorded by (2,1) and
630 (1,1). The latency between these two data sections was calculated by the cross-correlation method.
631

632 **Supplementary Note 15 | Modulation of HL-1 cells' electrophysiology by adding drugs or**
633 **changing the ion concentrations in the culture solutions**
634 Cellular electrophysiology can be modulated by drugs. These drugs act as ion channel blockers
635 that can affect ionic influx and/or efflux across the cellular membrane so they can modulate cellular
636 electrophysiology that can be reflected by the action potential morphology. In this work, the cells'
637 responses to nifedipine or tetrodotoxin (TTX) were studied. Nifedipine is an L-type calcium ion
638 blocker and TTX is a sodium ion blocker. To prepare the drug solutions, we added nifedipine or
639 TTX to the typical Tyrode's solution.
640 Changing the ion concentrations in the extracellular medium would also impact cellular
641 electrophysiological characteristics. For instance, abnormal solutions with above normal
642 potassium concentration (a.k.a. hyperkalemia) or below normal sodium concentration (a.k.a.
643 hyponatremia) in the culture medium can interfere with the proper electric signals. In this
644 experiment, we prepared solutions containing doubled concentrations of potassium ions for
645 hyperkalemia and half concentrations of sodium ions for hyponatremia studies.
646 After the drugs or the abnormal solutions were administered to the cells, it took several minutes
647 to affect the action potential recordings. Replacing the solutions with drugs or abnormal
648 concentrations of ions back with the typical Tyrode's solution by perfusion would recover the cell's
649 normal electrophysiological characteristics.
650

651 **Supplementary Note 16 | Cardiac microtissues engineering**
652 3D microtissues exhibit large similarity to the native tissue in the natural state[31], providing value
653 for studying organ development, disease progression, and effectiveness of certain drugs. Therefore,
654 it is attracting more attention as the biological model for pathology and pharmaceutical studies of
655 cardiovascular diseases.
656 The PDMS platform consisted of two or more micro-posts and one well to construct the
657 microtissues was fabricated. A master mold was designed using AutoCAD (Autodesk Inc., USA)
658 and made of PMMA using laser ablation (Supplementary Fig. 34c). Sticking the PMMA to the
659 Petri dish formed a mold for curing PDMS (Dow Corning, Sylgard™ 184, USA, base:curing agent
660 ratio 20:1, heated at 80 °C for 2 hours, Supplementary Fig. 34d). After proper sterilization, the
661 fabricated PDMS platform (within the well and around the microposts) was filled with a collagen-
662 based hydrogel with a density of 3 mg·ml^{-1}. The cell culture media was a mixture of Dulbecco's

663 Modified Eagle Medium (DMEM) (Gibco, USA), 10% fetal bovine serum (Gibco, USA), and 1%
664 penicillin-streptomycin (Lonza, USA). Cells were incubated at 37 °C with 5% CO_2.
665   Measurements were conducted three days after cell seeding in the PDMS platform and forming
666 the tissue compaction (Supplementary Fig. 34e). Supplementary Fig. 30 shows the measurement
667 setup of the 128-FET array, which included a customized DAQ system based on a commercial
668 current input analog-to-digital converter (TI DDC264). Each channel could operate independently
669 with no crosstalk. The system had a fixed amplification of 13.81 $V \cdot nA^{-1}$ (Supplementary Fig. 31).
670
671 **Supplementary Note 17 | Fluorescence staining of the HL-1 cells and the FET**
672   We conducted fluorescence staining and confocal microscopy imaging to show the cell/FET
673 interfaces. In this work, live cell staining was performed using NucBlue (ThermoFisher Scientific)
674 and CellBrite (Red; Biotium). The HL-1 cells were incubated at 37 °C for 15 minutes and 20
675 minutes after adding CellBrite and NucBlue dyes, respectively. To visualize the FET device, we
676 mixed 0.1 $mg \cdot ml^{-1}$ rhodamine 6G dye (Sigma Aldrich) in the PI layer during the device fabrication.
677 The device would emit green fluorescence, as shown in Fig. 4f and Supplementary Fig. 28.
678   Confocal imaging was carried out using a Leica SP8 confocal microscope with lightning
679 deconvolution. Confocal images were acquired using 405, 647, and 488 nm to excite components
680 labeled with NucBlue, CellBrite, and Rhodamine 6G fluorescent dyes, respectively. Fiji (ver.
681 2.1.0/1.53c) was used for analyzing the confocal images.
682

Supplementary Figures
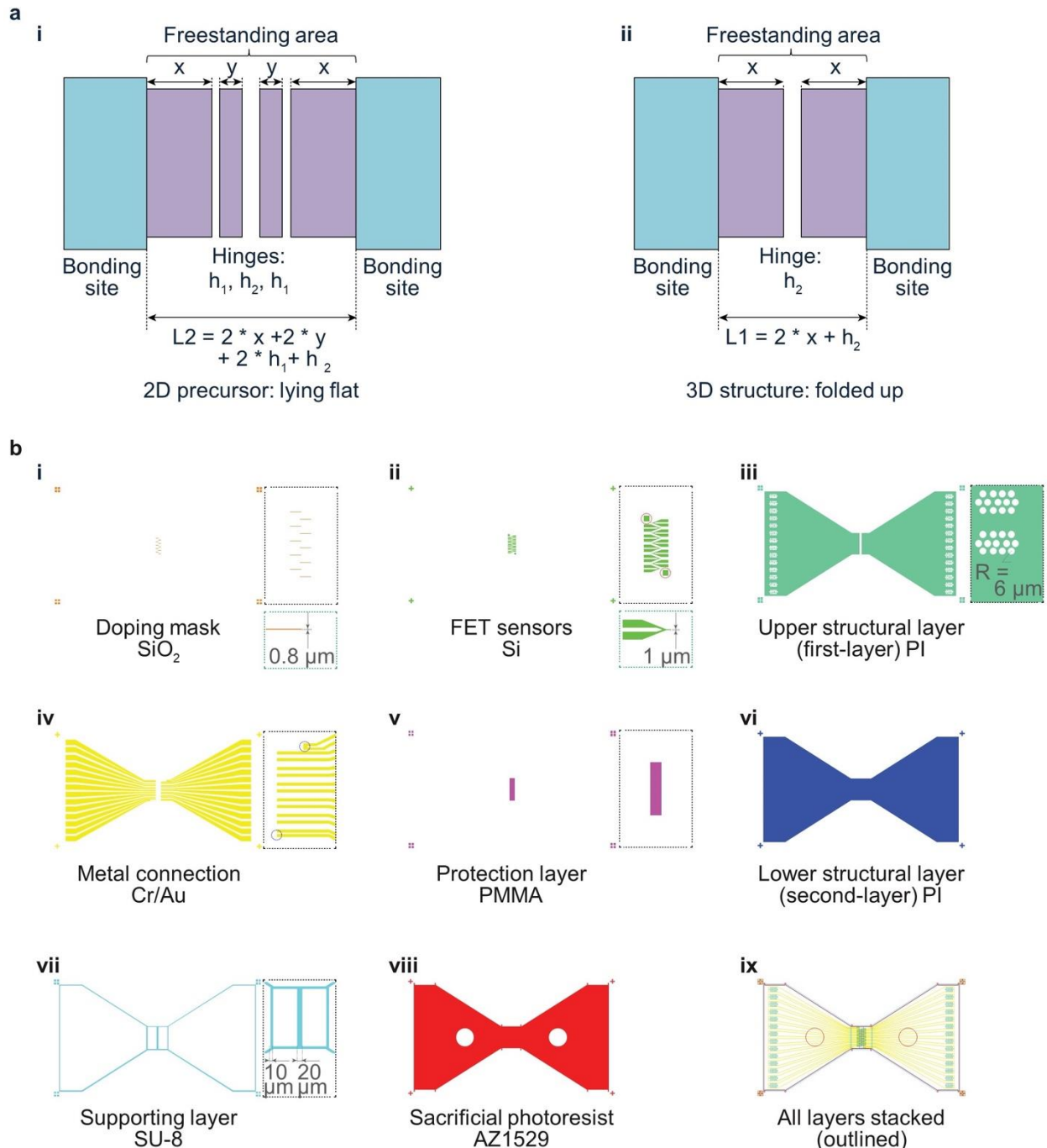
Supplementary Fig. 1 | Structural design of the arrayed FETs. a, Schematics showing the design principle of the 2D precursor of a 10-FET array. The applied prestrain on the dragon skin elastomer is defined by (L2 - L1)/L1. **b**, The CAD designs of the FETs showing the unique features of every layer of the device. Each layer has four alignment markers at corners for photolithography. (**i**) The doping line is 0.8 μm wide by photolithography. (**ii**) The sensors' tips are 1–2 μm wide, which can provide high sensitivity and spatial resolution while minimizing invasiveness to the cells and forming tight sealings during measurements[22]. Two square pads highlighted by the red dashed circles in the inset image serve to check the quality of metal connections with silicon after

693   soaking in acid solution for several hours. (**iii**) The holes shown in the inset image are designed to
694   expose the metal connections for bonding with external connective wires (e.g., ACF cables). (**iv**)
695   In the inset image the black dashed circle on the top indicates a metal loop that is used for checking
696   connections after compressive buckling. The black dashed circle at the bottom are the wires
697   connecting to the square silicon pad in (**ii**). (**v**) PMMA holds the ten FETs together during the
698   fabrication and gets removed during compressive buckling. (**vi**) The second PI layer has the same
699   layout as the first one. (**vii**) In this design, the middle hinge (h_2) is 20 µm wide. (**viii**) The shape of
700   the bonding site can be circular, square, or rectangular. A circular shape in this case makes the
701   compressive strain more evenly distributed on the bonding area and prevents delamination of the
702   device from the elastomer substrate.

a Si FETs left on the PI substrate

b Etched PI (first/upper layer)

c Defined metal connection

d Defined PMMA protection

e Defined PI protection (second/lower layer)

f Defined SU-8 structure

g Defined photoresist sacrificial layer

h Device picked up by a PDMS stamp
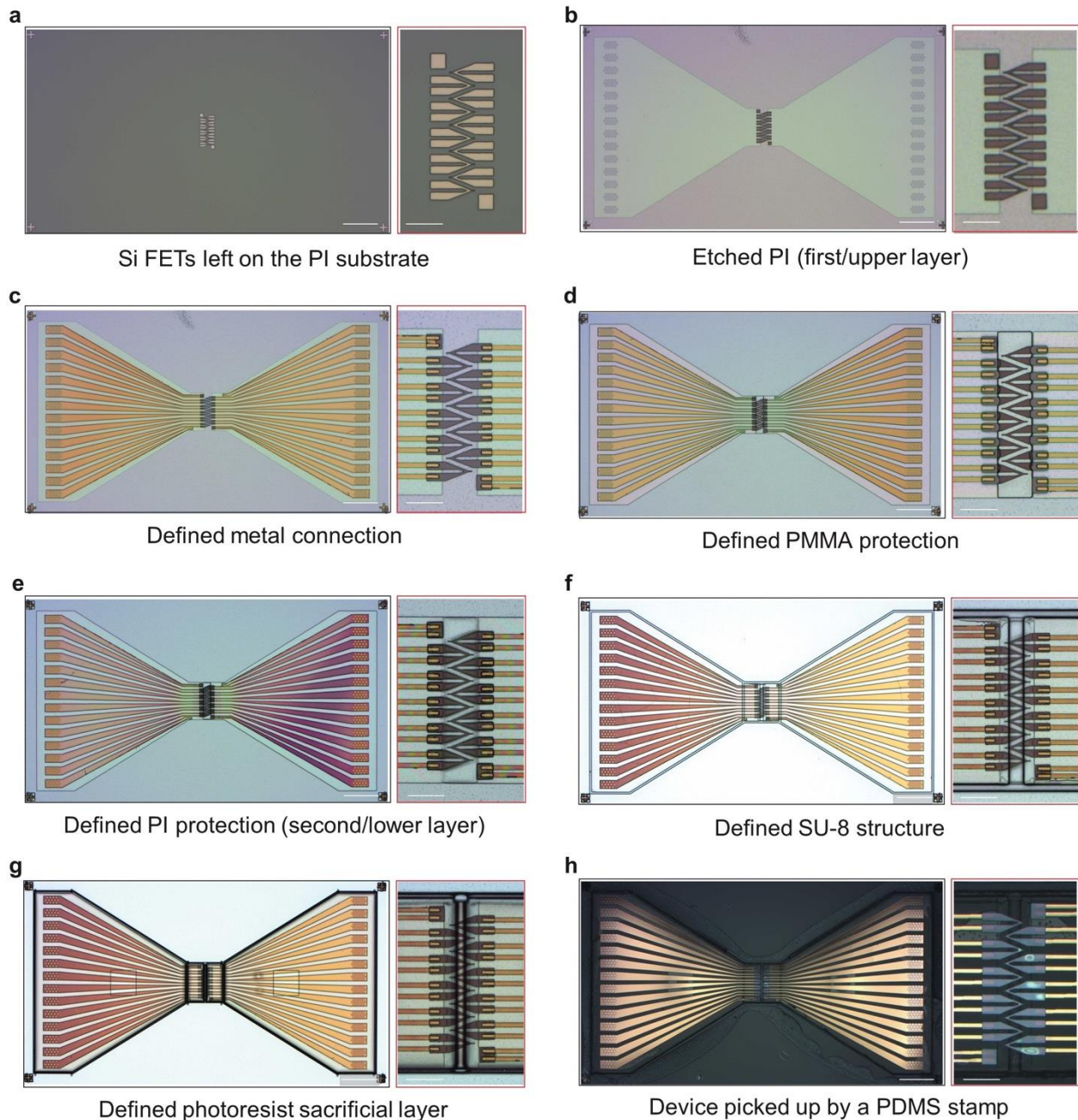
Supplementary Fig. 2 | Optical microscopical images illustrating the fabrication steps of the arrayed FETs. a, The FETs have been doped by spin-on diffusants on the SOI wafer. **b**, The sensors are transfer-printed to a temporary substrate coated with PI (first/upper layer). **c-g**, Multi-layered polymers and metal are formed in steps of spin coating, sputtering, and photolithography on the temporary substrate. **h**, Finally, the multi-layered 2D device is transferred to the PDMS stamp. The scale bars on each panel, left: 200 μm, right: 50 μm.

21
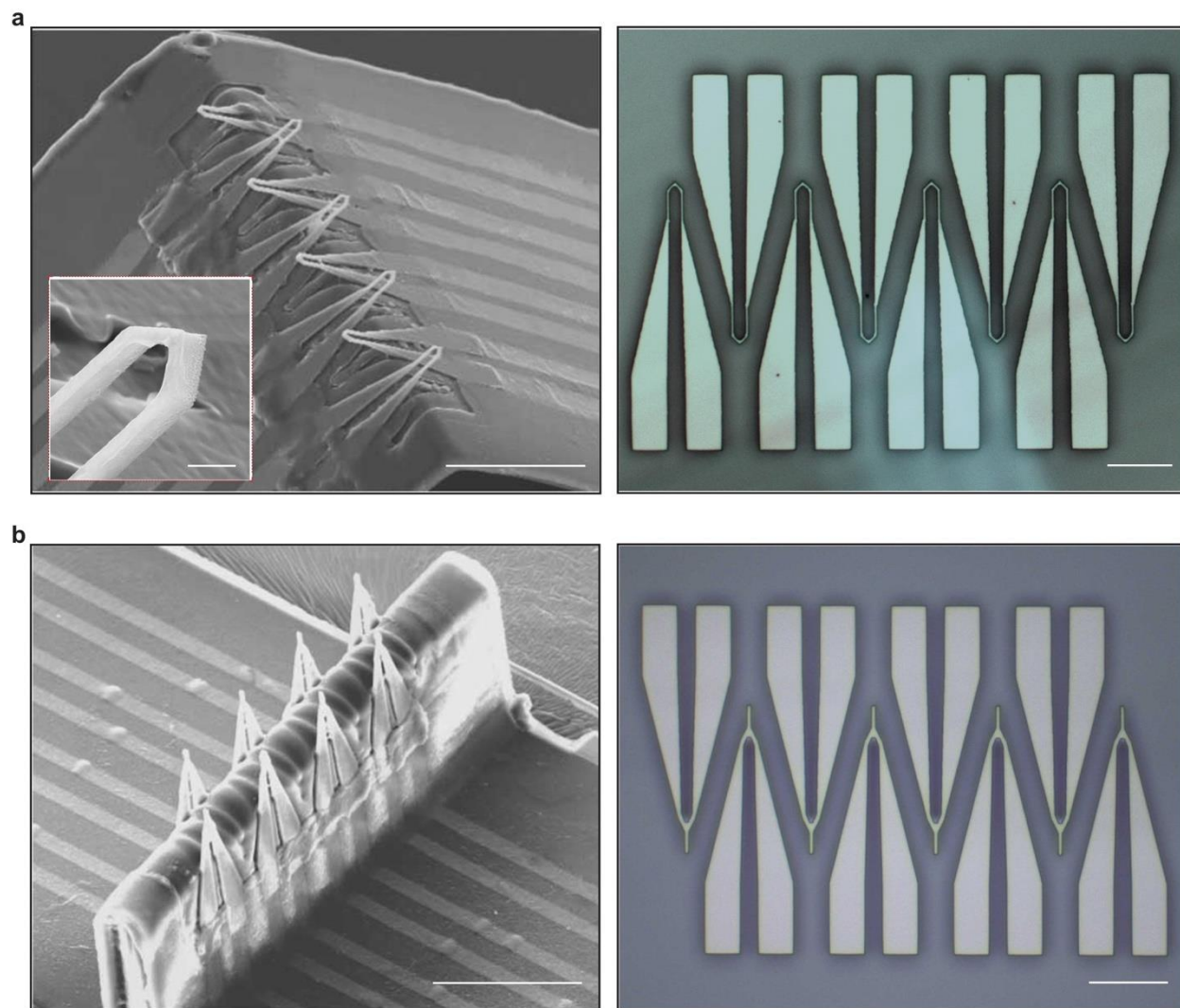
Supplementary Fig. 3 | Versatile designs of the FET shape. Scanning electron and optical microscopical (SEM and OM) images of FETs of two representative structural designs. **a**, An SEM image of an eight-FET array after buckling (top) and an OM image of them in 2D (bottom). Each sensor has a kinked tip defined by e-beam lithography (inset). This structure is mimicking a reported nanowire probe with a similar kinked tip[22]. The prestrain is only halfway released to enlarge the distance between the two rows of probes, thus covering a larger sensing area. **b**, An SEM image of an eight-FET array with sharp tips for minimal invasiveness to the cells (top) and an OM image of them in 2D (bottom). The FET's tip is 1 μm wide and 10 μm long. Scale bars: 50 μm in the top two SEM images; 2 μm in the inset image of (**a**); 20 μm in the bottom two OM images.
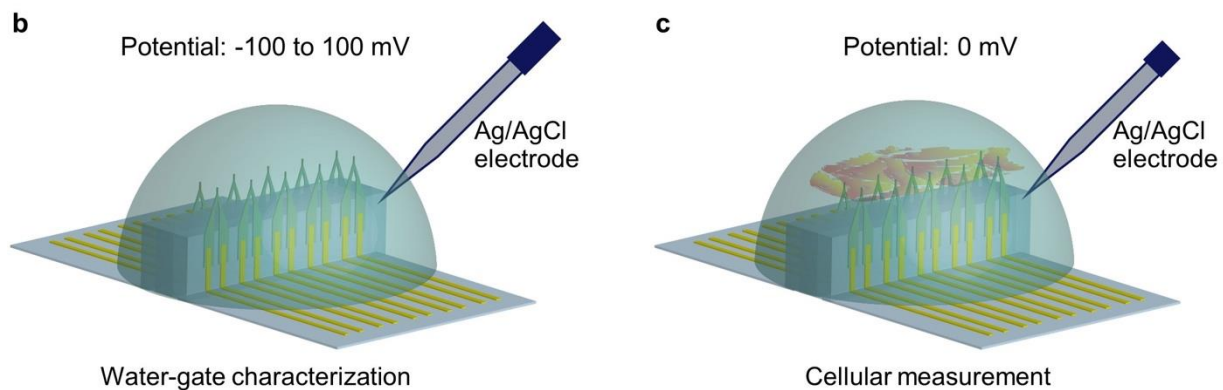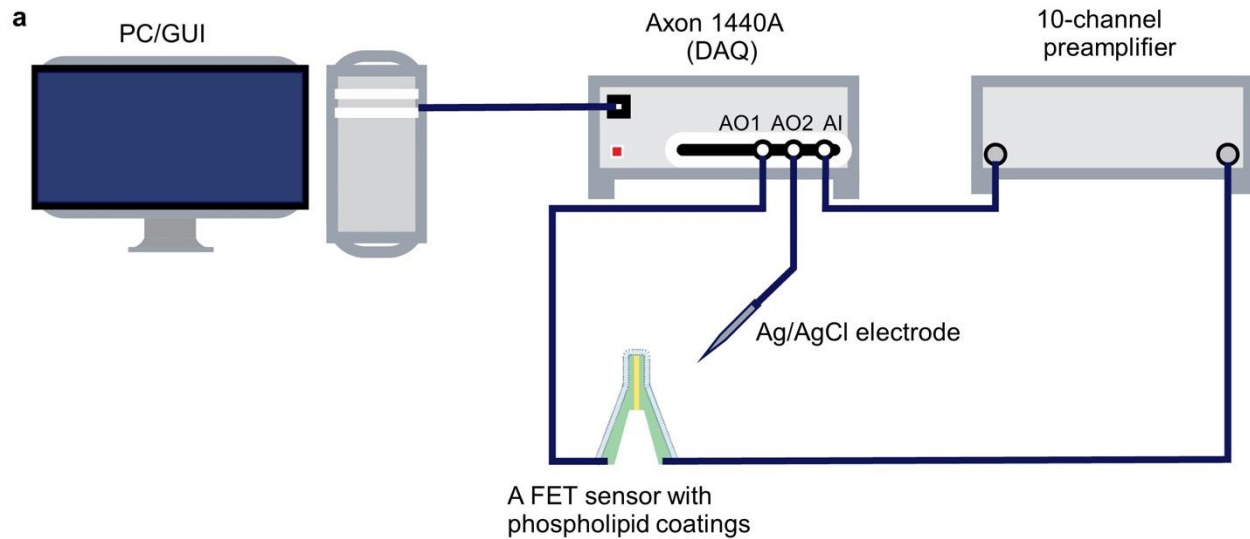
Supplementary Fig. 4 | Experimental setup for recording cellular electrophysiology by the arrayed FETs. a, The setup includes a computer with an installed commercial program (Axon pCLAMP 10 Software Suite), which is used to control the other electronic equipment to acquire the analog signals and to display the converted digital data. The computer is connected with a DAQ that can convert digital to analog or analog to digital signals. One analog output (AO1) channel is connected to the source terminal of all arrayed FETs that share the same potential. Another analog output (AO2) channel is connected to the Ag/AgCl electrode. While performing the water-gate characterization, a potential sweep was applied on the Ag/AgCl electrode. In the cellular signal measurements, a zero potential was applied to that electrode to provide a reference potential of the extracellular medium. The DAQ has a total of 16 analog input (AI) channels. Each channel is connected to one output channel of the preamplifier. The preamplifier's inputs are connected to the drain terminals of the arrayed FETs. **b**, A schematic showing the experiment setup during the water-gate characterization of the FETs. On the Ag/AgCl electrode, a potential is swept from -100 mV to 100 mV. The solution used in this experiment is either PBS or Tyrode's solution. **c**, A schematic showing the experimental setup during cellular signal recording. A zero-gate potential is applied to the Ag/AgCl electrode during measurements. The solution is the extracellular medium of the specific cells being measured.
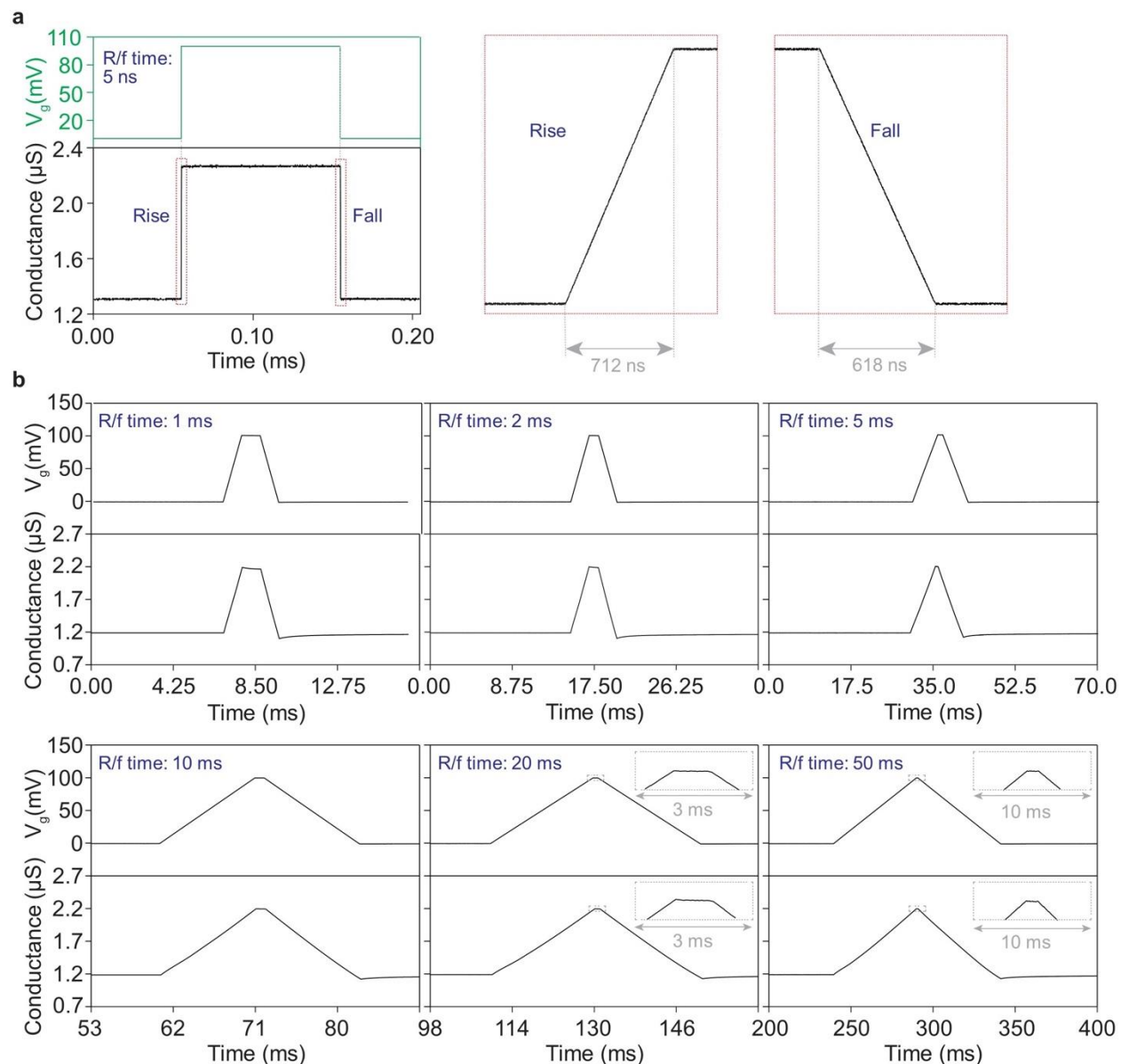
739
740 **Supplementary Fig. 5 | The FET's response characteristics to rapid and slow signals. a**, The
741 FETs respond quickly to the rapid signal applied on its gate (rising/falling (R/f) time 5 ns, duration
742 0.1 ms, amplitude 100 mV, Model 3390, Keithley). The FETs' response time to the rapid signal is
743 hundreds of nanoseconds (Rising: 712 ns; Falling: 618 ns), recorded at a 2 GHz sampling rate
744 (PicoScope 6000) and analyzed in MATLAB. **b**, A 100 mV pulse (rising/falling time ranging from
745 1 ms to 50 ms, duration 1 ms) is applied on the gate by an Ag/AgCl electrode. The corresponding
746 conductance of the FET remains the same trends to the input signals, which manifests its fast and
747 stable response to various signals. The ionic solution-FET gate coupling is influenced by the ionic
748 solution-metal electrode coupling in the water-gate measurement. The induced capacitance
749 responds differently to various AC (fast and slow) inputs and slightly changes the FET's
750 conductance. The induced capacitance can be safely ignored in cellular measurements due to the
751 very localized membrane potentials to the FET gate. These results demonstrate the FET's fast
752 response and large bandwidth for cellular measurements.
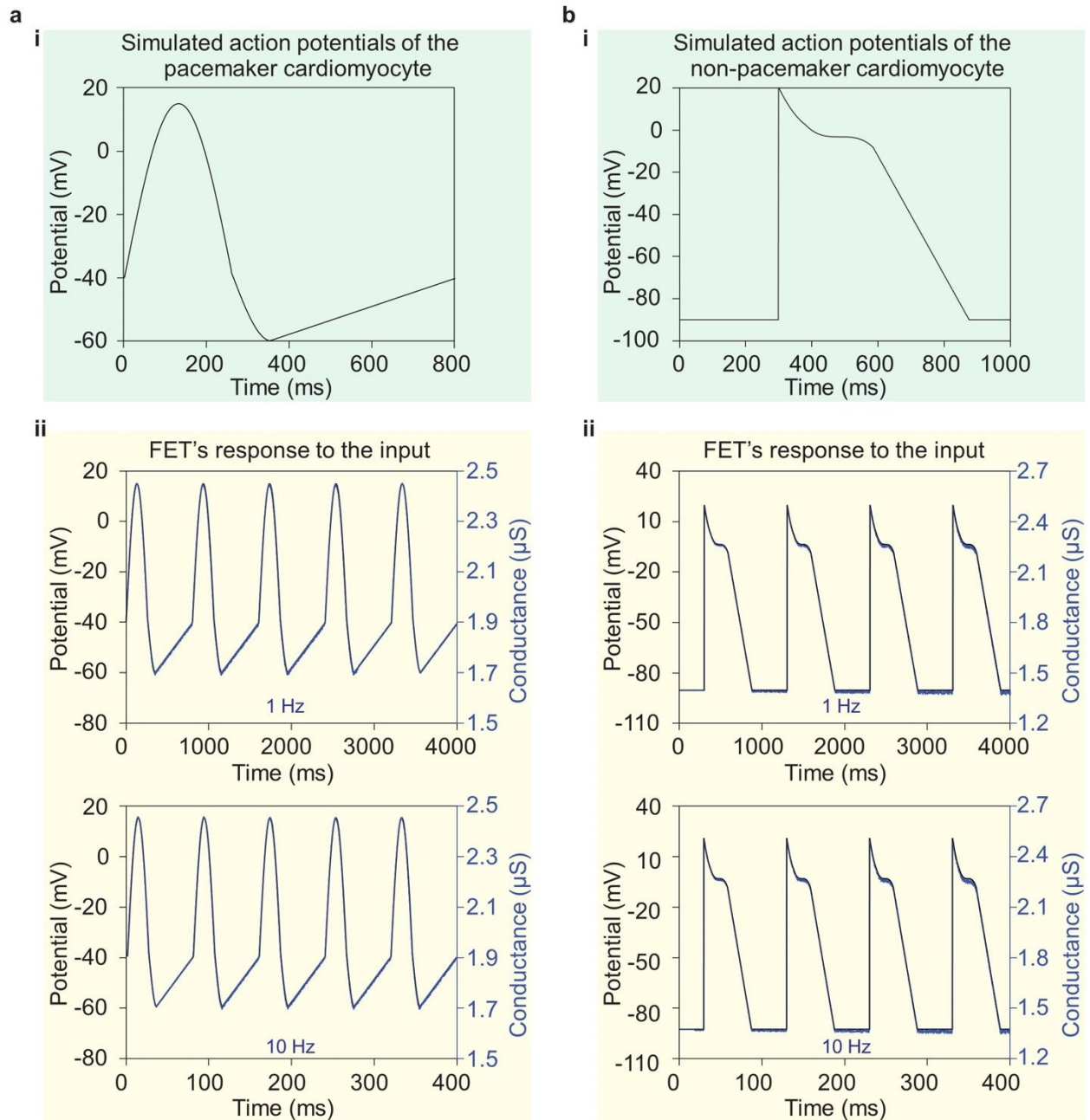
Supplementary Fig. 6 | The FET's response to simulated cellular action potentials. a,b, Simulated action potentials for (**a**) pacemaker and (**b**) non-pacemaker cardiomyocyte. Using the water-gate characterization setup and applying the simulated signals on the FET's gate at 1 Hz, and 10 Hz, corresponding to the action potential frequencies of various mammals' cardiomyocytes. Corresponding signals recorded by an FET are plotted in the same figures, with high fidelity to the original signals' morphologies at these frequencies.

a Mix phospholipids and a fluorescent dye in chloroform in a glass vial

b Desiccate the chloroform solution in N$_2$ gas

c Re-hydrate the mixture in DI water and transfer to a plastic vial

d Phospholipid mixture in a plastic vial

Liquid nitrogen   Water bath

Freeze (in liquid nitrogen) and thaw (in 37 °C water bath) the phospholipid mixture in sequence for 5 times

e Sonicate the mixture solution in a sonicator for 30 minutes

f Filter the mixture solution by extrusion via a 220 nm PTFE syringe filter

g Apply the filtered solution on the device and incubate the device at 37 °C for 2 hours

Supplementary Fig. 7 | The schematic process of functionalizing the FET surface with phospholipids. To prepare the lipid solution, the phospholipids as received are dissolved in the chloroform solution. The chloroform needs to be removed entirely before the lipids get re-hydrated in DI water. The mixture in the aqueous solution then undergoes a freeze-and-thaw process for at least five times to break the multi-lamellar into unilamellar lipid vesicles. Later, sonication disperses the lipid vesicles in the solution and eliminates any aggregates of small lipid vesicles. The final step is to extrude the mixture solution through a PTFE syringe filter. Only the small unilamellar vesicles would be left in the solution. Then the lipid solution is applied on the FETs, which are put in an incubator at 37 °C for at least two hours. After that, removing excessive lipid solutions gently by DI water completes the functionalization. Note that the above processes only work for synthetic phospholipids. For natural cell membranes, they are naturally in a bilayer structure and vesicles. Therefore, only the extrusion step (**f**) is needed to produce small unilamellar vesicles.
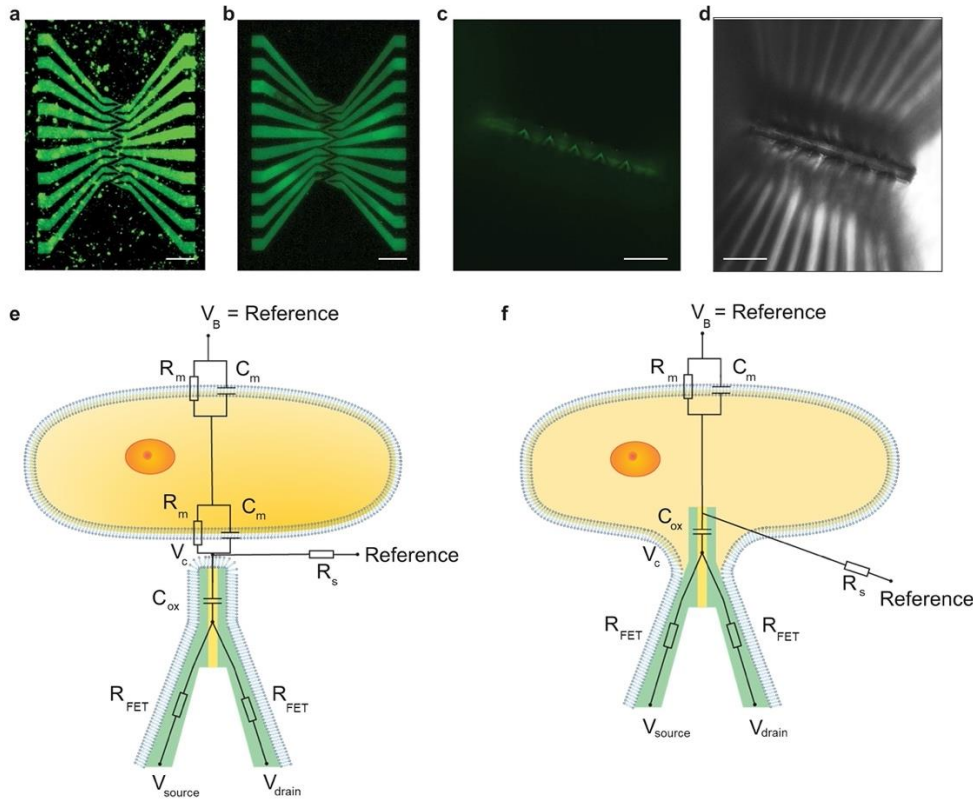
774
775 **Supplementary Fig. 8 | Functionalization of the FET surface with phospholipids and**
776 **equivalent circuit models of cellular measurements before and after FET internalization. a,b,**
777 Fluorescent images showing coatings of (**a**) natural phospholipids of red blood cell membranes
778 and (**b**) synthetic phospholipid (DMPC) on the gate oxide of the FETs. These coatings promote
779 the FETs' internalization into the cell body by spontaneous fusion of the phospholipids and the
780 cell membrane. Scale bars: 100 μm. **c,d,** (**c**) A fluorescent image and (**d**) the corresponding
781 transmitted optical image showing successful phospholipid coating on the 3D FETs. All FETs are
782 coated by the phospholipids as shown by the intense fluorescence of the FET tips. Scale bars: 50
783 μm. **e,f,** Equivalent circuit models of a functionalized FET-cell interface for (**e**) extracellular and
784 (**f**) intracellular interrogations of a cardiomyocyte. Before the phospholipids fuse, the FET sensor
785 is extracellularly recording the membrane potential. The circuit is composed of the FET resistance
786 (R_{FET}), the FET gate oxide capacitance (C_{ox}), the spreading resistance due to the cleft between the
787 cellular membrane and the FET surface (R_s), the cellular membrane capacitance (C_m), the cellular
788 membrane resistance (R_m), the potential applied at the source terminal of the FET (V_{source}), the
789 potential at the drain terminal (V_{drain}), the potential at the extracellular medium (V_B), and the
790 potential in the middle of the conduction channel of the FET (V_c). V_c doesn't represent the recorded
791 potential of the cellular membrane. For an FET, the real cellular potential needs to be converted
792 from the recorded conduction channel current and the transconductance of the FET calculated in
793 the water-gate measurements. With closer proximity to the cell, the cell membrane spontaneously
794 fuses with the phospholipid coating on the FET, realizing biological entrance of the FET and
795 intracellular sensing of the transmembrane potential. These models were built based on widely
796 adopted electrical models of cell membranes and FET[12,32]. The extracellular signals are attenuated
797 and distorted by the membrane impedance, showing a distinct shape to the intracellular signals.
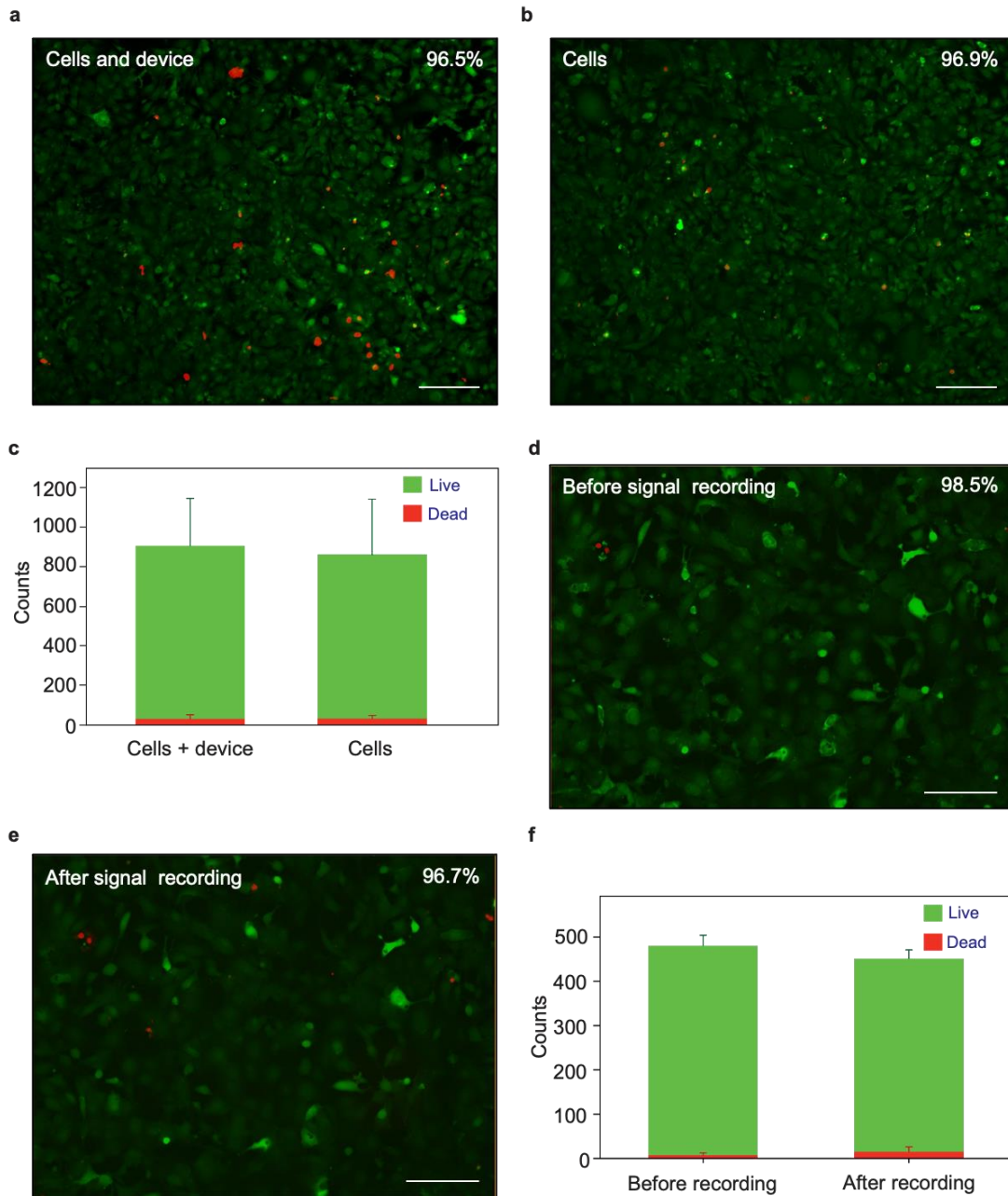
798
Supplementary Fig. 9 | Tests of cell viability. a,b, Confluent HL-1 cells (**a**) with and (**b**) without
an FET device in the culture for two days. Fluorescent imaging results of live (green)/dead (red)
cells show ~97% viability in these confluent cell cultures. **c**, Statistics of 8 cell cultures show that
the FET has no cytotoxicity to the cells. **d,e,** Fluorescent imaging results of the same region of a
confluent HL-1 cell culture (**d**) before and (**e**) after signal recording with 98.5% and 96.7% of cells
alive, respectively. The FET shows little harm to the cells. **f,** Statistics of 3 cell cultures show that
the recording process have negligible cytotoxicity to the cells. All scale bars: 200 μm.

a   Aspirate the cell culture medium and replace it with Tyrode's solution

Cells in the culture medium (pink)   Cells in the Tyrode's solution (clear)

b   Add Fluo-4 AM stock solution and incubate at 37 °C for one hour

c   Aspirate the old and add fresh Tyrode's solution before observing the result under a microscope
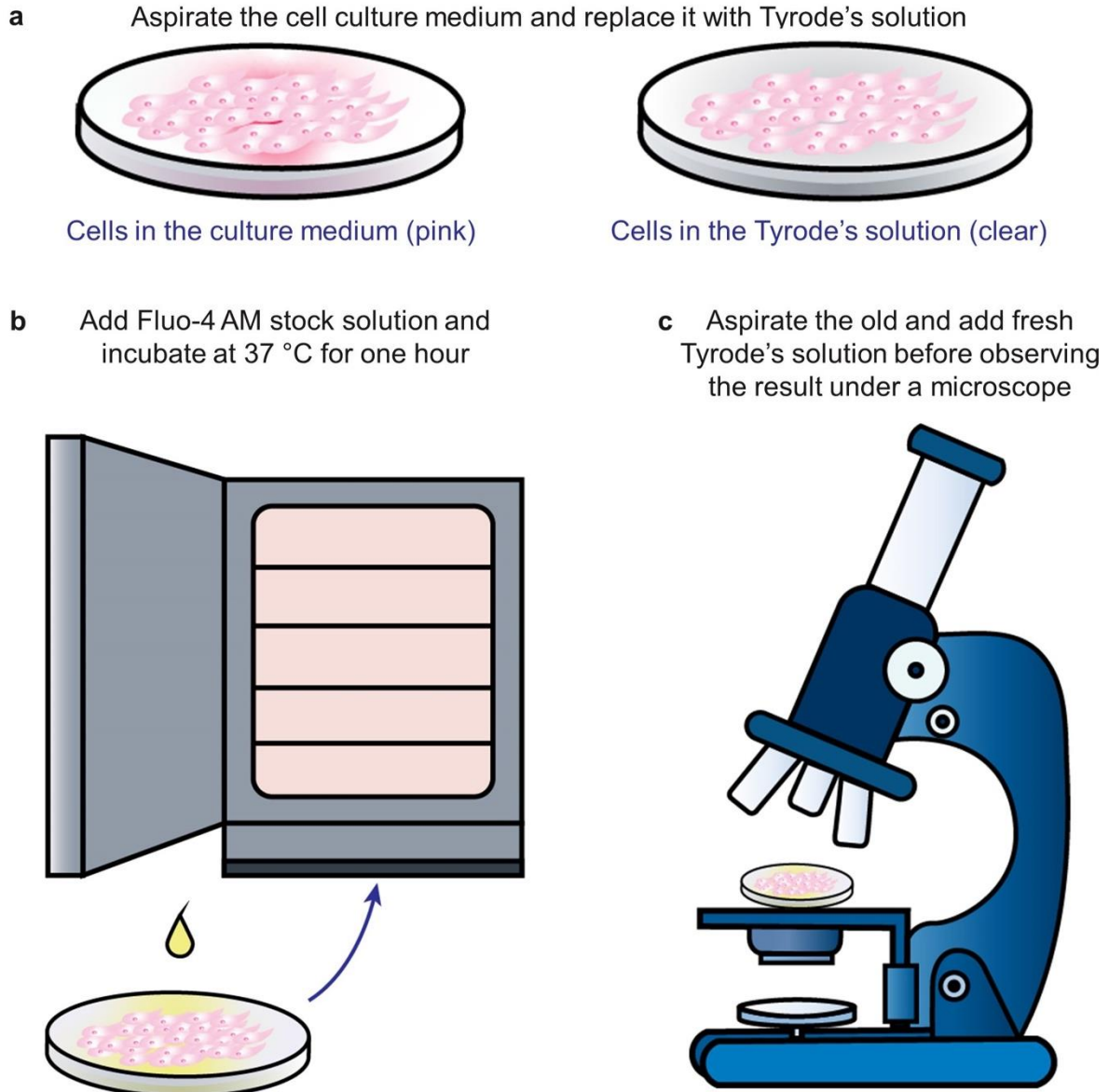
Supplementary Fig. 10 | The schematic process of Ca^{2+} sparks screening assay. a, HL-1 cells are cultured in a petridish filled with the supplemented Claycomb medium. The medium is removed by aspiration and Tyrode's solution is added with Ca^{2+} and glucose (pH: 7.35 at 37 °C). **b**, The Fluo-4 AM stock solution is added in the cells that are incubated for one hour. After that, the old solution is aspirated, and the fresh Tyrode's solution is added. **c**, Fluorescent Ca^{2+} sparks can be immediately observed under a microscope.
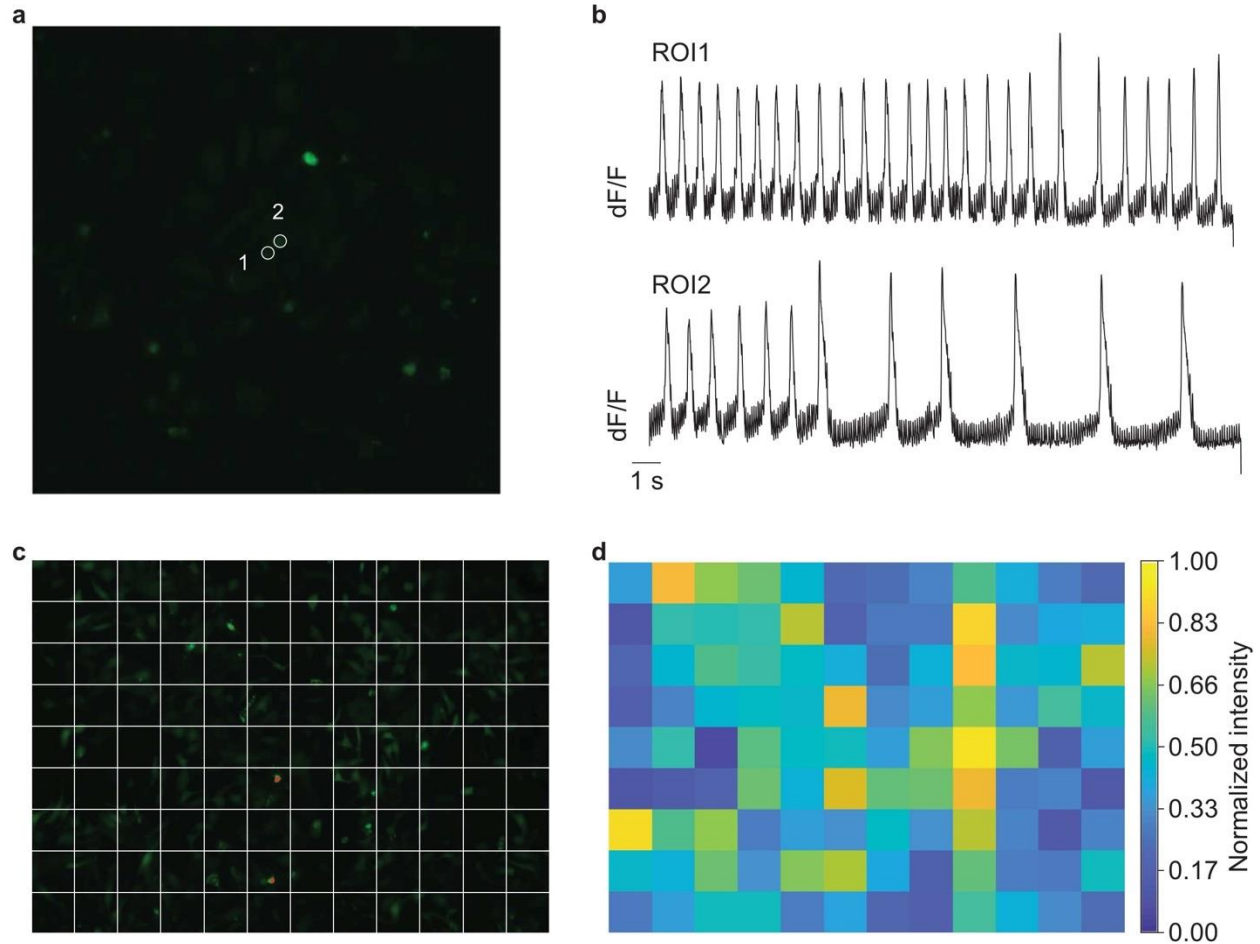
Supplementary Fig. 11 | Ca^{2+} sparks assay illustrating HL-1 cells' action potentials and mapping field potentials in the whole cell culture. a, A single snapshot from a video of an HL-1 cell culture stained with the Fluo-4 AM fluorescent dye. Two circles outline the two regions of interest (ROIs) to be analyzed, as marked by 1 and 2. **b**, Quantitative fluorescent intensity analysis of the ROI1 and ROI2 showing the transient Ca^{2+} signals. Quantifications are performed on stacked snapshots extracted from the video, which would clearly illustrate the spiking rate and the signal conduction pathways in the whole 2D cell culture. Calculating the fluorescent intensities of ROI1 and ROI2 of every snapshot provides the digitized fluorescent intensity to render the plot. **c**, Mapping the fluorescent intensities of the whole observation region reveals the positions that are showing the Ca^{2+} sparks at the corresponding time to that image. Quantification and replotting the fluorescent intensity amplify the intensity contrast for displaying the Ca^{2+} distribution. Each snapshot is sectioned into 12 by 9 ROIs, and each ROI's average fluorescent intensity is digitized. **d**, A heatmap showing the quantified intensity results of the image in (**c**). The Ca^{2+} sparks appear in those yellow regions.
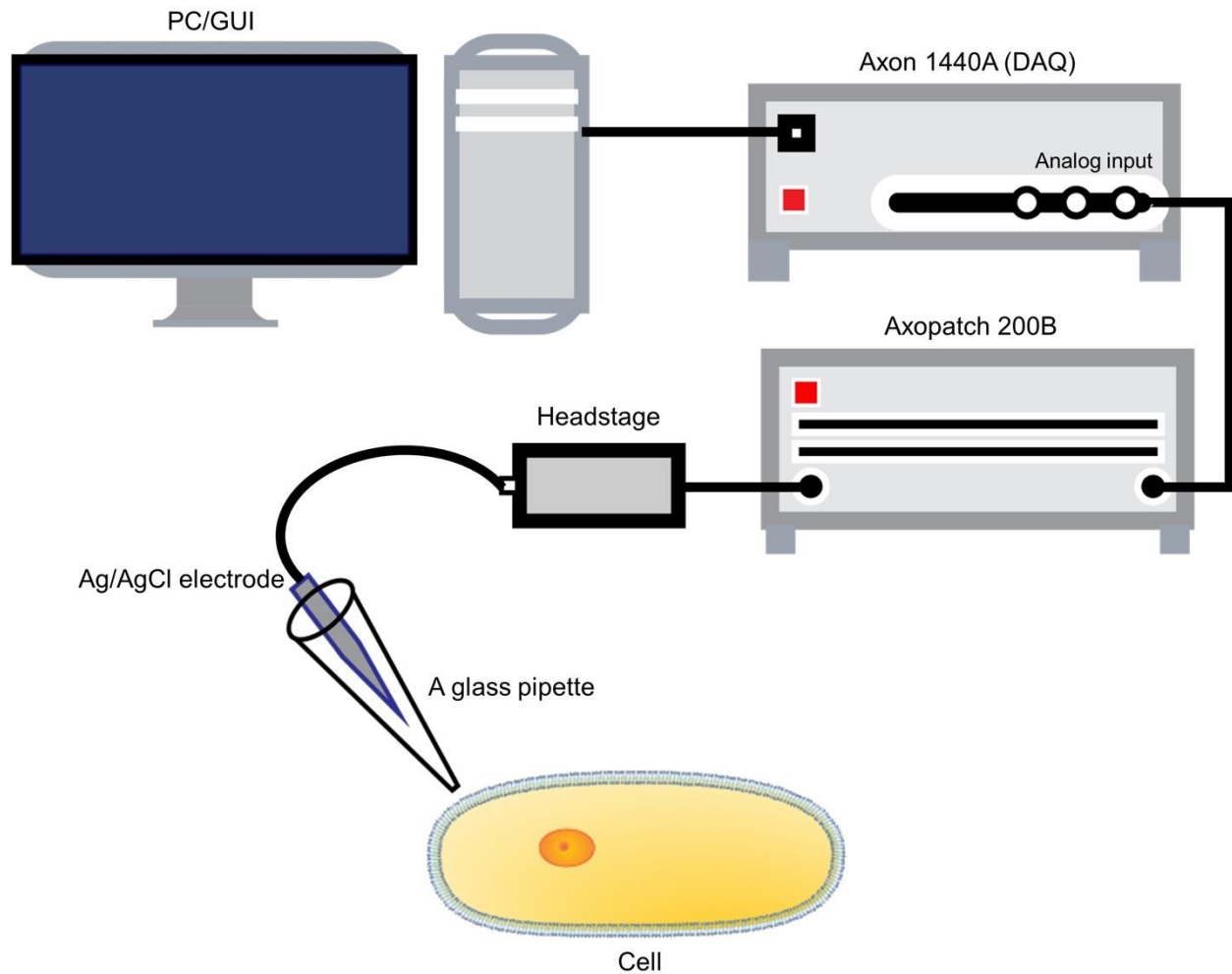
828
829 **Supplementary Fig. 12 | The schematic experimental setup of using the patch clamp to record**
830 **intracellular signals of a single cell.** The setup includes a computer that installs a commercial
831 program (Axon pCLAMP 10 Software Suite), which is used to acquire, convert, and display the
832 analog signals from the cells. The computer is connected with a DAQ that can realize digital to
833 analog or analog to digital signals conversion. One of the DAQ's analog input channels is
834 connected to a commercial preamplifier (Axopatch 200B). The preamplifier's input is linked to a
835 headstage that can eliminate the system noise and stabilize the recorded signals from an Ag/AgCl
836 electrode. The Ag/AgCl electrode is housed in a glass pipette of as small as a 1 μm in tip size. The
837 pipette is filled with saline solution. The small pipette tip can clamp to a small patch of the cellular
838 membrane. The whole-cell patch is performed when the cellular membrane at the patch gets
839 ruptured and a giga-seal is formed between the pipette and cellular membrane.

840
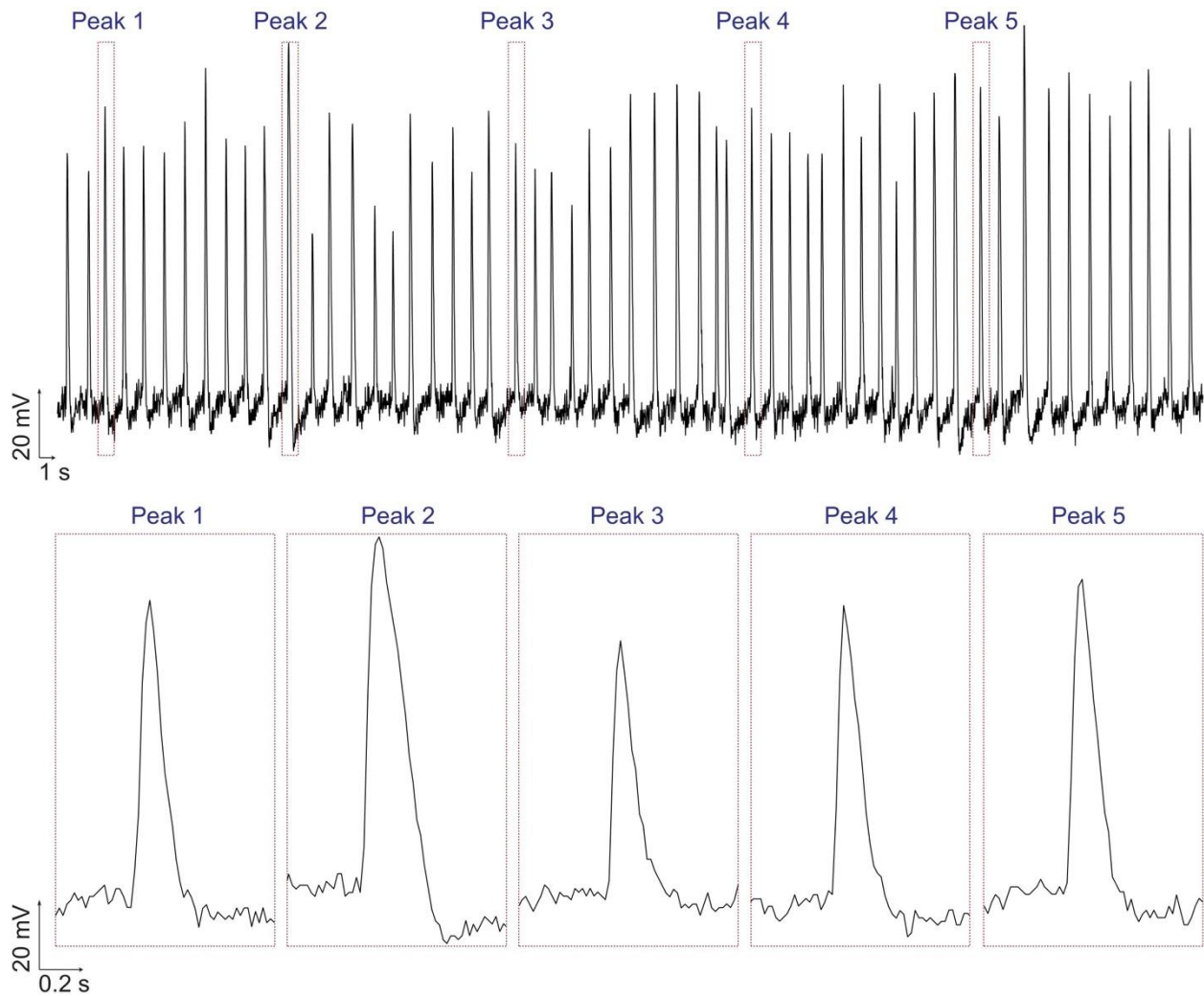
841
842 **Supplementary Fig. 13 | Extended intracellular recordings of an HL-1 cell.** Intracellular
843 recordings of an HL-1 cell can maintain stable with periodic spikes for 71 seconds. The cells'
844 activities are influenced by temperature, solution pH, and/or ion concentration disturbance during
845 the measurement, which typically limit the possibility of long-time monitoring. What we
846 demonstrate here is a considerably long duration among all reported active FETs for intracellular
847 recordings[33,34].

a

Transconductance (μS·V⁻¹)

Before insertion · After insertion 1 · After insertion 2 · After insertion 3 · After insertion 4

b

First insertion into cell 1

Second insertion into cell 2

Third insertion into cell 3

Fourth insertion into cell 4

Fifth insertion into cell 4 after FET re-functionalization

50 mV

1 s
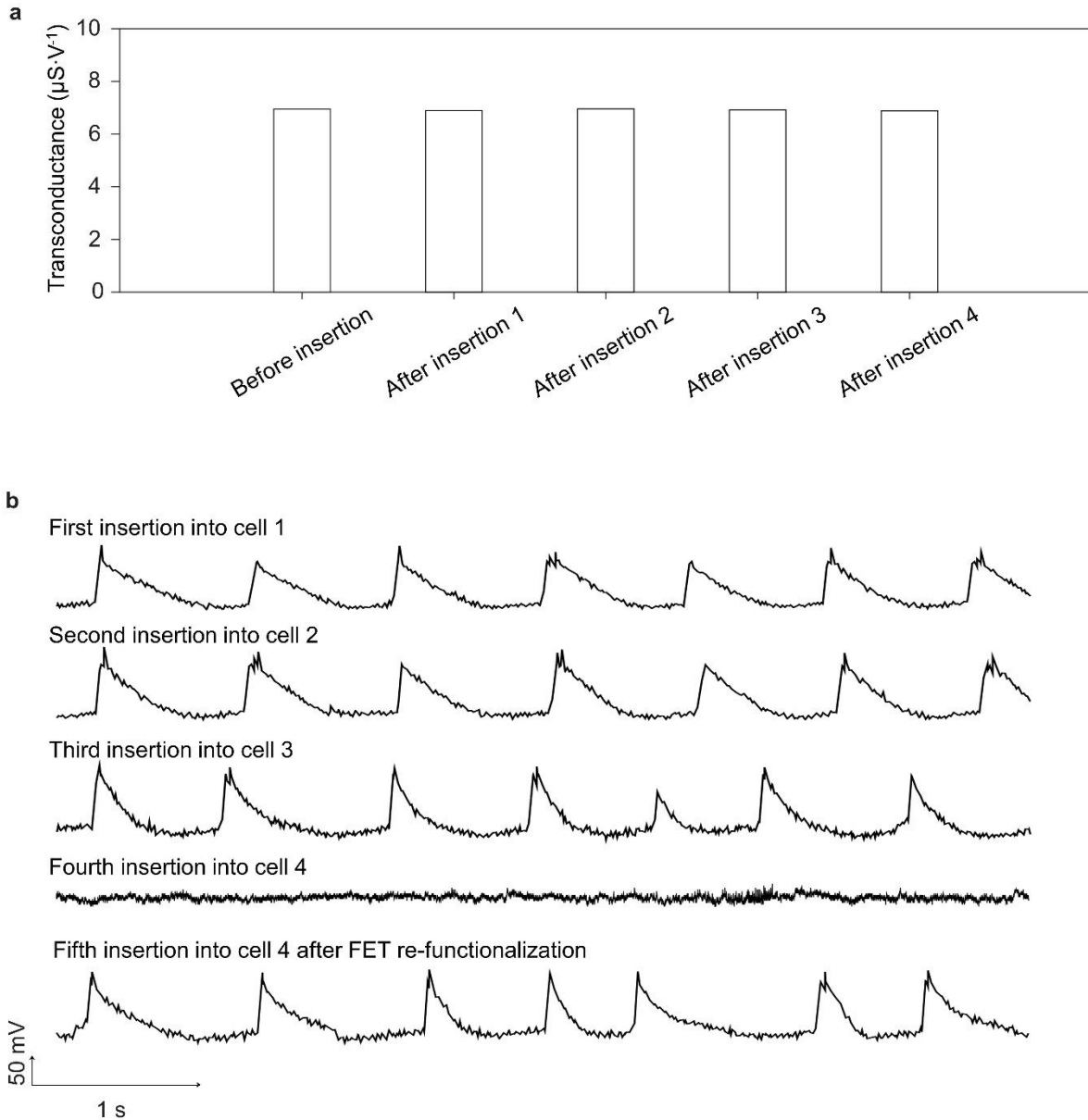
Supplementary Fig. 14 | Durability test of functionalized FETs for intracellular recording. a, The FET's transconductance was measured before the first and after each cell insertion, showing its stability. **b,** Intracellular recordings of four different cells show that cell insertion becomes unsuccessful after three cell insertions. After re-functionalization of the same FET, intracellular action potentials were obtained from the fourth cell, which revealed that the failed intracellular recording in the fourth insertion was because of the damaged lipid bilayer on the FET surface.

a

b
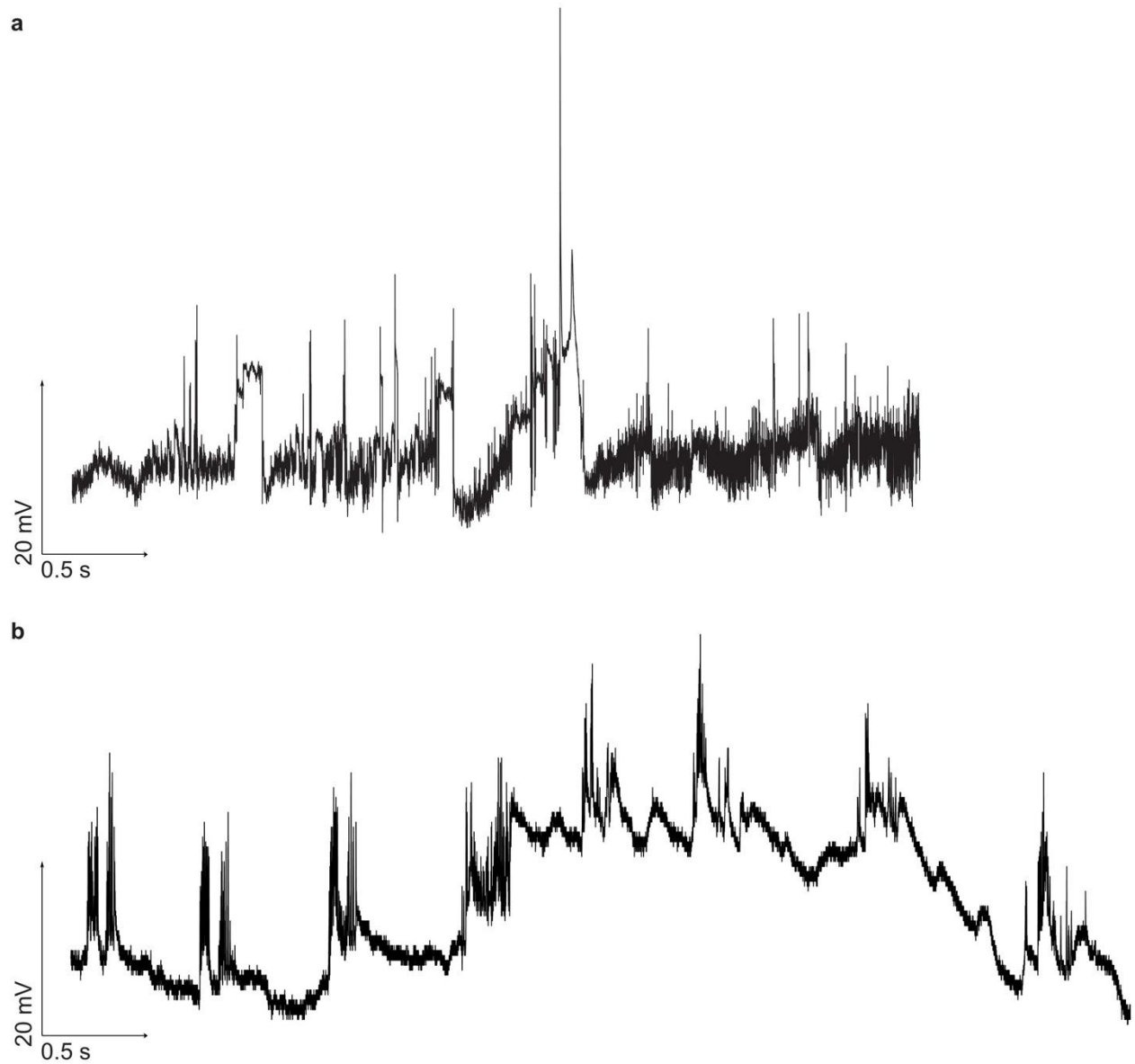
855
856 **Supplementary Fig. 15 | Recorded action potentials of adult mouse cardiomyocytes without**
857 **phospholipids coatings. a,b,** Two sweeps of intracellular signal recordings on adult mouse
858 cardiomyocytes without lipid functionalization on the FET surface, with (**a**) considerable noise or
859 (**b**) fluctuating baselines during the recordings due to the unstable FET-cell membrane interfaces.
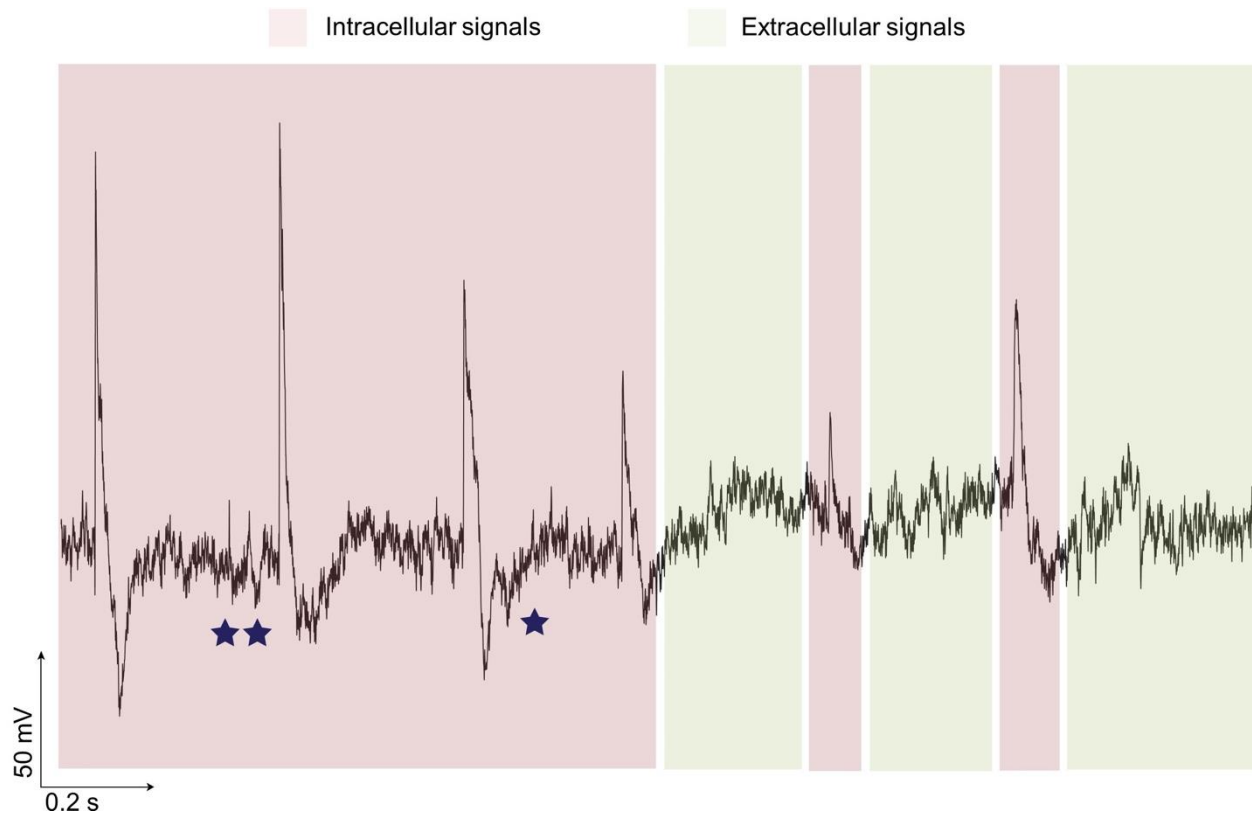
Supplementary Fig. 16 | The process of transitioning from intracellular to extracellular recordings. In this case, the intracellular recording of the HL-1 cell is achieved by mechanically rupturing the cell membrane. However, the sensor-cell interface is unstable. The cellular membrane will gradually fuse again and expel the FET. Thus, the signals sometimes show a transitioning process from intracellular (red shaded areas) to extracellular (light green shaded areas) recordings. Intracellular subthreshold events are recorded as marked by the stars. These low-amplitude signals cannot stimulate the all-or-none action potentials but can reflect the membrane potential oscillations due to ionic activities across the cellular membrane. For instance, these subthreshold potentials can influence sodium ion channels (i.e., the h gate) to open or close, generating a refractory period when the action potentials cannot be triggered[35].
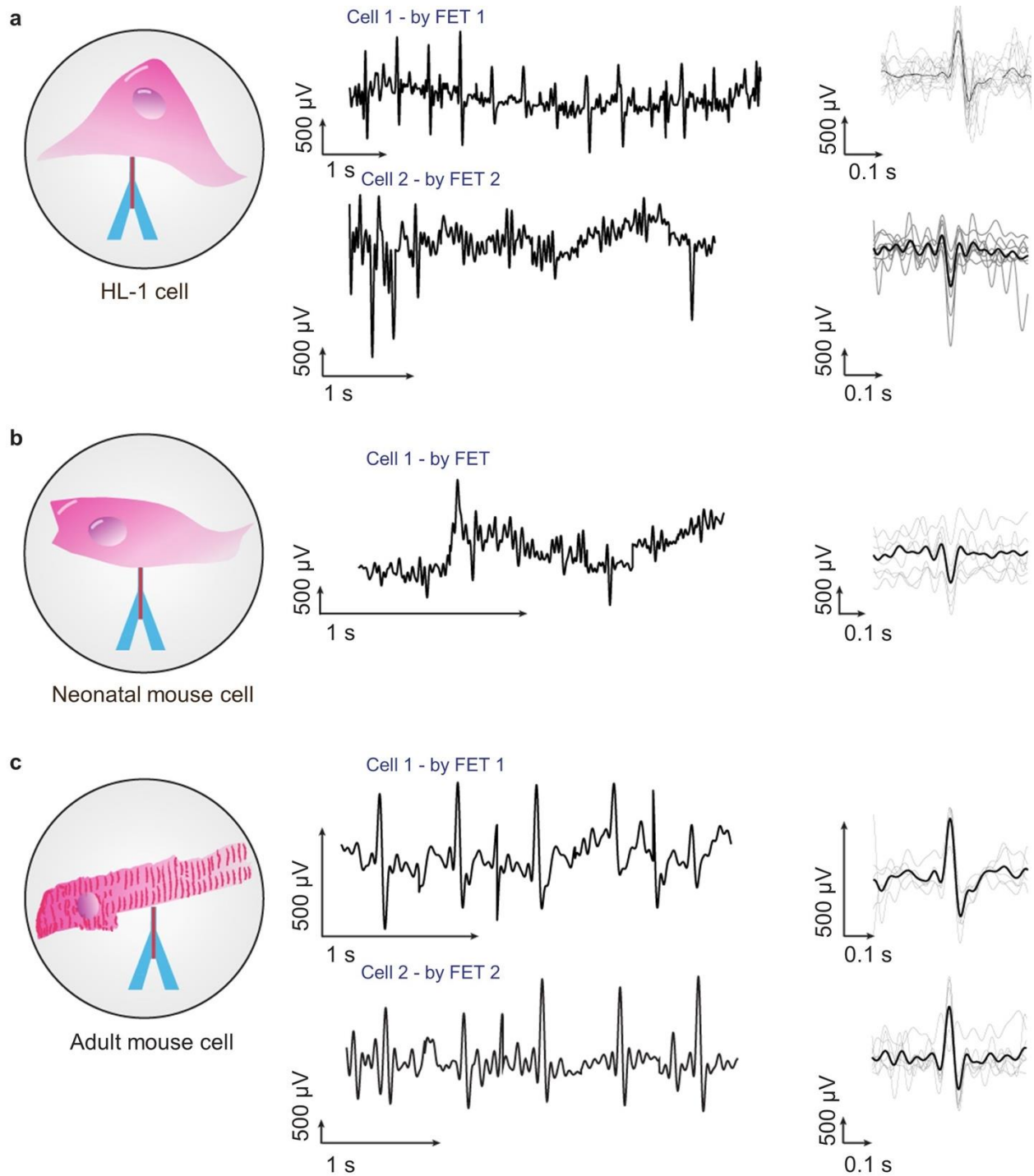
871
Supplementary Fig. 17 | Extracellular field potentials of cardiomyocytes recorded by the FETs. a–c, Before penetrating the cell membranes, with close contact, the FETs can record periodic spikes from (**a**) the HL-1 cells and (**b**, **c**) primary cells. These low-amplitude extracellular signals are characteristic extracellular field potentials of the cardiomyocytes[36,37].
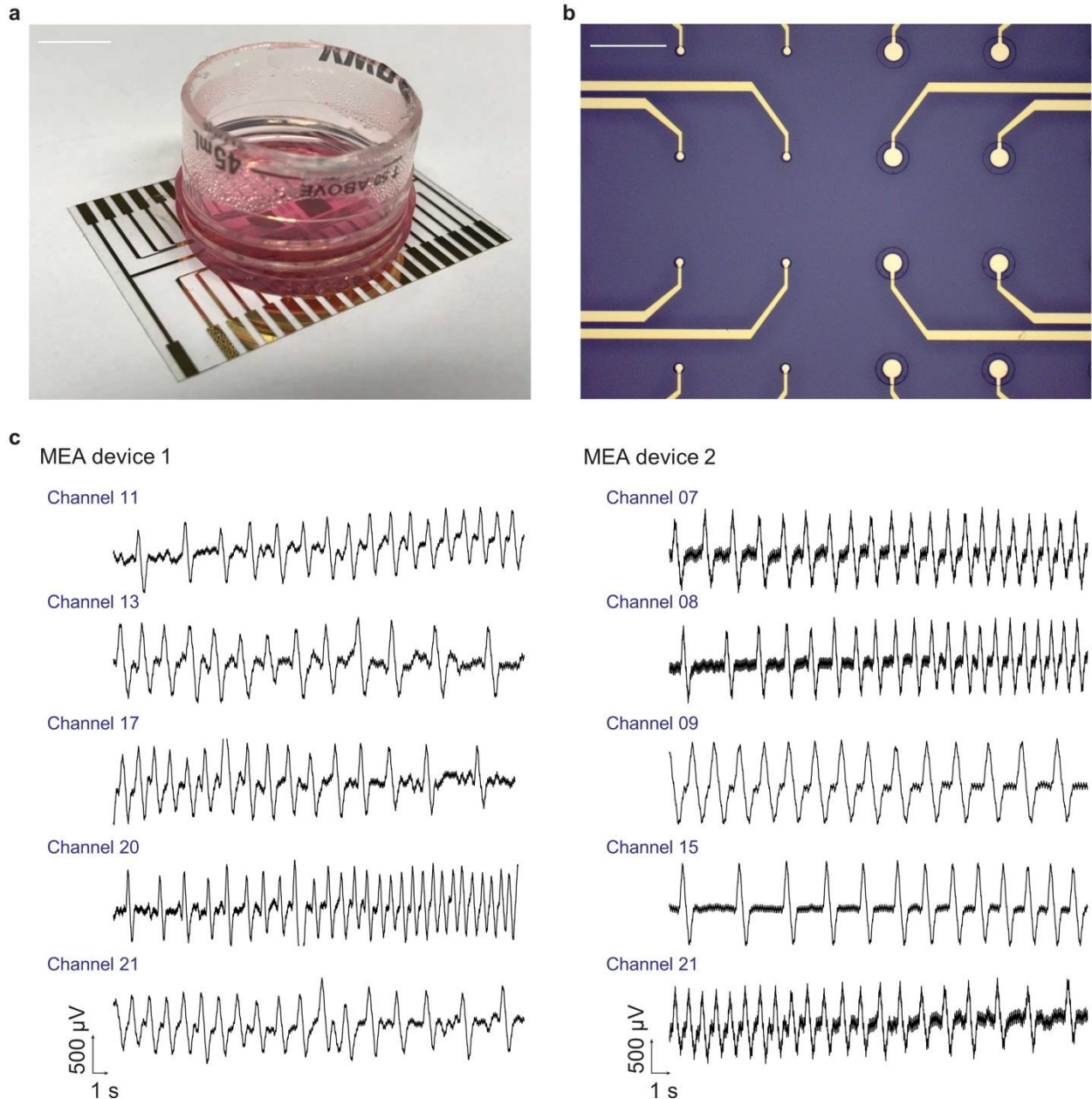
Supplementary Fig. 18 | Extracellular field potentials of HL-1 cells recorded by the MEA. a, A picture of the MEA with a customized container filled with the Claycomb Medium for HL-1 cell growth. Cells are growing on the MEA surface inside the tube for 3–4 days in an incubator at 37 °C, 5% CO_2 before they reach confluency. Scale bar: 10 mm. **b**, A closeup optical microscope image showing the metal pads and the covered connection wires by a layer of insulating SU-8. Only the circular areas of the metal pads are exposed to contact the cells. Scale bar: 200 µm. **c**, Representative extracellular field potentials of the HL-1 cells from two MEAs. The signals have been processed by a bandpass filter (0.5–30 Hz) in MATLAB.
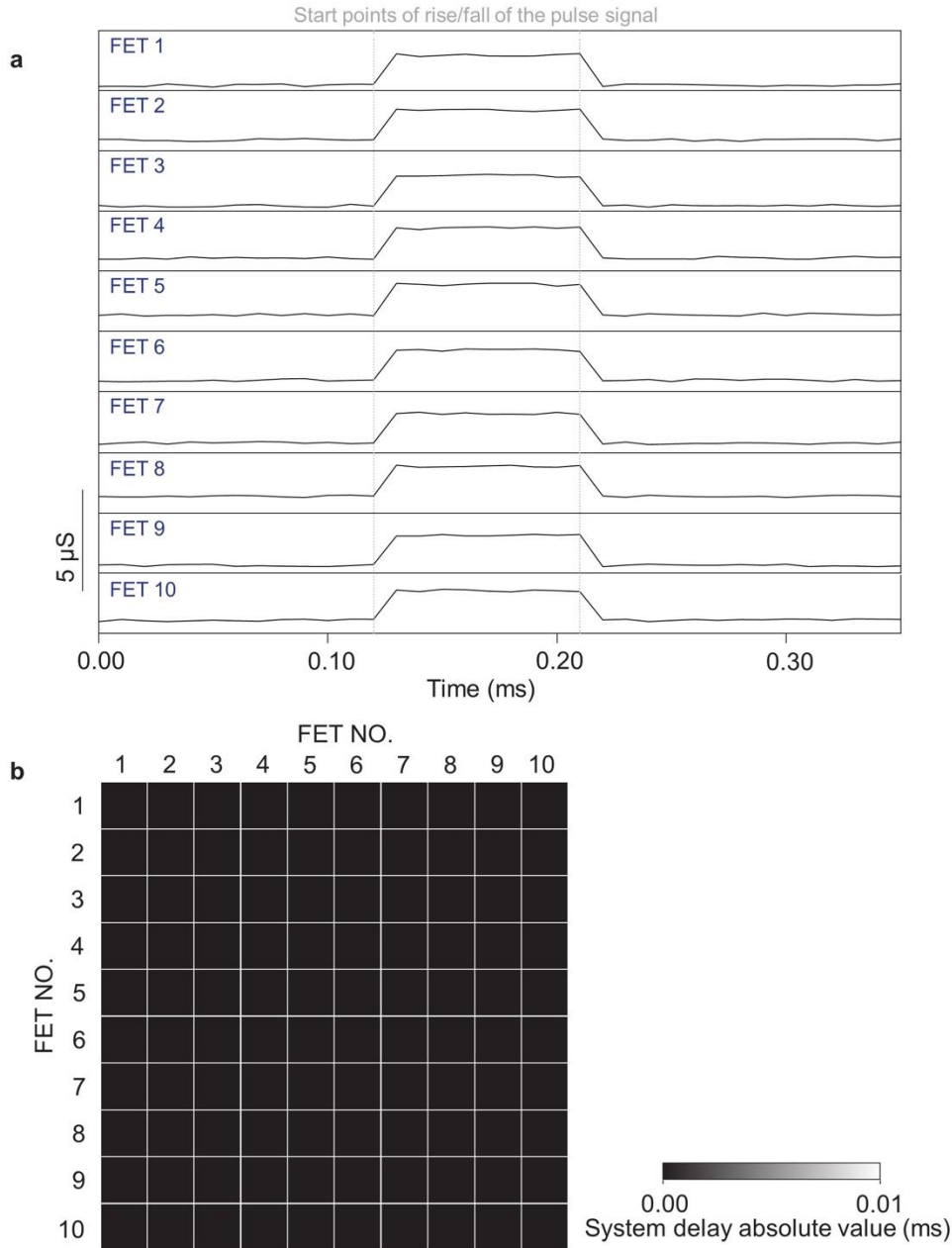
Supplementary Fig. 19 | Characterization of the electrical signal delay introduced by the measurement system. The same method as that used to characterize an FET's temporal response to dynamic signals is adopted to measure the delay between any two FETs in an array. A 100-mV pulse (rising/falling time of 0.01 ms, duration of 0.1 ms) is applied on a 10-FET array. The FETs' responses to the input pulse signal are simultaneously recorded at a 100 kHz sampling rate. **a**, Responses of the 10-FET array to the same input signal showing each FET is working independently. The dash lines mark the starting points of the rise and fall edges of the pulse. **b**, The cross-correlation method is used to calculate the latencies between any two channels showing that the system delay over the whole device is negligible. It proves that multiple FETs in an array exhibit the same characteristics to dynamic signals. Further, the system-induced electrical delay is negligible compared to those generated from cellular ionic dynamics.
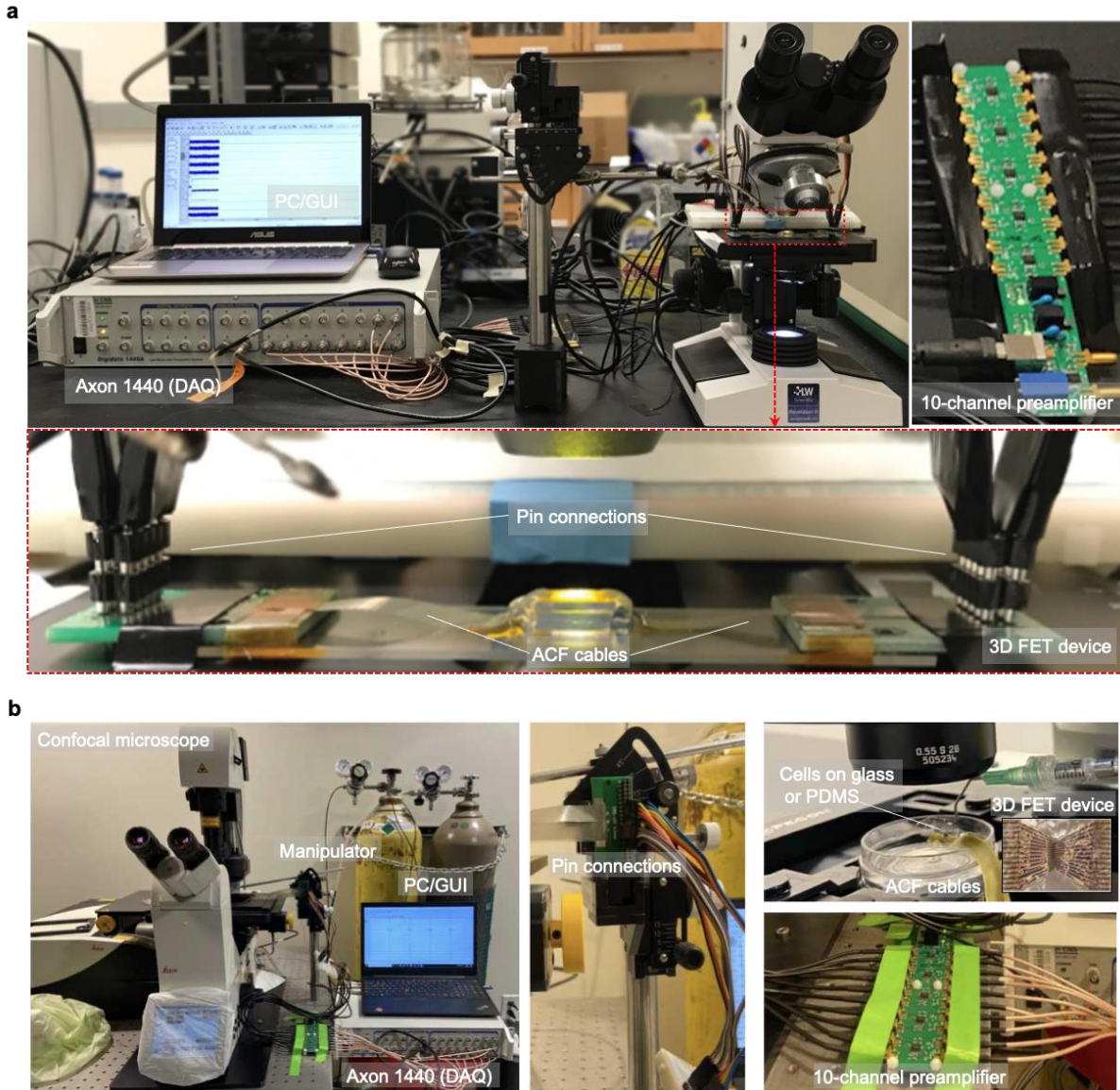
Supplementary Fig. 20 | Pictures of the experimental setup for cellular electrophysiology recording using the arrayed FETs. a,**b**, Using an ACF cable, the FET array is connected to the amplifier, analog-to-digital converter (ADC), and PC sequentially, as shown in the schematics in Supplementary Fig. 4a. During measurements, we can either place a sheet of PDMS (**a**) with cardiomyocytes on the FETs or fix the FET to a manipulator and approach to cell cultures in the dish (**b**). During signal recording, an Ag/AgCl electrode is inserted into the culturing solution to maintain the extracellular potential at zero bias.

906
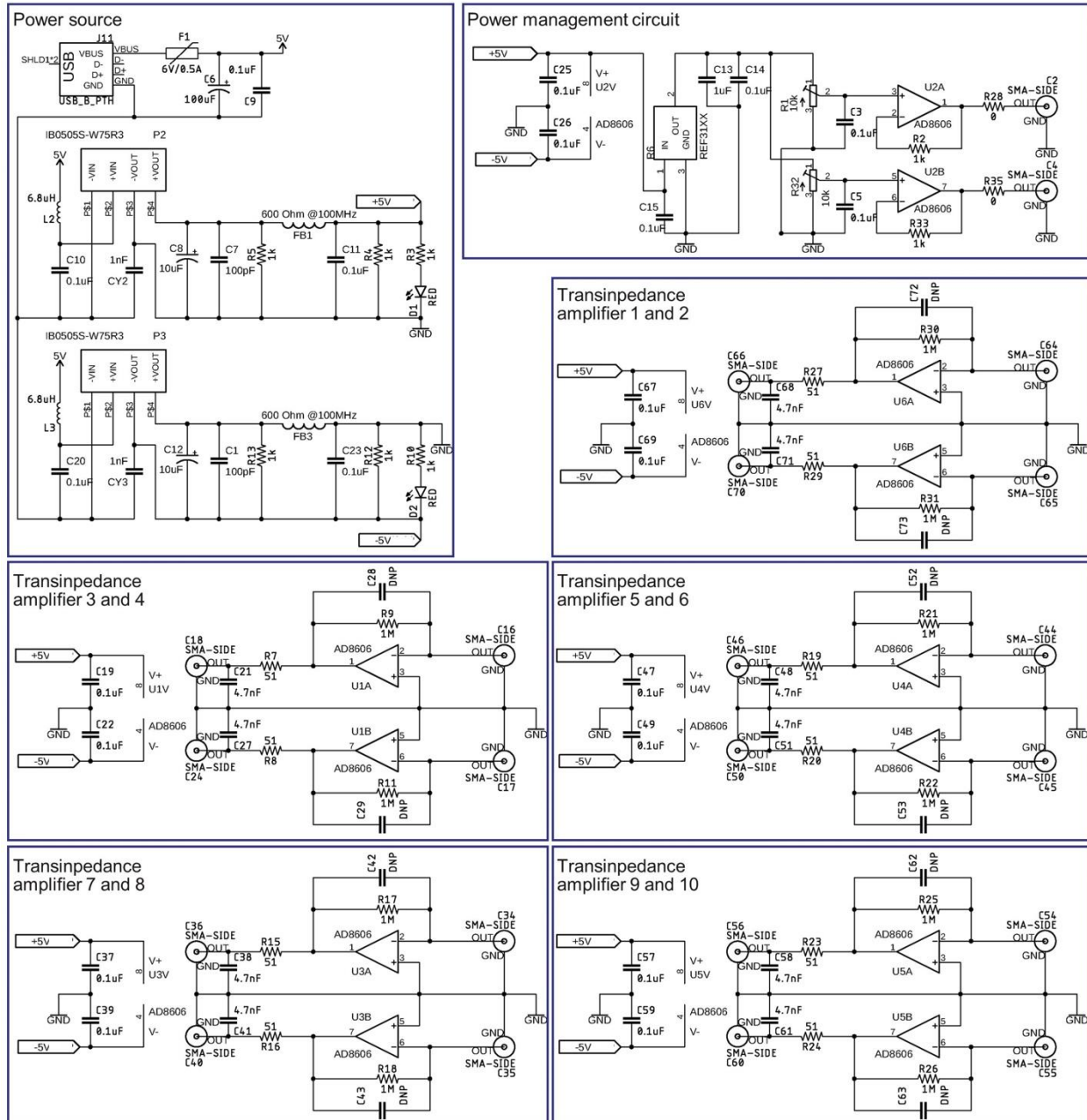
Supplementary Fig. 21 | The circuit design of the customized 10-channel current preamplifier. The current amplifier contains a USB power source and a power regulation circuit that can stably output +5 V and -5 V constant voltages to the entire circuit. A power management circuit is designed to stabilize the output voltage further to be +5 V or -5 V accurately. Also, it can regulate the output voltage to be in the range from 0 to 2 V. The amplifier circuit integrates ten independent transimpedance amplifier circuits that can function individually.
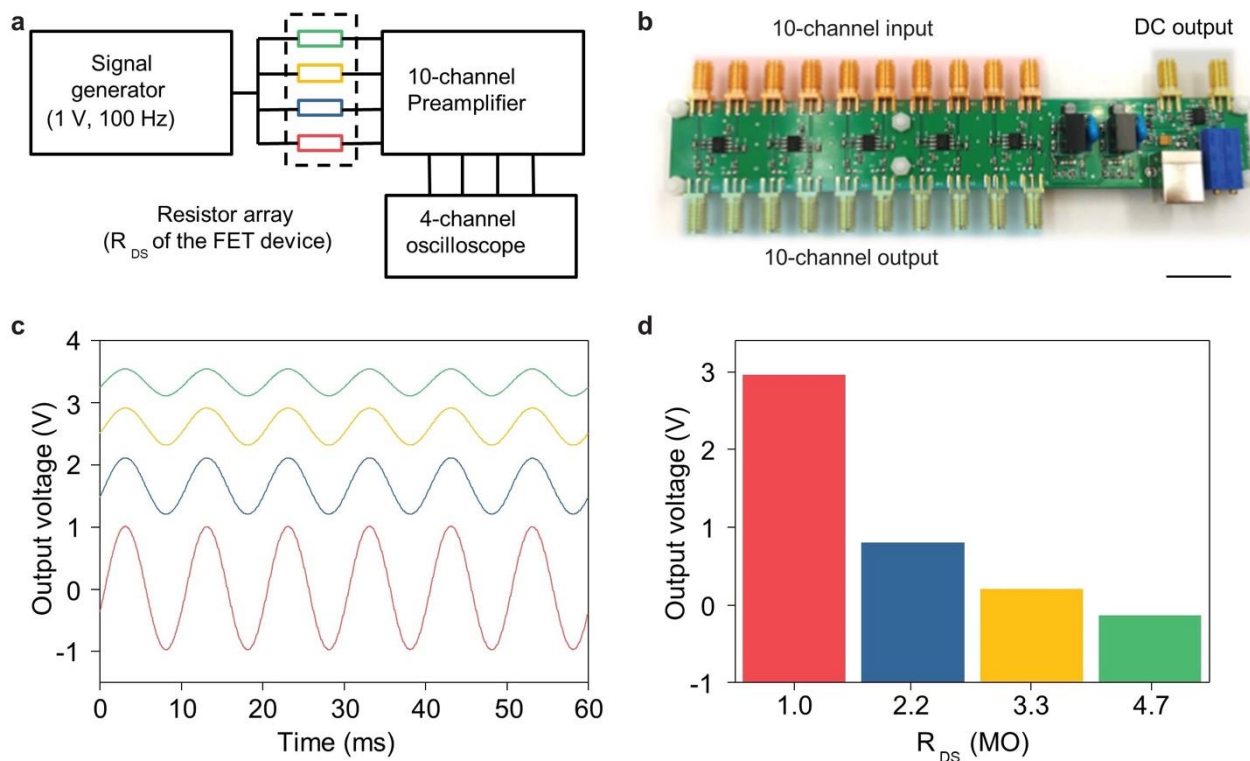
Supplementary Fig. 22 | Electrical properties of the customized 10-channel current preamplifier. a, The electrical setup to characterize the multi-channel amplifier. A generated signal is exerted on four parallelly connected resistors. The other ends are input into four different channels of the preamplifier. An oscilloscope displays the amplified and digitalized signals. **b**, A picture of the customized 10-channel preamplifier, labeled with input and output terminals. Scale bar: 2 cm. **c**, Amplified signals in corresponding colors. The amplitude differences are from the different values of the four resistors. **d**, The amplitude of each output signal is different from each other, which demonstrates the four channels are functioning independently, with no crosstalk.

a

FET 1 ····· 0.82 µS
FET 2 ····· 0.95 µS
FET 3 ····· 0.73 µS
FET 4 ····· 1.02 µS
FET 5 ····· 1.11 µS
FET 6 ····· 0.97 µS
FET 7 ····· 1.31 µS
FET 8 ····· 1.22 µS
FET 9 ····· 0.85 µS
FET 10 ····· 0.91 µS

10 µS

Time (ms)

b

Before short circuit   After short circuit

FET 1   5.12 µS   6.14 µS   ····· 1.21 µS

FET 2   5.97 µS   6.14 µS   ····· 1.05 µS

5 µS

0.1 µs
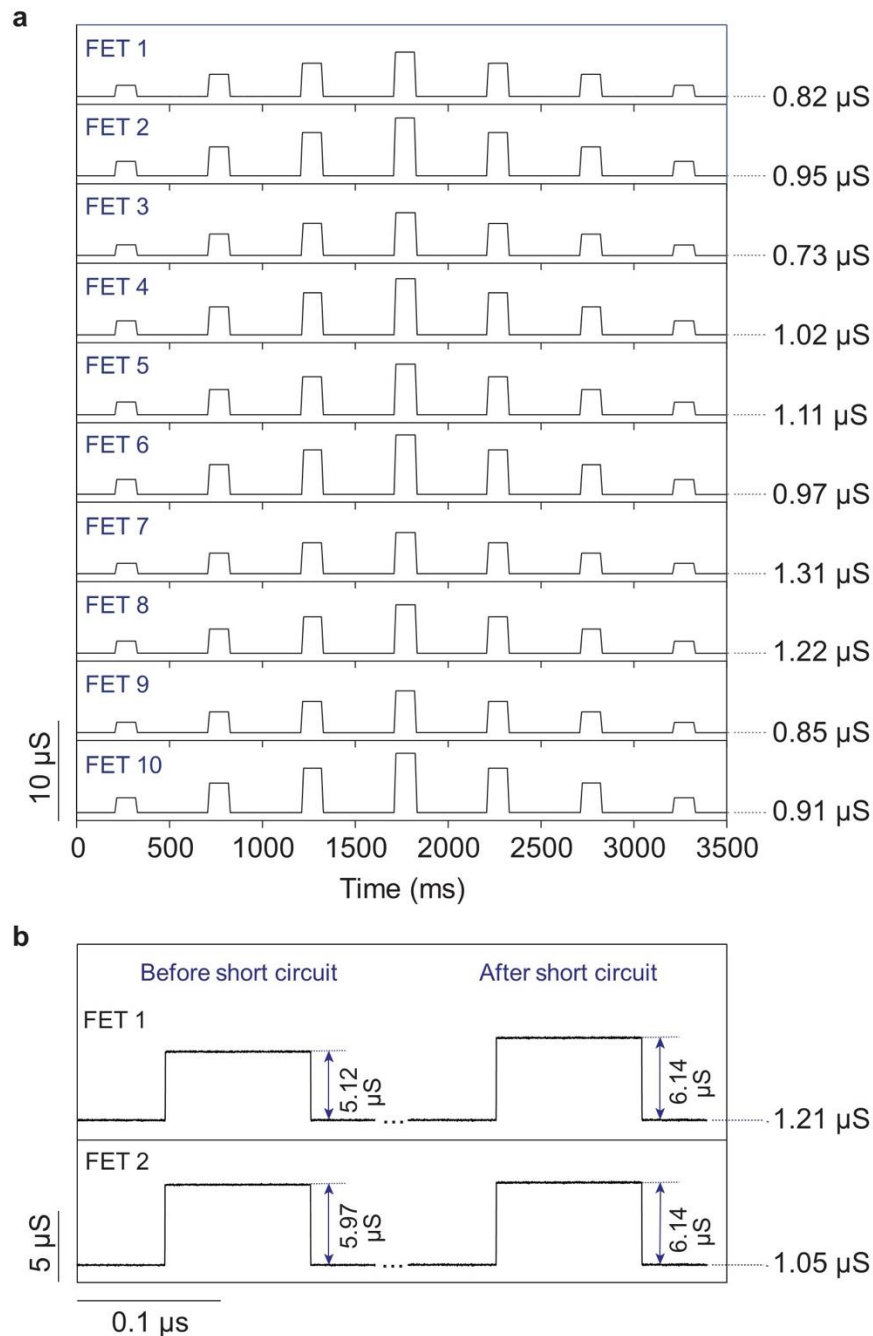
922
923 **Supplementary Fig. 23 | Verifying the arrayed FET device's crosstalk. a,** The same signal,
924 containing seven pulses (from 100 mV to 400 mV and then back to 100 mV, with a step size of
925 100 mV, rising/falling time of 0.1 ms, duration of 100 ms), is applied to the gate solution of all 10
926 FETs. Each FET is separately connected to an individual channel of the preamplifier. The 10
927 responses recorded by the 10 FETs show different signal amplitudes, illustrating the variance of
928 their sensitivities. The conductance of each FET under zero gate potential is shown in the far-right
929 column. Each FET is recording signals independently, with no crosstalk during operation. **b,** When
930 two FETs are shorted, their recordings become identical, which further proves that those small
931 signal latencies are resulted from the cellular activities.

42
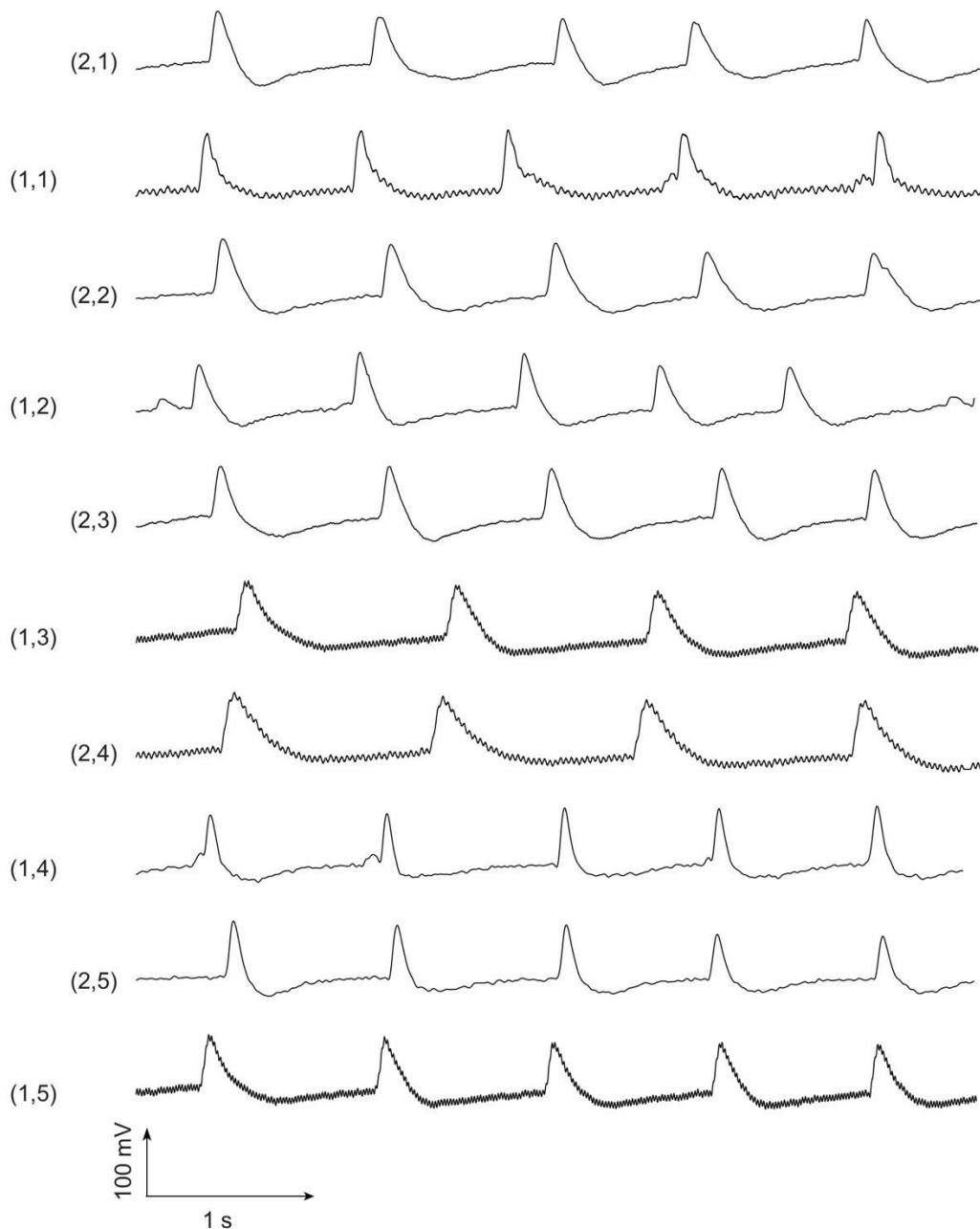
Supplementary Fig. 24 | Recordings of spontaneous firing HL-1 cells by a 10-FET array. Cells communicate on the basis of intercellular electrical coupling by gap junctions, particularly ion channels. Ions (e.g., K^+) can travel from one cell to its neighboring cells via these gap junctions, triggering the donor cells' action potentials. Without pacing the cells (e.g., by a platinum stimulation electrode), the FETs can also form stable FET-cell interfaces and record action potentials from different cells. However, the action potentials show arrhythmic firing patterns, which mean the period of action potentials is varying. Also, the action potential's propagating behaviors become irregular because the locations and firing patterns of those spontaneously firing cells (i.e., pacemaker cells) in the culture are stochastic and inconsistent. Therefore, the signal conduction direction among these cells will alter according to the signals of the pacemaker cells.

a Original data (Extended Data Fig.5a)

(2,1)
(1,1)
(2,2)
(1,2)
(2,3)
(1,3)
(2,4)
(1,4)
(2,5)
(1,5)

1 s

200 mV
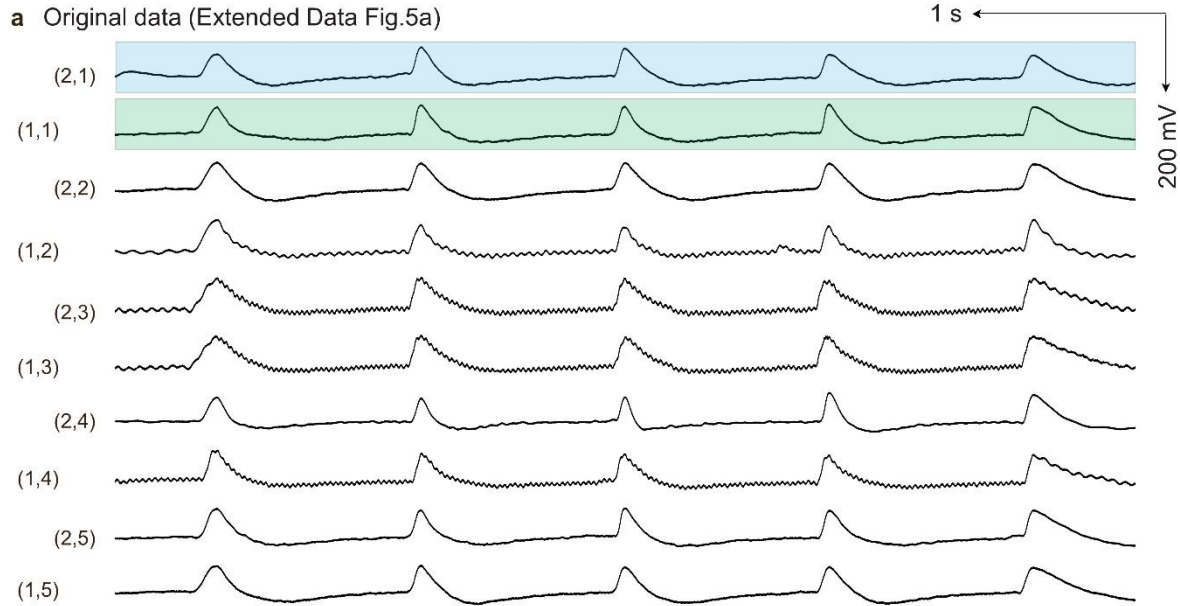
b Selected the data to process (cross-correlation)

i Section the data into 5 windows

Window 1

Window 2

-0.68   -0.66   -0.66   -0.69   -0.70

Δt (ms)
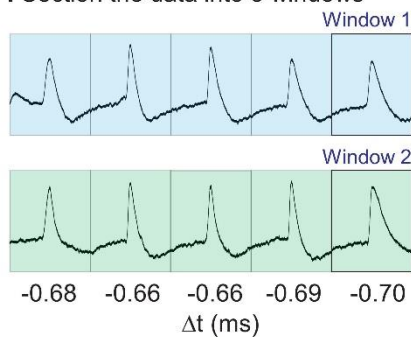
ii Select the windows (1 and 2) to calculate

Apex

Δt = -0.70 ms

0.0

Normalized amplitude

Time (s)
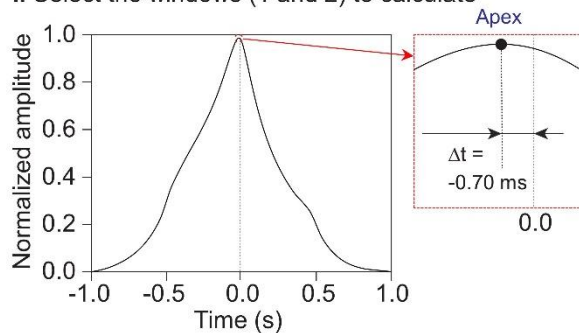
Supplementary Fig. 25 | The cross-correlation method. a, An example data set that is the same as those in Extended Data Fig. 5a. **b**, We select the signals of (2,1) and (1,1) and section the data into five windows. Each window is one-second-long and includes one action potential spike. We choose the fifth pair of windows to conduct the cross-correlation and use the action potential spike as the reference point. Cross-correlation calculated in MATLAB (See Supplementary Note 14.2) in the right plot shows a -0.70 ms latency (τ) from (1,1) to (2,1). By calculating the other four pairs of windows, we find the average latency from (1,1) to (2,1) is -0.68 ms. Similarly, latencies between any other two FETs can be accurately calculated, and the action potentials' propagating characteristics are faithfully revealed.
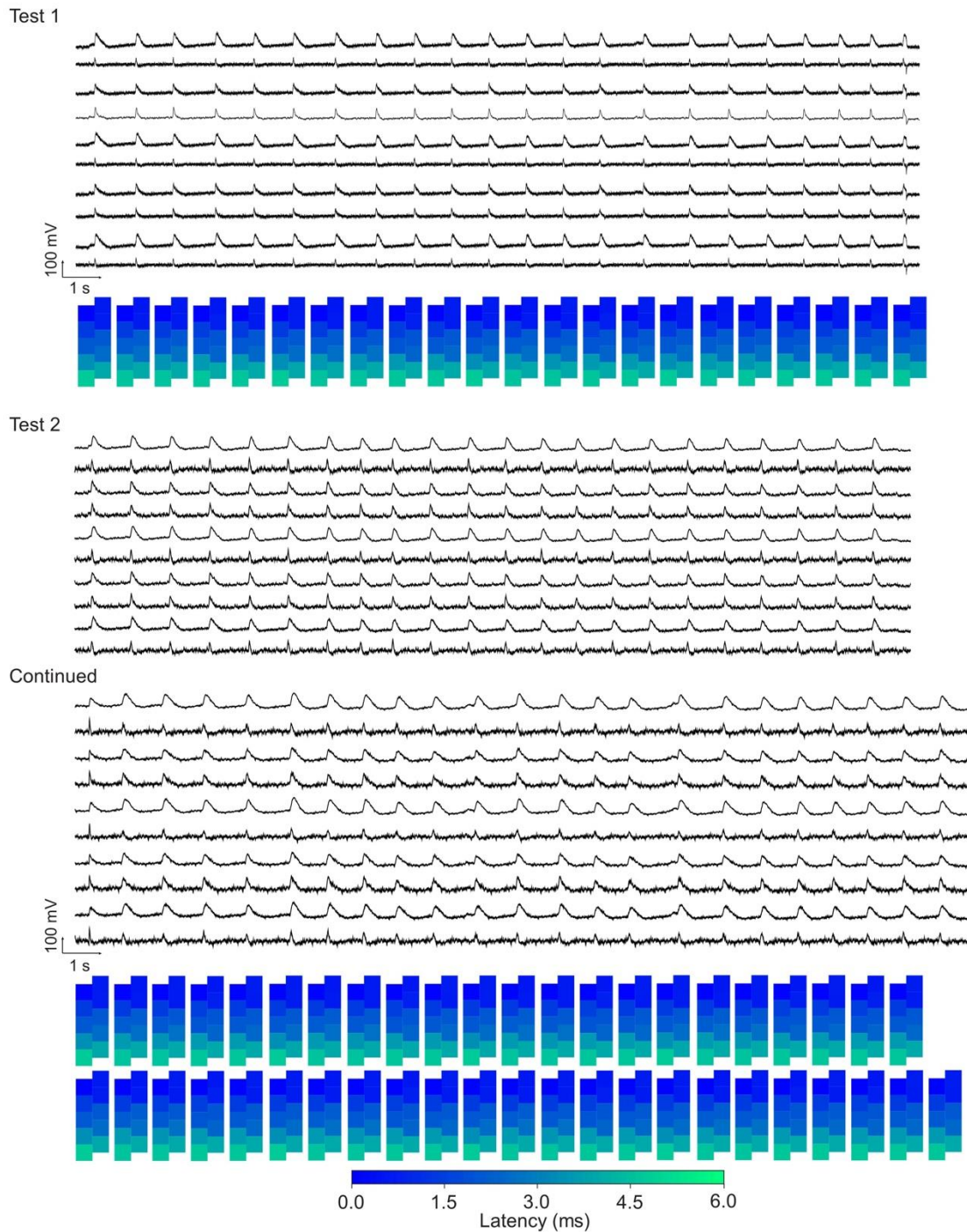
953
Supplementary Fig. 26 | Long-period recordings of intracellular signals of paced HL-1 cells by the 10-FET array. The stimulation electrode is ~10 mm to the northwest corner of the FET array. Heatmaps elucidate the action potentials' latencies and the occurrence sequence among the cells. Signals of tests 1 and 2 show continuous recordings for 25 and 50 seconds, respectively, which is the longest among all arrayed FET-based intracellular probes in the literature. The extended intracellular recordings prove the stable performance of each one of the FETs in the array.
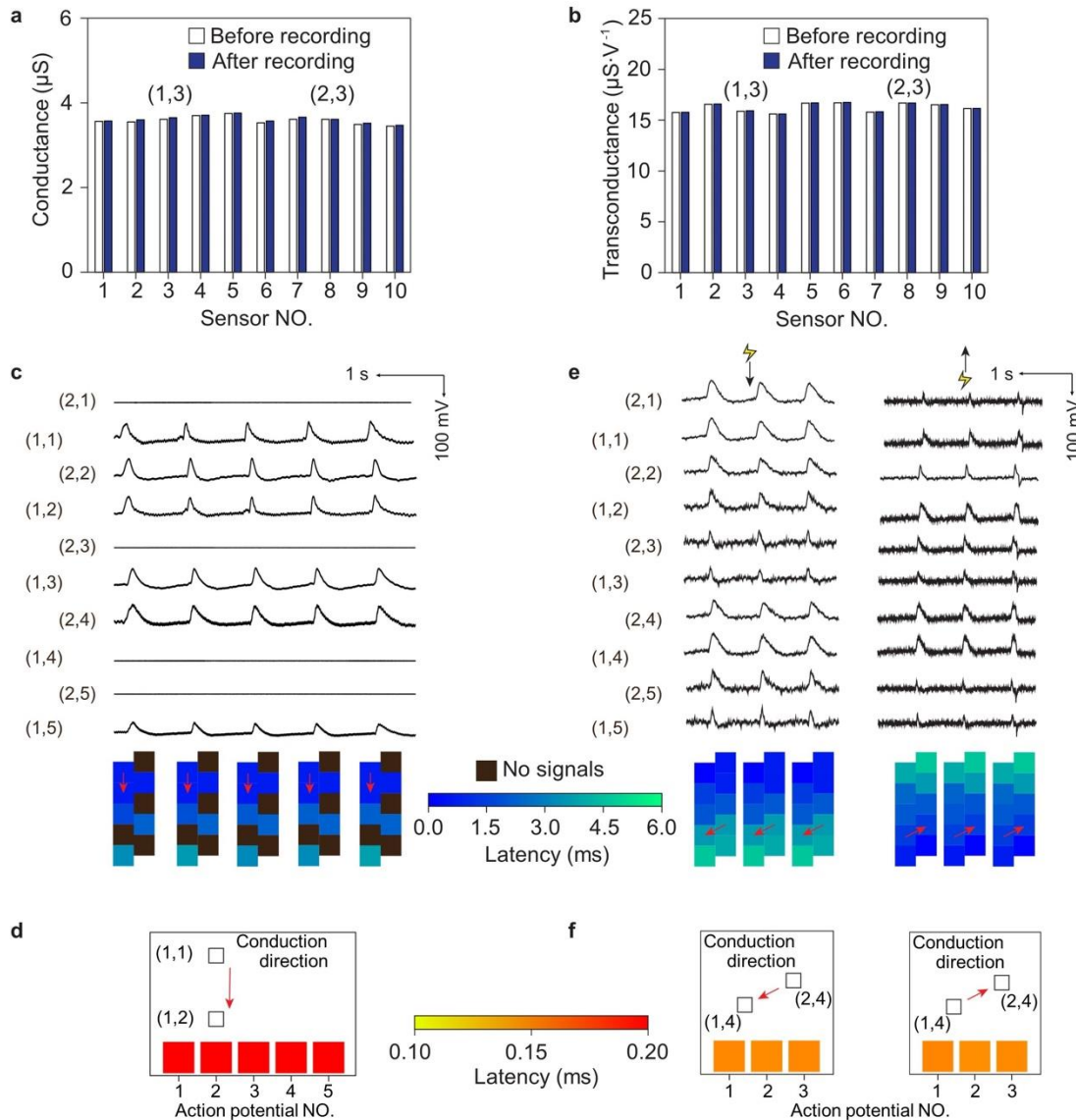
Supplementary Fig. 27 | Justification of the intracellular signal conduction inside a HL-1 cell. a,b, Comparable conductance and transconductances of the 10-FET array measured before and after intracellular recordings, showing that the FETs maintain their intact electrical properties and are free from any crosstalk or short circuits between the FETs. The same FET array is used for the recordings in Fig. 4d and Extended Data Fig. 5. **c,d,** With the same electrical stimulation **(nw)** as that in Extended Data Fig. 5, another recording by the same FET array on a different HL-1 cell culture showing a ~0.18 ms latency between FETs (1,1) and (1,2), which are 35 µm apart. The intracellular signal conduction velocity is ~194 µm·ms^{-1} that is close to the measurements (~182 µm·ms^{-1}) in Extended Data Fig. 5. Such reproducible and reliable results provide additional evidence for the intracellular signal conductions. **e,f,** Studying the relationship between intracellular and intercellular signal conduction directions on another recording on HL-1 cell culture. In this case, the intracellular conduction direction from (2,4) to (1,4) varies with the intercellular direction when the stimulation orientation is changed from the north to the south of the FETs. The intracellular signal conduction velocity is ~191 µm·ms^{-1}, which is on par with the results in other measurements.
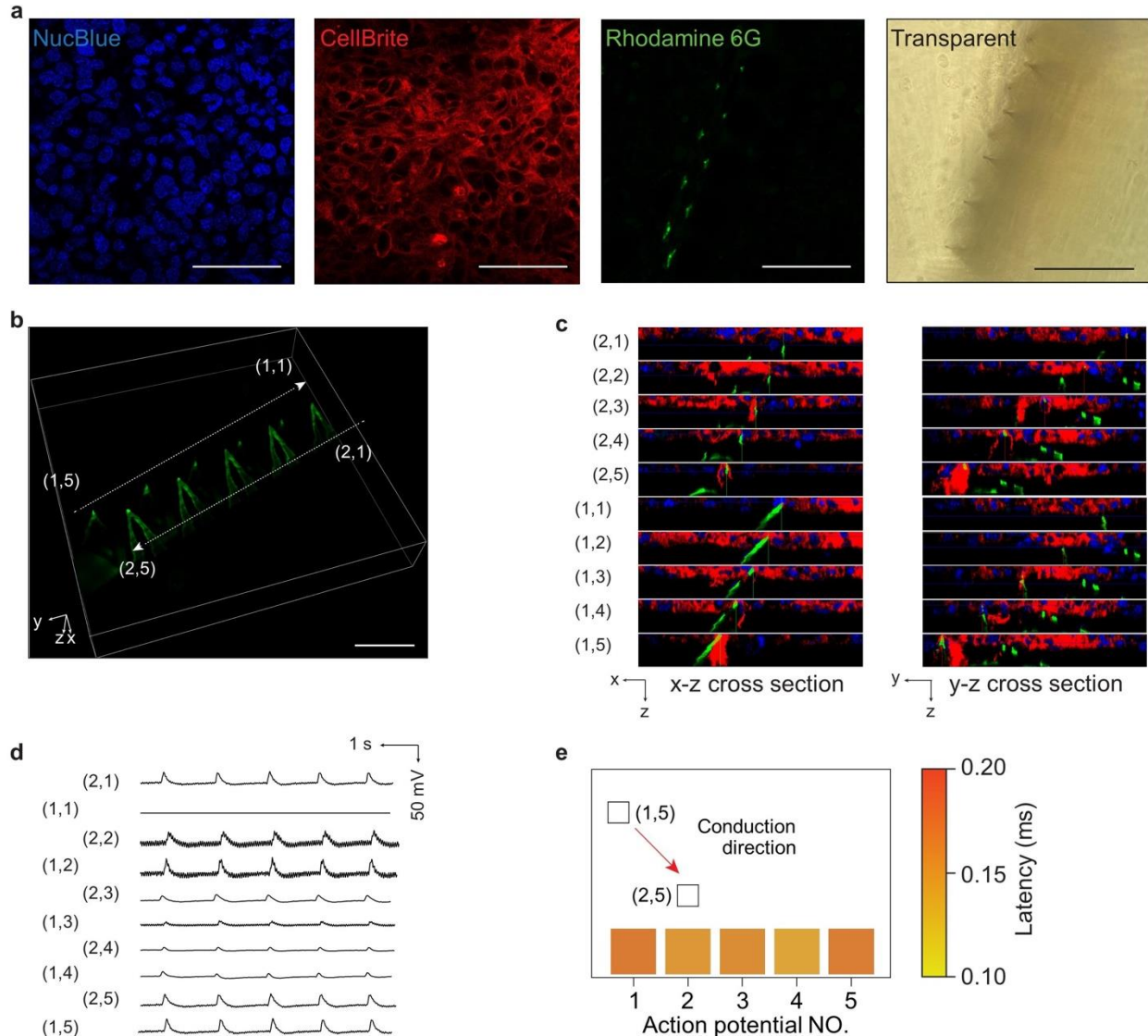
Supplementary Fig. 28 | Fluorescent images and simultaneous electrical recordings of an FET array and HL-1 cells. The cells and FETs are prepared according to the staining protocol introduced in Supplementary Note 17. **a**, Fluorescent images of nuclei (NucBlue), cell membranes (CellBrite), and FETs (Rhodamine 6G), as well as a bright field optical image, illustrating features of the cells and FETs. Scale bars: 100 μm. **b**, A 3D view image corresponding to the images in Fig. 4f, showing the FETs structures and relative spatial locations. Scale bar: 50 μm. **c**, Cross-sectional images of each FET in the x-z and y-z planes, showing well-defined interfaces between the cells and FETs. **d**,**e**, Simultaneous electrical recordings performed with the fluorescent confocal imaging. The intracellular conduction direction is from (1,5) to (2,5). The intracellular signal conduction velocity is ~184 μm·ms^{-1}.
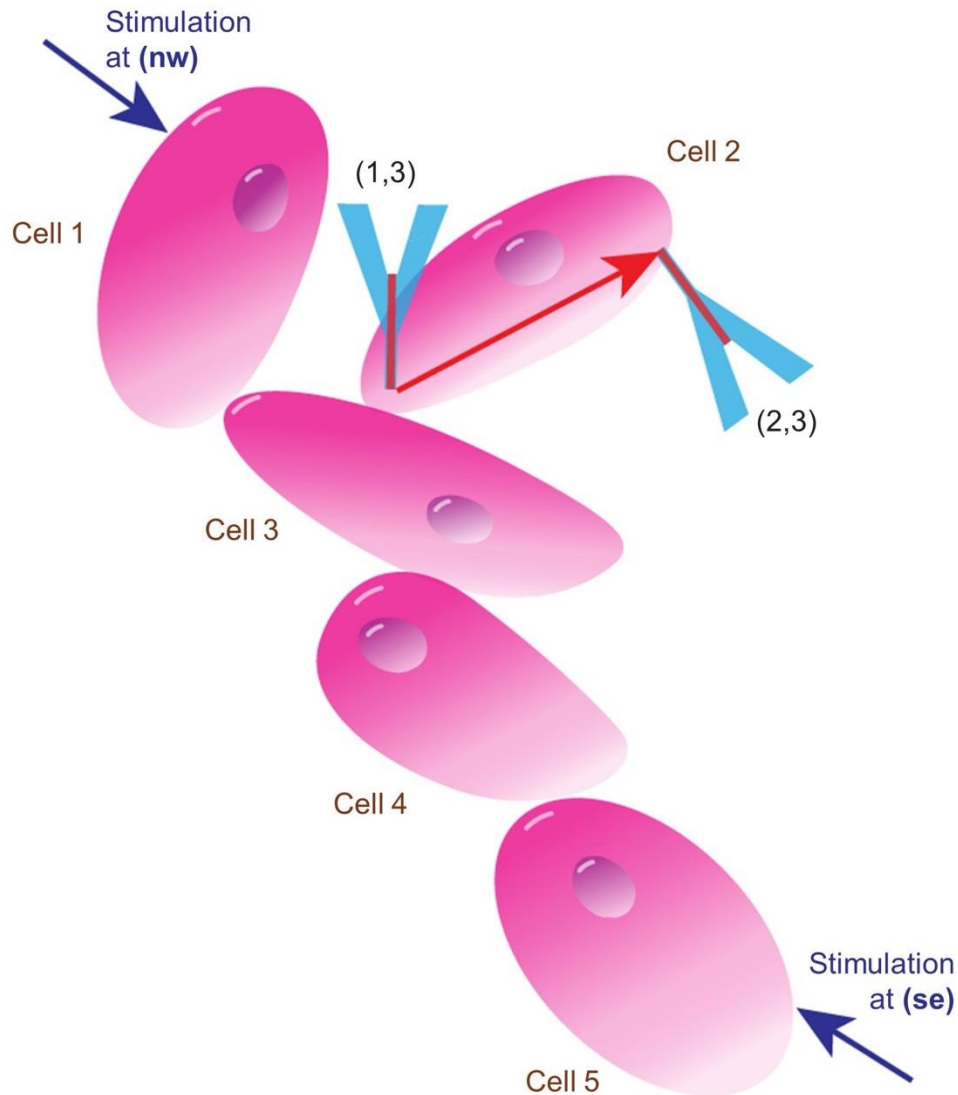
Supplementary Fig. 29 | A simplified model illustrating the independence of inter- and intra-cellular signal conduction directions. Five cells are electrically coupled with each other at the contacted areas. Two FETs record intracellular signals simultaneously from Cell 2. Particularly, Cell 2 is only electrically coupled with Cell 3. When the stimulation is placed at the northwest **(nw)** orientation to the FETs, the intercellular signal propagates from Cell 1 and travels to Cell 3 and Cell 2. The intracellular conduction direction is from (1,3) to (2,3), because (1,3) is closer than (2,3) to the electrical coupling position between Cell 2 and Cell 3. When the stimulation is placed at the southeast **(se)** corner, the intercellular signal propagates from Cell 5 to Cell 4, Cell 3, and then Cell 2. Similarly, the intracellular signal conduction is still from (1,3) to (2,3) due to the same reason. In other words, the incoming signal from the upstream cell always first arrives at a location closer to (1,3) than (2,3), leading to an invariant intracellular signal conduction direction regardless of the intercellular signal conduction directions. In this case, the intracellular signal conduction direction is dependent on cells' coupling positions and FETs' sensing locations on the cell membranes.

1002
1003 **Supplementary Fig. 30 | Organization of the 128-FET array and display of data. a**, Schematic
1004 distribution of the 128-FET array in eight arms of different directions, labeled counterclockwise
1005 from A to H. In each arm, the FETs have different heights distributed in three loops, labeled as 1,
1006 2, and 3. **b**, A raster plot with coordinates of each FET in the array, whose data are in Fig. 5b. **c**,
1007 Heatmaps with the raster layout in (**b**) showing the normalized amplitude of each FET at specific
1008 time points, e.g., t_1, t_2, etc. The transient information of each FET's recordings could be animated
1009 by stacking many heatmaps of sequential time points, as in Supplementary Video 5.

a Overview

PC/GUI

DAQ

128-FET device

b 128-FET device and 3D cardiac tissue

Jumper wires

3D cardiac tissue

c

ACF cables

d GUI

Supplementary Fig. 31 | Pictures of the experimental setup of recording electrophysiology of the 3D cardiac tissue by the 128-FET array. a, The measurement setup includes a 128-FET array connected to a flexible print circuit (FPC, uxcell) with flexible ACF cables, a customized DAQ board (Texas Instruments DDC264), and a GUI (provided by Texas Instruments). **b**, A closeup of the 128-FET array interfacing a 3D cardiac tissue. Signals transmit from the front-end sensors to the DAQ board via jumper wires. **c**, The 128-FET array fans out to the external circuits via flexible ACF cables. **d**, The DDC264 evaluation software is the interface used to command the DAQ board for data acquisition and storage.

a Input = 70 mV (V$_{p-p}$), R = 8.6 MΩ

b Input = 70 mV (V$_{p-p}$), R = 17.2 MΩ

c Input = 70 mV (V$_{p-p}$), R = 25.8 MΩ
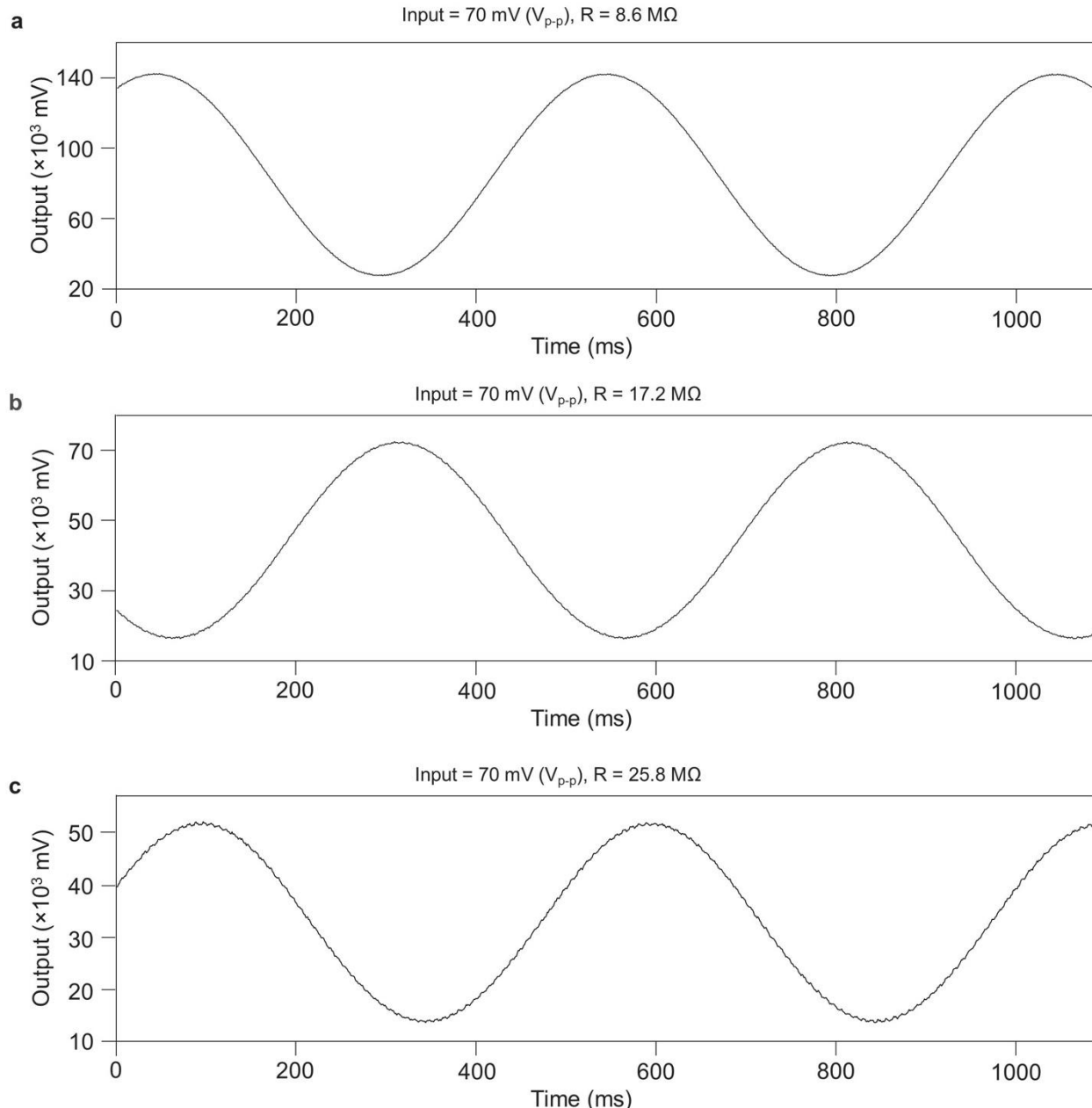
1019
1020 **Supplementary Fig. 32 | Amplification tests of the DDC264. a-c**, The DDC264 is a current input
1021 analog-to-digital converter. To calculate its amplification, a signal (sine wave, V$_{p-p}$ = 70 mV) is
1022 input into a channel on the DDC264 board and goes through various resistances. The output signal
1023 is recorded accordingly, when the resistance is (**a**) 8.6 MΩ, (**b**) 17.2 MΩ, and (**c**) 25.8 MΩ,
1024 respectively. The input current is the division of V$_{p-p}$ by the resistance, which is 8.14, 4.07, and
1025 2.71 nA in (**a**), (**b**), and (**c**), and the output voltage reading is correspondingly 111,941, 563,12,
1026 and 37,495 mV, respectively. Thus, the amplification of the DDC264 is 13.81 V·nA^{-1}, which is
1027 used to calculate the FET's current in the conduction channel, and further to derive the membrane
1028 potentials during cellular recordings.
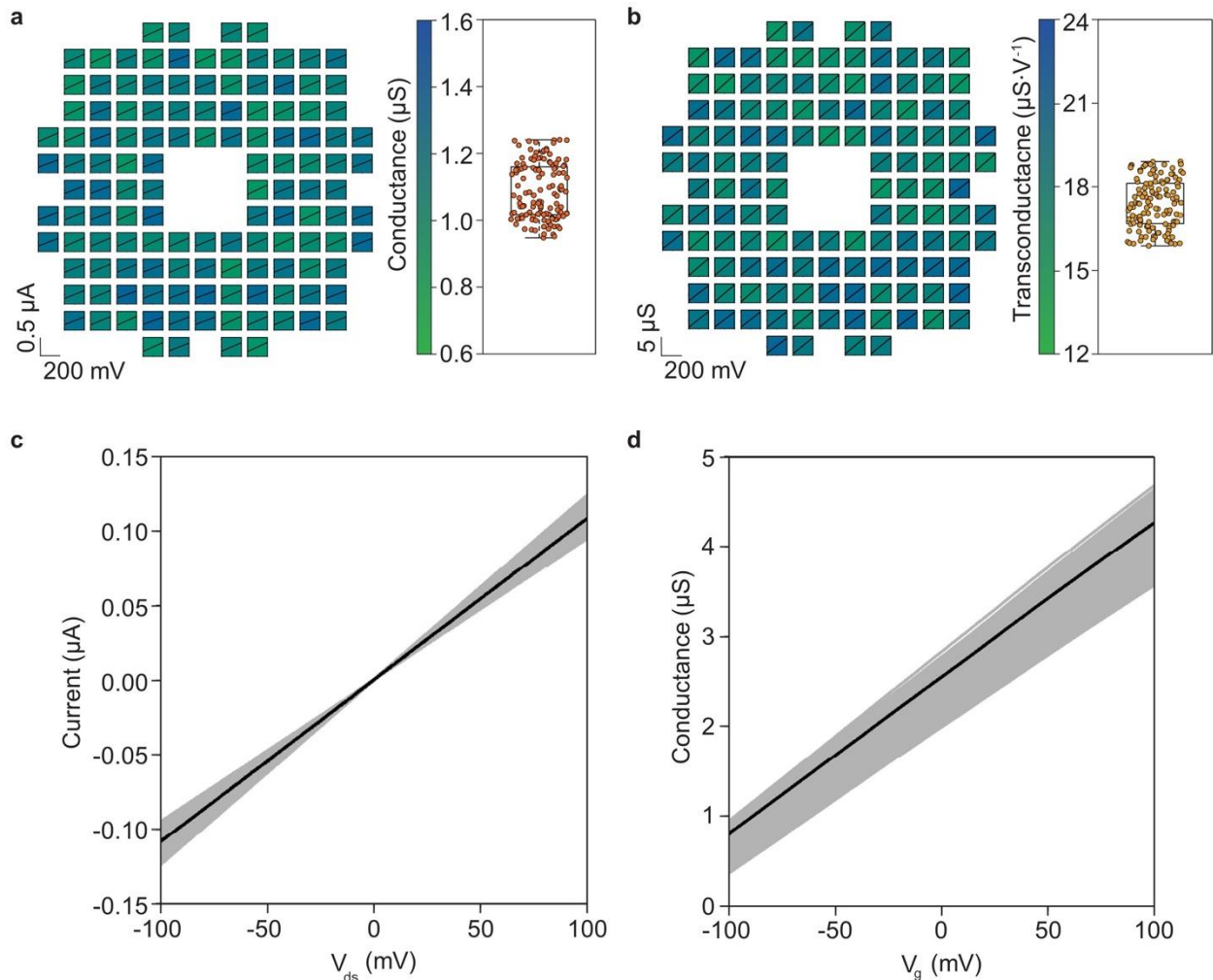
1029

Supplementary Fig. 33 | Electrical characterizations of the 128-FET array. a, Output
characteristics of each FET in the array. The measurement is performed with PBS solution (pH:
7.4 at 37 °C) covering the gate regions of all FETs and under a fixed 0 mV potential in the solution
by an Ag/AgCl electrode. The background color of each pixel of the raster plot represents the
conductance, in accordance with the color bar on the right. A box and whisker plot on the right
summarizing each sensor's conductance. The 128 FETs have an average conductance of 1.1 μS.
b, Transfer characteristics of each FET in the array. The measurement is performed in the same
configuration as the water-gate characterization (see Supplementary Fig. 4). A 100 mV potential
is applied to the source, and the signal is collected at the drain of each FET. The background color
of each pixel of the raster plot represents the transconductance, in accordance with the color bar
on the right. A box and whisker plot on the right summarizing each sensor's transconductance.
The 128 FETs have an average transconductance of 17 μS·V^{-1}. **c,d**, Summary of all 128 FETs'
output and transfer characteristics in gray lines, and the average is shown by the black lines. Both
the conductance and transconductance have great consistency among all of the 128 FETs, because
of the high reliability of the fabrication process. Each FET has high sensitivity for 3D tissue
mapping.
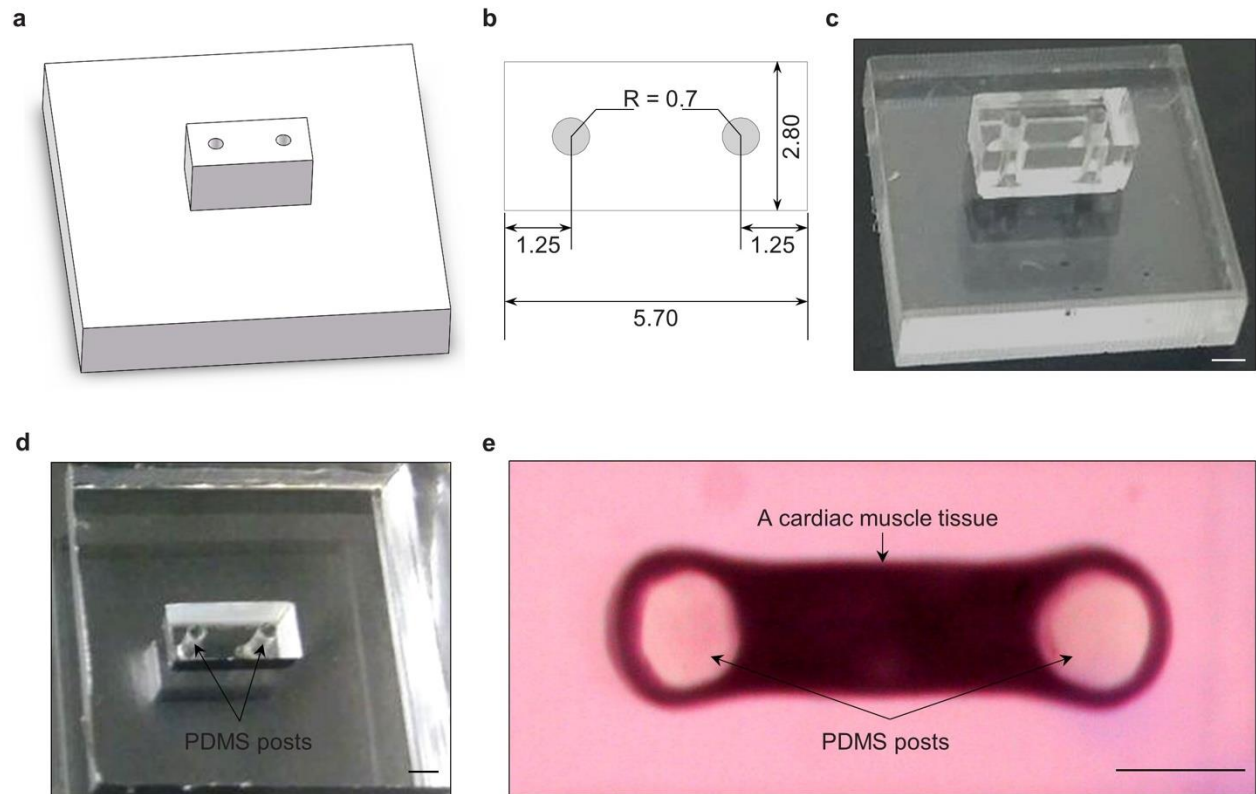
Supplementary Fig. 34 | Fabrication processes of the PDMS platform for cultivating cardiac microtissues. a, Schematics of the master mold. **b**, The top view of the well and micro-posts. Unit: mm. **c**, The PMMA master mold made by laser ablation. **d**, The PDMS well and two micro-posts made by the PMMA master mold. **e**, A cardiac microtissue around micro-posts and inside the well. All scale bars are 1 mm.
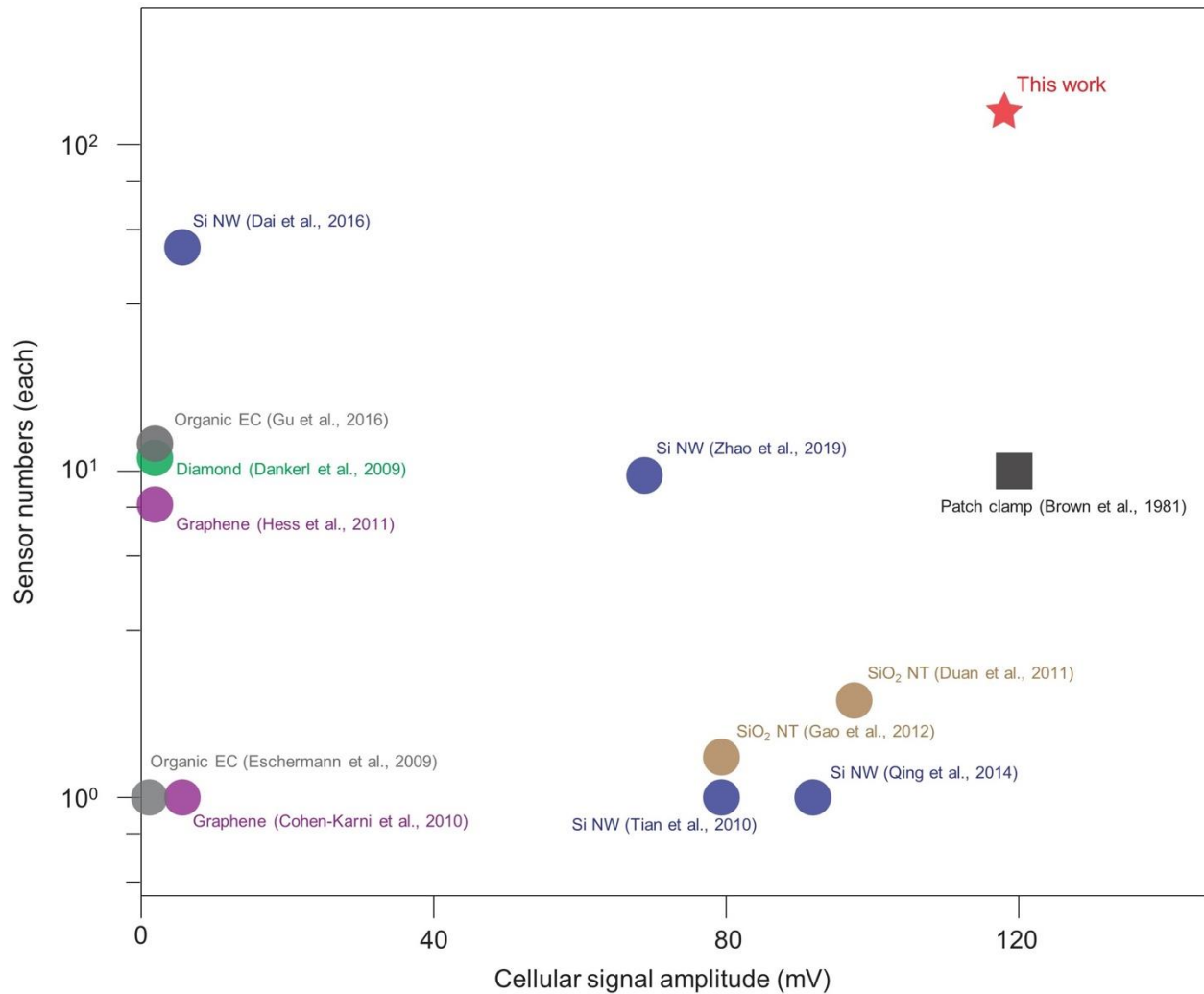
1052
1053 **Supplementary Fig. 35 | A summary of the 3D FETs for electrophysiology recording.** In
1054 comparison with the state of the art[12,22,33,34,37-44], the arrayed FETs demonstrated in this work have
1055 the greatest number of sensors and can record full-amplitude cardiomyocytic action potentials
1056 comparable to those by the patch-clamp.

Supplementary Tables

Supplementary Table 1 | Action potential durations and amplitudes before and after altering ion concentrations or administrating ion blockers. Abnormally high potassium ion or low sodium ion concentration in the extracellular environment would affect cell's membrane resting potential and change its action potential shape. Nifedipine and TTX can interfere with HL-1 cells by diminishing their membrane depolarization upstroke and thus decreasing the action potential duration (APD). The APD50 and APD90 in the table correspond to the action potentials shown in Fig. 3f and g.

Solutions	APD50 (ms)	APD90 (ms)	Amplitude (mV)	Refractory Period (ms)
Normal	121.2	222.4	119.4	925.4
Hyperkalemia	95.1	166.0	75.9	1154.6
Hyperkalemia washout	120.3	187.5	97.4	840.6
Hyponatremia	179.9	270.1	63.8	893.7
Hyponatremia washout	140.3	238.9	98.6	975.8
Nifedipine 60s	106.0	172.9	102.9	964.8
Nifedipine 120s	59.1	90.1	88.9	1022.3
TTX 60s	81.2	166.6	113.4	948.4
TTX 120s	65.5	141.8	91.9	958.6

Supplementary Table 2 | Action potential (AP) latencies of the recordings in Extended Data Fig. 5a. The stimulation electrode is placed ~10 mm to the four orientations of the FET array. Recordings of each FET contain five APs. We use the cross-correlation method to calculate the AP latencies between every two recordings. These values are listed below.

(nw)

FET	AP1 (ms)	AP2 (ms)	AP3 (ms)	AP4 (ms)	AP5 (ms)
(2,1)	0.68	0.68	0.67	0.68	0.68
(1,1)	0.00	0.00	0.00	0.00	0.00
(2,2)	0.65	0.66	0.65	0.65	0.65
(1,2)	1.46	1.46	1.44	1.44	1.47
(2,3)	2.24	2.26	2.23	2.24	2.22
(1,3)	2.09	2.11	2.08	2.10	2.08
(2,4)	2.75	2.80	2.71	2.74	2.72
(1,4)	3.42	3.42	3.40	3.40	3.41
(2,5)	4.08	4.08	4.07	4.07	4.08
(1,5)	4.75	4.76	4.74	4.74	4.75

(ne)

FET	AP1 (ms)	AP2 (ms)	AP3 (ms)	AP4 (ms)	AP5 (ms)
(2,1)	0.00	0.00	0.00	0.00	0.00
(1,1)	0.66	0.65	0.66	0.68	0.67
(2,2)	1.50	1.52	1.50	1.52	1.50
(1,2)	2.21	2.16	2.18	2.24	2.24
(2,3)	3.06	3.09	3.05	3.07	3.09
(1,3)	2.95	2.97	2.95	2.93	2.96
(2,4)	3.65	3.65	3.68	3.62	3.71
(1,4)	4.30	4.31	4.29	4.31	4.29
(2,5)	4.95	4.94	4.95	4.94	4.95
(1,5)	5.71	5.71	5.76	5.73	5.68

1078 **(sw)**

FET	AP1 (ms)	AP2 (ms)	AP3 (ms)	AP4 (ms)	AP5 (ms)
(2,1)	4.36	4.35	4.35	4.35	4.36
(1,1)	3.62	3.64	3.59	3.64	3.62
(2,2)	2.98	2.98	3.01	2.94	3.02
(1,2)	2.19	2.19	2.16	2.16	2.20
(2,3)	1.51	1.55	1.51	1.51	1.54
(1,3)	1.35	1.36	1.33	1.33	1.35
(2,4)	0.67	0.68	0.72	0.70	0.66
(1,4)	0.00	0.00	0.00	0.00	0.00
(2,5)	0.65	0.69	0.65	0.68	0.60
(1,5)	1.40	1.40	1.40	1.40	1.40

1079
1080 **(se)**

FET	AP1 (ms)	AP2 (ms)	AP3 (ms)	AP4 (ms)	AP5 (ms)
(2,1)	5.80	5.79	5.80	5.81	5.80
(1,1)	5.19	5.19	5.19	5.19	5.19
(2,2)	4.51	4.53	4.48	4.48	4.52
(1,2)	3.82	3.85	3.87	3.84	3.82
(2,3)	3.01	2.99	3.00	3.00	3.02
(1,3)	2.87	2.86	2.85	2.87	2.88
(2,4)	2.11	2.11	2.09	2.12	2.06
(1,4)	1.32	1.31	1.30	1.36	1.29
(2,5)	0.65	0.65	0.65	0.65	0.66
(1,5)	0.00	0.00	0.00	0.00	0.00

1081

Supplementary Table 3 | Action potential (AP) latencies of the long-period recordings in Supplementary Fig. 26. The stimulation electrode is placed ~10 mm to the northwest corner of the FET array. Recordings of each FET contain five APs. We use the cross-correlation method to calculate the AP latencies between each two recordings. These values are listed below.

Test 1

FET	AP1 (ms)	AP2 (ms)	AP3 (ms)	AP4 (ms)	AP5 (ms)	AP6 (ms)	AP7 (ms)	AP8 (ms)	AP9 (ms)	AP10 (ms)	AP11 (ms)	AP12 (ms)	AP13 (ms)	AP14 (ms)	AP15 (ms)
(2,1)	0.68	0.68	0.69	0.68	0.67	0.67	0.69	0.68	0.67	0.68	0.69	0.67	0.69	0.69	0.68
(1,1)	0.00	0.00	0.00	0.00	0.00	0.00	0.00	0.00	0.00	0.00	0.00	0.00	0.00	0.00	0.00
(2,2)	0.65	0.64	0.67	0.63	0.63	0.66	0.63	0.66	0.67	0.64	0.66	0.63	0.66	0.64	0.67
(1,2)	1.46	1.47	1.46	1.47	1.47	1.48	1.44	1.49	1.45	1.46	1.49	1.46	1.47	1.43	1.45
(2,3)	2.23	2.19	2.18	2.20	2.20	2.20	2.19	2.24	2.20	2.18	2.20	2.20	2.21	2.21	2.20
(1,3)	2.08	2.11	2.08	2.07	2.10	2.08	2.11	2.12	2.09	2.08	2.09	2.08	2.08	2.07	2.07
(2,4)	2.75	2.77	2.80	2.75	2.78	2.76	2.76	2.79	2.75	2.77	2.75	2.71	2.76	2.81	2.72
(1,4)	3.44	3.43	3.42	3.40	3.42	3.43	3.39	3.42	3.43	3.41	3.44	3.44	3.41	3.40	3.39
(2,5)	4.08	4.10	4.09	4.06	4.08	4.08	4.10	4.07	4.06	4.10	4.09	4.09	4.07	4.06	4.08
(1,5)	4.78	4.79	4.73	4.73	4.75	4.73	4.77	4.74	4.78	4.72	4.72	4.75	4.73	4.73	4.77

FET	AP16 (ms)	AP17 (ms)	AP18 (ms)	AP19 (ms)	AP20 (ms)	AP21 (ms)	AP22 (ms)
(2,1)	0.68	0.68	0.68	0.68	0.68	0.68	0.69
(1,1)	0.00	0.00	0.00	0.00	0.00	0.00	0.00
(2,2)	0.63	0.63	0.65	0.67	0.66	0.66	0.64
(1,2)	1.48	1.47	1.43	1.48	1.44	1.49	1.44
(2,3)	2.23	2.22	2.23	2.22	2.19	2.23	2.23
(1,3)	2.10	2.10	2.09	2.07	2.11	2.08	2.08
(2,4)	2.70	2.78	2.77	2.69	2.73	2.73	2.73
(1,4)	3.44	3.43	3.43	3.40	3.43	3.41	3.42
(2,5)	4.07	4.09	4.06	4.09	4.09	4.09	4.07
(1,5)	4.73	4.73	4.72	4.79	4.76	4.76	4.76

1090 **Test 2**

FET	AP1 (ms)	AP2 (ms)	AP3 (ms)	AP4 (ms)	AP5 (ms)	AP6 (ms)	AP7 (ms)	AP8 (ms)	AP9 (ms)	AP10 (ms)	AP11 (ms)	AP12 (ms)	AP13 (ms)	AP14 (ms)	AP15 (ms)
(2,1)	0.68	0.67	0.67	0.68	0.67	0.67	0.68	0.69	0.67	0.68	0.67	0.69	0.67	0.69	0.67
(1,1)	0.00	0.00	0.00	0.00	0.00	0.00	0.00	0.00	0.00	0.00	0.00	0.00	0.00	0.00	0.00
(2,2)	0.66	0.64	0.64	0.65	0.65	0.64	0.64	0.64	0.64	0.64	0.64	0.66	0.67	0.63	0.66
(1,2)	1.44	1.47	1.45	1.47	1.47	1.44	1.43	1.45	1.48	1.46	1.45	1.44	1.46	1.46	1.49
(2,3)	2.20	2.24	2.23	2.18	2.22	2.20	2.23	2.18	2.23	2.21	2.22	2.22	2.22	2.20	2.19
(1,3)	2.08	2.10	2.10	2.09	2.10	2.09	2.11	2.11	2.09	2.09	2.13	2.10	2.08	2.10	2.13
(2,4)	2.75	2.78	2.79	2.79	2.70	2.71	2.76	2.74	2.78	2.76	2.81	2.71	2.81	2.74	2.79
(1,4)	3.40	3.44	3.41	3.43	3.43	3.41	3.41	3.45	3.41	3.43	3.42	3.40	3.42	3.41	3.42
(2,5)	4.08	4.08	4.07	4.07	4.07	4.10	4.07	4.08	4.08	4.08	4.07	4.09	4.09	4.07	4.08
(1,5)	4.72	4.76	4.71	4.72	4.72	4.77	4.76	4.76	4.78	4.74	4.77	4.72	4.71	4.73	4.73

FET	AP16 (ms)	AP17 (ms)	AP18 (ms)	AP19 (ms)	AP20 (ms)	AP21 (ms)	AP22 (ms)	AP23 (ms)	AP24 (ms)	AP25 (ms)	AP26 (ms)	AP27 (ms)	AP28 (ms)	AP29 (ms)	AP30 (ms)
(2,1)	0.69	0.68	0.68	0.67	0.67	0.68	0.68	0.69	0.67	0.69	0.68	0.68	0.69	0.67	0.67
(1,1)	0.00	0.00	0.00	0.00	0.00	0.00	0.00	0.00	0.00	0.00	0.00	0.00	0.00	0.00	0.00
(2,2)	0.63	0.66	0.67	0.64	0.63	0.67	0.65	0.67	0.64	0.67	0.66	0.64	0.63	0.66	0.63
(1,2)	1.48	1.48	1.44	1.48	1.47	1.48	1.44	1.43	1.43	1.48	1.47	1.48	1.48	1.46	1.46
(2,3)	2.22	2.21	2.22	2.22	2.19	2.22	2.23	2.22	2.19	2.20	2.21	2.21	2.24	2.22	2.19
(1,3)	2.11	2.11	2.11	2.10	2.07	2.12	2.13	2.12	2.11	2.11	2.11	2.09	2.12	2.08	2.12
(2,4)	2.77	2.81	2.73	2.70	2.78	2.73	2.68	2.75	2.81	2.71	2.75	2.71	2.69	2.70	2.69
(1,4)	3.42	3.42	3.40	3.45	3.41	3.43	3.42	3.44	3.41	3.41	3.39	3.40	3.41	3.44	3.39
(2,5)	4.08	4.06	4.06	4.07	4.09	4.08	4.06	4.10	4.08	4.09	4.09	4.07	4.09	4.09	4.08
(1,5)	4.78	4.78	4.74	4.78	4.74	4.75	4.77	4.76	4.79	4.75	4.79	4.77	4.77	4.78	4.77

FET	AP31 (ms)	AP32 (ms)	AP33 (ms)	AP34 (ms)	AP35 (ms)	AP36 (ms)	AP37 (ms)	AP38 (ms)	AP39 (ms)	AP40 (ms)	AP41 (ms)	AP42 (ms)	AP43 (ms)	AP44 (ms)	AP45 (ms)
(2,1)	0.68	0.68	0.68	0.69	0.68	0.68	0.68	0.68	0.68	0.68	0.69	0.68	0.68	0.68	0.67
(1,1)	0.00	0.00	0.00	0.00	0.00	0.00	0.00	0.00	0.00	0.00	0.00	0.00	0.00	0.00	0.00
(2,2)	0.64	0.67	0.64	0.65	0.67	0.66	0.64	0.67	0.64	0.64	0.63	0.64	0.67	0.64	0.64
(1,2)	1.44	1.48	1.49	1.49	1.45	1.47	1.47	1.45	1.47	1.45	1.45	1.47	1.47	1.44	1.49
(2,3)	2.21	2.21	2.19	2.21	2.23	2.22	2.19	2.21	2.23	2.20	2.22	2.22	2.23	2.21	2.24
(1,3)	2.12	2.12	2.11	2.09	2.11	2.11	2.12	2.13	2.07	2.08	2.12	2.12	2.10	2.09	2.09
(2,4)	2.77	2.70	2.77	2.77	2.81	2.69	2.70	2.69	2.69	2.73	2.76	2.76	2.75	2.79	2.79
(1,4)	3.40	3.41	3.44	3.41	3.39	3.41	3.43	3.45	3.45	3.40	3.43	3.39	3.42	3.44	3.44
(2,5)	4.08	4.10	4.08	4.09	4.07	4.08	4.07	4.07	4.09	4.10	4.10	4.10	4.07	4.09	4.08
(1,5)	4.71	4.78	4.77	4.74	4.76	4.73	4.77	4.76	4.73	4.72	4.71	4.77	4.77	4.72	4.78

1091

Supplementary Table 4 | Signal occurrence times of each FET in the 128-FET array from the 3D cardiac tissue. The recording duration is 2,048 ms at a sampling rate of 1 kHz. The first recorded signal of the entire array appears at H2i after 43 ms from the start of recording.

FET label			Signal occurrence time (ms)							
			A	B	C	D	E	F	G	H
Loop 1	a	i	1480	-	864	792	673	547	-	166
		ii	-	1294	865	794	674	549	253	167
		iii	-	1295	866	795	675	-	255	170
	b	iv	-	-	-	-	549	-	288	171
		v	1533	1329	885	830	552	617	290	173
		vi	1534	-	-	834	-	620	293	175
Loop 2	a	i	1856	1030	-	717	-	-	193	43
		ii	1857	1032	894	719	633	487	194	45
		iii	1860	1034	896	-	635	491	198	48
	b	iv	1880	1026	907	-	644	507	-	-
		v	1882	-	908	730	645	509	211	73
		vi	1886	1030	909	732	649	511	213	75
Loop 3	a	i	-	-	-	-	591	400	-	141
		ii	1606	-	946	786	593	402	271	143
		iii	1608	1195	948	788	594	404	273	144
		iv	1610	-	954	791	596	405	113	146

Supplementary Table 5 | Intercellular signal conduction velocity calculation within each unit.
The average velocity in the small scale is 18.8 ± 7.5 $\mu m \cdot ms^{-1}$, which is larger than those velocities of signal conduction between different units in Fig. 5f. Because the distance of the conduction pathway between different units is regarded as a straight line instead of a rugged one, the calculation shortens the resulted conduction distance and thus reduces the velocities.

FET label		Signal conduction velocities within each unit ($\mu m \cdot ms^{-1}$)							
		A	B	C	D	E	F	G	H
Loop 1	a	-	35.0	35.0	23.3	35.0	17.5	17.5	17.5
	b	35.0	-	-	8.8	11.7	11.7	14.0	17.5
Loop 2	a	17.5	17.5	17.5	17.5	17.5	8.8	14.0	14.0
	b	11.7	17.5	35.0	17.5	14.0	17.5	17.5	17.5
Loop 3	a	17.5	-	8.8	17.5	21.0	21.0	17.5	21.0

References

1. Xu, S. et al. Assembly of micro/nanomaterials into complex, three-dimensional architectures by compressive buckling. *Science* **347**, 154-159 (2015).

2. Viventi, J. et al. A conformal, bio-interfaced class of silicon electronics for mapping cardiac electrophysiology. *Sci. Transl. Med.* **2**, 24ra22 (2010).

3. Lee, Y. K. et al. Dissolution of Monocrystalline Silicon Nanomembranes and Their Use as Encapsulation Layers and Electrical Interfaces in Water-Soluble Electronics. *ACS Nano* **11**, 12562-12572 (2017).

4. Dargent, T. et al. An interferometric scanning microwave microscope and calibration method for sub-fF microwave measurements. *Rev Sci Instrum* **84**, 123705 (2013).

5. Li, J. et al. in *2018 IEEE/MTT-S International Microwave Symposium - IMS.* 115-118.

6. Sonmez, B. G., Ertop, O. & Mutlu, S. Modelling and Realization of a Water-Gated Field Effect Transistor (WG-FET) Using 16-nm-Thick Mono-Si Film. *Sci Rep* **7**, 12190 (2017).

7. Yuan, S., Fan, X. & Wang, Z. Design and fabrication of field-effect biosensors for biochemical detection. *IET Nanobiotechnol* **8**, 208-215 (2014).

8. Rettinger, J., Schwarz, S. & Schwarz, W. *Electrophysiology*. (Springer International Publishing, 2016).

9. Lee, J. W., Yun, W. S. & Ghibaudo, G. Impact of trap localization on low-frequency noise in nanoscale device. *Journal of Applied Physics* **115**, 194501 (2014).

10. Lee, J. W. et al. Analysis of charge sensitivity and low frequency noise limitation in silicon nanowire sensors. *J. of Appl. Phys.* **107**, 044501 (2010).

11. Elasser, A. & Chow, T. P. Silicon carbide benefits and advantages for power electronics circuits and systems. *Proceedings of the IEEE* **90**, 969-986 (2002).

12. Duan, X. et al. Intracellular recordings of action potentials by an extracellular nanoscale field-effect transistor. *Nat. Nanotechnol.* **7**, 174-179 (2011).

13. Patlak, J. B. & Ortiz, M. Slow currents through single sodium channels of the adult rat heart. *Journal of General Physiology* **86**, 89-104 (1985).

1132   14.   Anumonwo, J. M. B., Tallini, Y. N., Vetter, F. J. & Jalife, J. Action Potential
1133   Characteristics and Arrhythmogenic Properties of the Cardiac Conduction System of the
1134   Murine Heart. *Circ. Res.* **89**, 329-335 (2001).

1135   15.   Grant, A. O. Cardiac Ion Channels. *Circulation: Arrhythmia and Electrophysiology* **2**, 185-
1136   194 (2009).

1137   16.   Gong, H. et al. Biomembrane-Modified Field Effect Transistors for Sensitive and
1138   Quantitative Detection of Biological Toxins and Pathogens. *ACS Nano* **13**, 3714-3722
1139   (2019).

1140   17.   Hu, C.-M. J. et al. Erythrocyte membrane-camouflaged polymeric nanoparticles as a
1141   biomimetic delivery platform. *Proc Natl Acad Sci USA* **108**, 10980-10985 (2011).

1142   18.   Ai, X. et al. Emerging Approaches to Functionalizing Cell Membrane-Coated
1143   Nanoparticles. *Biochemistry* **60**, 941-955 (2020).

1144   19.   Wang, S. et al. Drug Targeting via Platelet Membrane–Coated Nanoparticles. *Small
1145   Structures* **1**, 2000018 (2020).

1146   20.   Hu, C.-M. J. et al. A biomimetic nanosponge that absorbs pore-forming toxins. *Nat
1147   Nanotechnol* **8**, 336-340 (2013).

1148   21.   Zhuang, J. et al. Multimodal Enzyme Delivery and Therapy Enabled by Cell Membrane-
1149   Coated Metal–Organic Framework Nanoparticles. *Nano Letters* **20**, 4051-4058 (2020).

1150   22.   Tian, B. et al. Three-dimensional, flexible nanoscale field-effect transistors as localized
1151   bioprobes. *Science* **329**, 830-834 (2010).

1152   23.   Aalipour, A. et al. Plasma Membrane and Actin Cytoskeleton as Synergistic Barriers to
1153   Nanowire Cell Penetration. *Langmuir* **30**, 12362-12367 (2014).

1154   24.   Prinz, C. N. Interactions between semiconductor nanowires and living cells. *J Condens
1155   Matter Phys* **27**, 233103 (2015).

1156   25.   Elcarpio, J. O. B. D. et al. HL-1 cells : A cardiac muscle cell line that contracts and retains
1157   phenotypic characteristics of the adult cardiomyocyte. *Proc. Natl Acad. Sci. USA* **95**, 2979-
1158   2984 (1998).

1159   26.   White, S. M., Constantin, P. E. & Claycomb, W. C. Cardiac physiology at the cellular level:
1160   use of cultured HL-1 cardiomyocytes for studies of cardiac muscle cell structure and
1161   function. *Am J Physiol Heart Circ Physiol* **286**, H823-829 (2004).

1162   27.   Czeschik, A. et al. Nanostructured cavity devices for extracellular stimulation of HL-1 cells.
1163   *Nanoscale* **7**, 9275-9281 (2015).

1164   28.   Smith, A. W. et al. Long-term culture of HL-1 cardiomyocytes in modular poly(ethylene
1165   glycol) microsphere-based scaffolds crosslinked in the phase-separated state. *Acta*
1166   *Biomater* **8**, 31-40 (2012).

1167   29.   Fu, T. M. et al. Sub-10-nm intracellular bioelectronic probes from nanowire-nanotube
1168   heterostructures. *Proc Natl Acad Sci USA* **111**, 1259-1264 (2014).

1169   30.   Liu, H. et al. Heart-on-a-Chip Model with Integrated Extra- and Intracellular
1170   Bioelectronics for Monitoring Cardiac Electrophysiology under Acute Hypoxia. *Nano Lett*
1171   **20**, 2585-2593 (2020).

1172   31.   Zuppinger, C. 3D Cardiac Cell Culture: A Critical Review of Current Technologies and
1173   Applications. *Front. Cardiovasc. Med.* **6**, 87 (2019).

1174   32.   Tian, B. & Lieber, C. M. Nanowired Bioelectric Interfaces. *Chem. Rev.* **119**, 9136-9152
1175   (2019).

1176   33.   Zhao, Y. et al. Scalable ultrasmall three-dimensional nanowire transistor probes for
1177   intracellular recording. *Nat. Nanotechnol.* **14**, 783-790 (2019).

1178   34.   Qing, Q. et al. Free-standing kinked nanowire transistor probes for targeted intracellular
1179   recording in three dimensions. *Nat. Nanotechnol.* **9**, 142-147 (2014).

1180   35.   Dutta, S., Minchole, A., Quinn, T. A. & Rodriguez, B. Electrophysiological properties of
1181   computational human ventricular cell action potential models under acute ischemic
1182   conditions. *Prog Biophys Mol Biol* **129**, 40-52 (2017).

1183   36.   Kireev, D. et al. Graphene Multielectrode Arrays as a Versatile Tool for Extracellular
1184   Measurements. *Adv Healthc Mater* **6**2017).

1185   37.   Dai, X. et al. Three-dimensional mapping and regulation of action potential propagation in
1186   nanoelectronics-innervated tissues. *Nat. Nanotechnol.* **11**, 776-782 (2016).

1187   38.   Gao, R. et al. Outside looking in: nanotube transistor intracellular sensors. *Nano Lett* **12**,
1188   3329-3333 (2012).

1189   39.   Cohen-Karni, T. et al. Graphene and nanowire transistors for cellular interfaces and
1190   electrical recording. *Nano Lett.* **10**, 1098-1102 (2010).

1191 40. Dankerl, M. et al. Diamond Transistor Array for Extracellular Recording From
1192   Electrogenic Cells. *Adv. Funct. Mater.* **19**, 2915-2923 (2009).

1193 41. Eschermann, J. F. et al. Action potentials of HL-1 cells recorded with silicon nanowire
1194   transistors. *Appl Phys Lett* **95**, 1-4 (2009).

1195 42. Hess, L. H. et al. Graphene transistor arrays for recording action potentials from
1196   electrogenic cells. *Adv. Mater.* **23**, 5045-5049, 4968 (2011).

1197 43. Gu, X., Yao, C., Liu, Y. & Hsing, I. M. 16-Channel Organic Electrochemical Transistor
1198   Array for In Vitro Conduction Mapping of Cardiac Action Potential. *Adv Healthc Mater* **5**,
1199   2345-2351 (2016).

1200 44. Brown, A. M., Lee, K. S. & Powell, T. Voltage clamp and internal perfusion of single rat
1201   heart muscle cells. *The Journal of Physiology* **318**, 455-477 (1981).
1202